Silica diagenesis and physical properties of Cenozoic rocks in the North Viking Graben, northern North Sea

Thilo Wrona

A thesis submitted in partial fulfilment of the requirements for the degree of Doctor of Philosophy at Imperial College London

Department of Earth Science and Engineering

2015

Abstract

Silica diagenesis has the potential to drastically change the physical and fluid flow properties of the host strata and may therefore play a key role in the development of sedimentary basins. To investigate the role of silica diagenesis in the North Viking Graben, northern North Sea, mineralogical-, well- and 3-D seismic data are combined in this study. Optical microscopy, scanning electron microscopy and X-ray diffraction are used to identify the opal-A/CT transformation in the Cenozoic succession of the North Viking Graben, northern North Sea. The effect of the opal-A/CT transformation on the host rock properties is investigated by combining quantitative mineralogical data obtained by X-ray diffraction with wireline data of sixteen exploration wells using multiple linear regression analysis. The analysis shows that opal-A content explains host rock porosity to a large extent and opal-CT and pyrite content explain host rock porosity to a lesser degree. The overall decline in opal-A content with depth is interpreted to reflect increasing biogenic silica production between the Eocene and Miocene. Focussed reductions in opal-A content that coincide with increased opal-CT contents are probably the result of opal-A/CT transformation. Because the observed opal-A/CT transformation does not coincide with major lithology variations, it is assumed that the transformation is primarily a function of time and temperature. This assumption allows the spatial and temporal evolution of the opal-A/CT transformation to be modelled. Modelling results indicate that opal-A/CT transformation probably started in the Balder Formation in the Middle-to-Late Eocene, migrated upwards through the lower Hordaland Group, and fossilised as a result of Middle-Miocene sea-level fall and erosion. Based on the basin modelling results and a detailed fault analysis, silica diagenesis could have led to the nucleation and growth of the polygonal faults in the North Viking Graben. This study highlights that silica diagenesis is a complex process that can significantly impact compaction and deformation of siliceous sedimentary successions.

Declaration

The material contained in this thesis has not previously been submitted for a degree in this or any other institution. The work is my own, except where reference is made.



Thilo Wrona

The copyright of this thesis rests with the author and is made available under a Creative Commons Attribution Non-Commercial No Derivatives licence. Researchers are free to copy, distribute or transmit the thesis on the condition that they attribute it, that they do not use it for commercial purposes and that they do not alter, transform or build upon it. For any reuse or redistribution, researchers must make clear to others the licence terms of this work.

© Thilo Wrona 2015

Acknowledgements

First and foremost, I would like to thank my primary supervisor Chris Jackson for all his time, support, advice, and attention to detail that made this PhD such a great experience. I would also like to thank my external supervisors Mads Huuse and Kevin Taylor for their scientific insights and continues support in the last three years.

Thanks must also go to all the people helping me with my PhD; in particular to Craig Magee for numerous discussions and revisions of early (and therefore horrible) versions of the main thesis chapters. I would also like to thank Nick Holgate, Aruna Mannie and Peter Fitch for their help with the seismic-to-well tie, seismic interpretation and petrophysics. Jens Najorka, Tomasz Goral, Tony Wighton and Jacob Longridge are thanked for their help with X-ray diffraction, scanning electron microscopy, thin sections and optical microscopy. Evangelia Mavridou is thanked for her support with PetroMod. I would also like to thank Cedric John and Gary Hampson for their feedback during internal examinations. Joe Cartwright, Mark Ireland and one anonymous reviewer are thanked for the revision of the manuscript that forms Chapter 6 of this thesis. I would also like to thank all the people who took their time discussing my work with me; in particular Johan Claringbould, Matthew Andrew, Matthew Reeve, and Richard Jardine.

I would like to gratefully acknowledge funding from the Department of Earth Science and Engineering, the American Association of Petroleum Geologists, the British Sedimentological Research Group, the London Petrophysical Society, the Geological Society and the International Association of Sedimentologists. I also thank the Norwegian Petroleum Directorate for providing wireline data and cuttings samples, Statoil for seismic data, Senergy and Schlumberger for software.

Finally, I would like to thank my family and friends who made the last three years such a great experience. Danke Jens, Julia, Steffi, Juergen, Torsten, Katharina, Elli, Robert und Patrick. Thank you Issy, Jake, Meredith, Matt, Matt, Han, Yvette, Sarah, Craig, Akela, Bisma, Aruna, Tenice, Indranil, Alex, Tom, Steve and Matt. Gracias, Jorge y Dari. Спасибо, Irina. Merci, Benoit.

Tables of Contents

1. INTRODUCTION 1

1.1. RATIONALE 1

1.2. RESEARCH AIMS 3

2. LITERATURE REVIEW 4

2.1. SILICA MINERALS 4

2.1.1. Opal-A 4

2.1.2. Opal-CT 6

2.1.3. Quartz 8

2.2. SILICA DIAGENESIS 9

2.2.1. Kinetics 10

2.2.2. Water release 12

2.2.3. Physical properties 13

2.2.4. Seismic studies 16

3. STUDY AREA 19

4. DATA & METHODS 22

4.1. OPTICAL MICROSCOPY 22

4.2. SCANNING ELECTRON MICROSCOPY 24

4.3. X-RAY DIFFRACTION 26

4.3.1. Identification 26

4.3.2. Quantification 29

4.4. MINERALOGICAL DATA 32

4.4.1. Descriptive statistics 32

4.4.2. Correlation 36

4.5. WELL DATA 39

4.5.1. Petrophysics 39

4.5.2. Descriptive statistics 42

4.6. DATA INTEGRATION 44

4.6.1. Correlation 44

4.6.2. Multiple linear regression analysis 47

4.7. SEISMIC DATA 56

4.7.1. 3-D seismic reflection data 56

4.7.2. Seismic-to-well tie 58

4.7.3. Seismic interpretation 58

4.8. BASIN MODELLING 60
4.8.1. Modelling of the opal-A/CT transformation 63
4.9. FAULT ANALYSIS 65
4.9.1. Seismic interpretation 65
4.9.2. Depth conversion 67
4.9.3. Fault properties 68
4.9.4. Strain summation 72
5. RESULTS 75
5.1. MINERALOGY 75
5.1.1. Clay minerals 75
5.1.2. Silica minerals 75
5.1.2.1. Opal-A 75
5.1.2.2. Opal-CT 76
5.1.2.3. Quartz 76
5.2. ROCK PROPERTIES 77
5.3. SEISMIC EXPRESSION 77
5.4. BASIN MODELLING RESULTS 78
5.5. POLYGONAL FAULTS 80
5.5.1. Displacement 80
5.5.2. Strain 81
6. DISCUSSION & CONCLUSIONS 82
6.1. MINERALOGY 82
6.1.1. Clay minerals 82
6.1.1.1. Illite-smectite 82
6.1.1.2. Illite 83
6.1.1.3. Kaolinite 83
6.1.2. Silica minerals 83
6.1.2.1. Opal-A 83
6.1.2.2. Opal-CT 85
6.1.2.3. Quartz 86
6.2. ROCK PROPERTIES 88
6.2.1. Clay minerals 88
6.2.2. Silica minerals 88
6.3. EXTENT OF OPAL-A/CT TRANSFORMATION 90
6.4. DIAGENETIC HISTORY 91
6.4.1. Opal-A preservation 91

6.4.2. Evolution of opal-A/CT transformation 92
6.4.2.1. Formation 93
6.4.2.2. Migration 94
6.4.2.3. Fossilisation 94
6.5. POLYGONAL FAULTING 95
6.5.1. Nucleation 95
6.5.2. Growth 97
7. ADVANCES & IMPLICATIONS 100
7.1. SILICA DIAGENESIS 100
7.2. BASIN MODELLING 101
7.3. ROCK PHYSICS 101
7.4. WATER RELEASE 102
7.5. POLYGONAL FAULTING 102
8. APPENDIX 104
8.1. ENERGY DISPERSIVE SPECTRA 104
8.2. MINERALOGICAL AND WIRELINE DATA 105
8.3. R CODES 107
9. REFERENCES 108

1. INTRODUCTION

1.1. RATIONALE

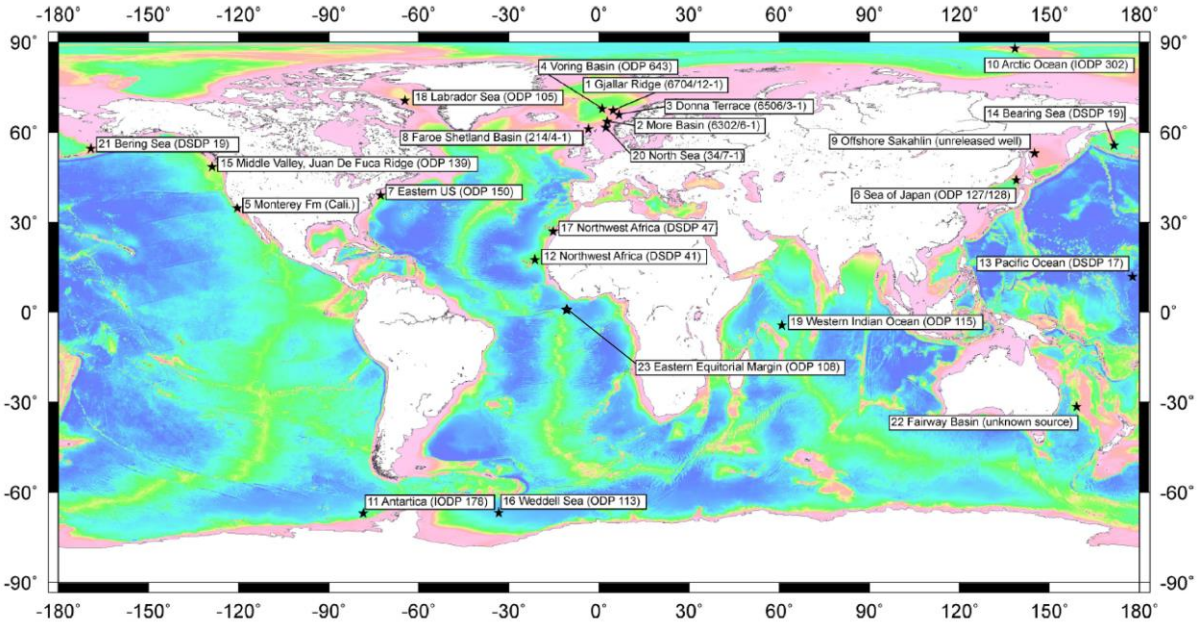


Figure 1.1: Global map showing diagenetic transformation of opal-A to opal-CT, confirmed by the ODP, IODP and DSDP (after Ireland, 2011)

Diagenesis, compaction and rock deformation are fundamental, often related processes in sedimentary basins (e.g. Fossen, 2010; Allen & Allen, 2013; Bjørlykke, 2014). Diagenesis describes the dissolution and precipitation of minerals during burial of sediments and sedimentary rocks. These reactions occur in response to a chemical and/or physical disequilibrium between the host strata and pore fluids. Attaining this equilibrium is further complicated by changing chemical and physical conditions in the host strata during burial. As a result of these changing conditions, diagenetic reactions in- or decrease in activity. Even though silica diagenesis, that is the transformation of amorphous, typically biogenic opal (opal-A) to low-crystalline, cristobalite/tridymite lepispheres (opal-CT) to microcrystalline quartz, has been documented by numerous field, borehole and seismic

studies around the world (Fig. 1.1), the controlling factors rate remain elusive. To infer the factors controlling silica diagenesis, it is crucial to know the overall mineralogy of the host rocks.

Diagenesis is intrinsically related to compaction, as mineral dissolution and precipitation can significantly alter the pore space and/or matrix volume (Addis & Jones, 1985; Bjørlykke, 1999). Compaction is often studied using porosities-depth functions that are derived from measurements of core samples or from wireline logs (e.g. Giles, 1997). These studies have been used to distinguish between compaction that has been driven by mechanical or chemical processes. Mechanical compaction typically involves grain re-orientation and breakage due to the weight of the overburden, whereas chemical compaction describes the rock volume reduction by dissolution and precipitation (i.e. diagenesis) (e.g. Bjørlykke, 2014). Although diagenesis is well known to impact compaction, the underlying microscopic processes are not well understood. To improve our understanding of these processes, it is required to combine analytical techniques (e.g. scanning electron microscopy and X-ray diffraction) with measurements of physical rock properties.

The deformation of sediments and rocks, that describes any change in shape or size of a volume when subject to stress, is also related to diagenesis. Deformation can be reversible (elastic) or irreversible (inelastic). A key type of inelastic deformation is fracturing, i.e. the separation of a volume by a discontinuity (Jaeger *et al.*, 2009; Gudmundsson, 2011). Fractures are distinguished based on their displacement (e.g. Price & Cosgrove, 1990). Shear fractures, for example, exhibit fracture-parallel displacement. When subject to continuous deformation, fractures can evolve into faults, i.e. surfaces or zones of macroscopic shear displacement (e.g. Fossen, 2010). Normal faults typically develop in response to and strike-perpendicular to the tectonic extension (Anderson, 1951). Polygonal faults, that are randomly-oriented, layer-bound normal faults, are difficult to explain by tectonic extension, but instead seem to be formed by internal contraction of the host strata (Cartwright & Lonergan, 1996). Recently, Shin *et al.* (2008) and Cartwright (2011) suggest that particle dissolution during diagenesis may lead to contraction of the host strata and polygonal faulting. This hypothesis can be tested by analysing the growth of polygonal faults in rocks that have undergone silica diagenesis.

1.2. RESEARCH AIMS

The overall goal of this study is to improve our understanding of silica diagenesis and to reveal its connection to sediment compaction and deformation. This is achieved by a truly interdisciplinary approach that includes analytical techniques, wireline, and 3-D seismic data of the North Viking Graben, northern North Sea. This approach allows the following research aims to be addressed:

I. Identify silica transformations in the Cenozoic succession of the North Viking Graben.

II. Document the extent of silica diagenesis in the North Viking Graben.

III. Understand the controls on silica deposition and diagenesis in the North Viking Graben.

IV. Determine the influence of silica diagenesis on the physical host rock properties.

V. Constrain the evolution of silica diagenesis in the North Viking Graben.

VI. Reconstruct polygonal fault growth in the North Viking Graben.

VII. Investigate the influence of silica diagenesis on polygonal faulting.

2. LITERATURE REVIEW

This literature review starts with a description of the three key minerals (opal-A, opal-CT and quartz) involved in silica diagenesis (Section 2.1). This description forms the foundation to the subsequent review of silica diagenesis (Section 2.2). At the end of this review, the water release (Subsection 2.2.2), physical property changes (Subsection 2.2.3) and seismic response of silica diagenesis (Subsection 2.2.4) are discussed.

2.1. SILICA MINERALS

Silica or silicon dioxide (SiO_2) is one of the most abundant chemical compounds on Earth and its minerals are essential constituents of sedimentary, metamorphic and igneous rocks. In sedimentary rocks, silica forms a variety of minerals that can undergo diagenesis, such as opal-A, opal-CT and quartz. To understand silica diagenesis, the structure, origin and physical properties of these three minerals are outlined.

2.1.1.Opal-A

Opal-A has been defined as amorphous, hydrous silica by Jones and Segnit (1971). The word ‘amorphous’ describes the poorly-ordered/non-crystalline structure of opal-A, whereas ‘hydrous’ indicates that opal-A can contain up to 17 wt.% water (Hurd & Theyer, 1975).

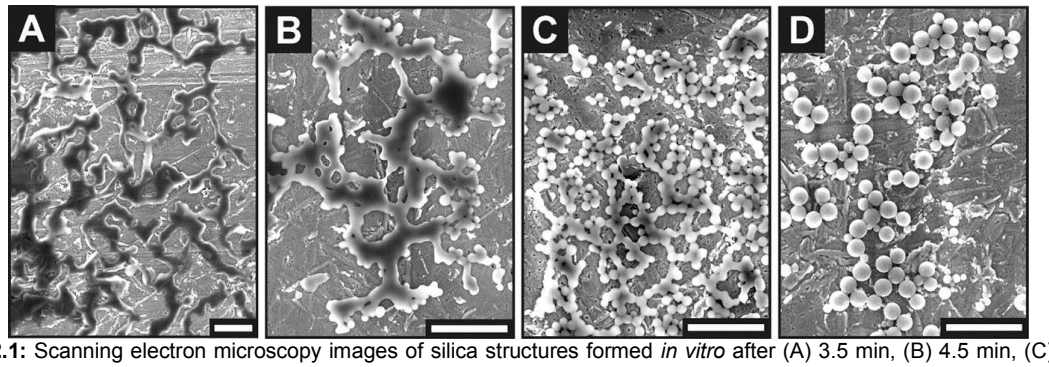


Figure 2.1: Scanning electron microscopy images of silica structures formed *in vitro* after (A) 3.5 min, (B) 4.5 min, (C) 5 min, and (D) 8 min after the addition of natSil-1A to a buffered monosilicic acid solution (50 mM sodium acetate, pH = 5.5). Scale bars, 2 µm (Kröger *et al.*, 2002).

In general, opal-A is either bio- or volcanogenic; with the former being more common than the latter. Biogenic opal-A is deposited in shallow and deep water depositional environments where surface productivity is increased by upwelling of nutrient-rich water (e.g. Hesse & Schacht, 2011). Diatoms, radiolarians, sponge spicules and silicoflagellates are the main sources of biogenic opal-A (Treguer & De La Rocha, 2013). These organisms increase the silicic acid concentration in solution from 10-70 μM in ocean surface water to 1000-2000 μM in their so-called silica deposition vesicles using sodium-dependent transport proteins (DeMaster, 2003). When the silicic acid concentration exceeds the solubility of amorphous silica, the monomeric silicic acid starts to polymerise (Williams & Crerar, 1985). The polymerisation involves condensation reactions transforming silanol to siloxane bonds (Iler, 1979). Siloxane bonds are maximised during condensation leading to the formation of nuclei (Perry, 2003). These nuclei grow either in size or in number dependent on the pH and cation concentration of the solution (Iler, 1979). In basic solution with low cation concentration, nuclei grow predominantly in size, forming nanometre-scale spheres (Fig. 2.1). These spheres are the building blocks for the complex skeletons of diatoms, radiolarians, sponge spicules and silicoflagellates (Fig. 2.2).

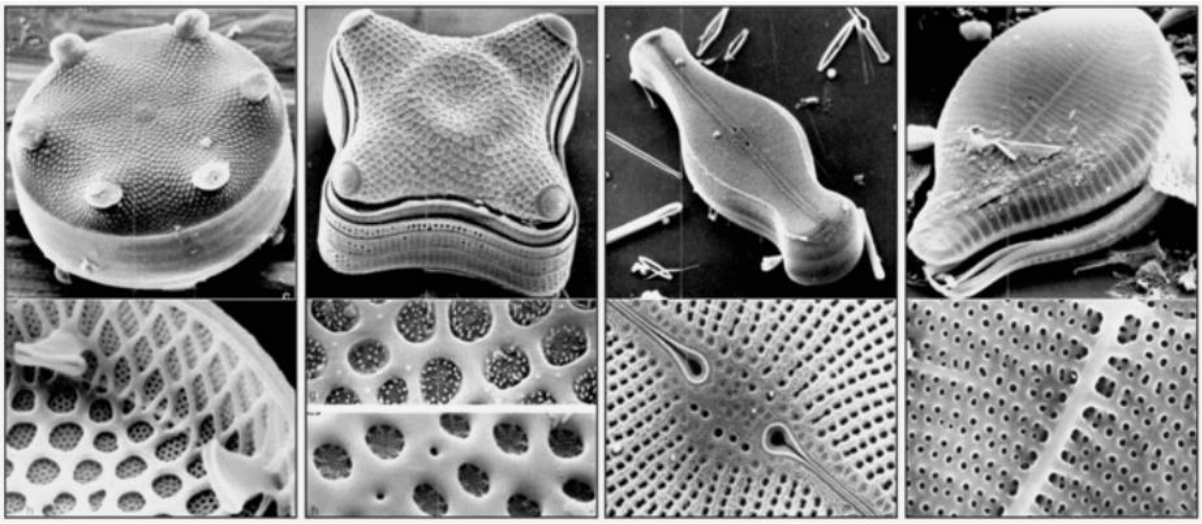


Figure 2.2: Scanning electron microscope images of the cell walls of four different diatom species (Kröger & Poulsen, 2008).

On a global scale, biogenic silica production is one factor controlling the deposition of silica in marine sediments. It is widely accepted that biogenic silica production is most effective at high

latitudes, where the initial silicic acid concentration is high and surface water temperature is low (Treguer & De La Rocha, 2013). Biogenic silica production however might be less important than silica preservation; the second component, controlling the deposition of biogenic silica in marine sediments. The importance of silica preservation is highlighted by the low global preservation ratio of only 3% (Treguer & De La Rocha, 2013). In other words, if biogenic silica is effectively produced in the surface water, but subsequently dissolved in the water column or at the seafloor, it would not be preserved in the sedimentary record. Unfortunately, silica preservation is not well-understood and further research on the current silica cycle is required (Treguer and De La Rocha, 2013).

2.1.2.Opal-CT

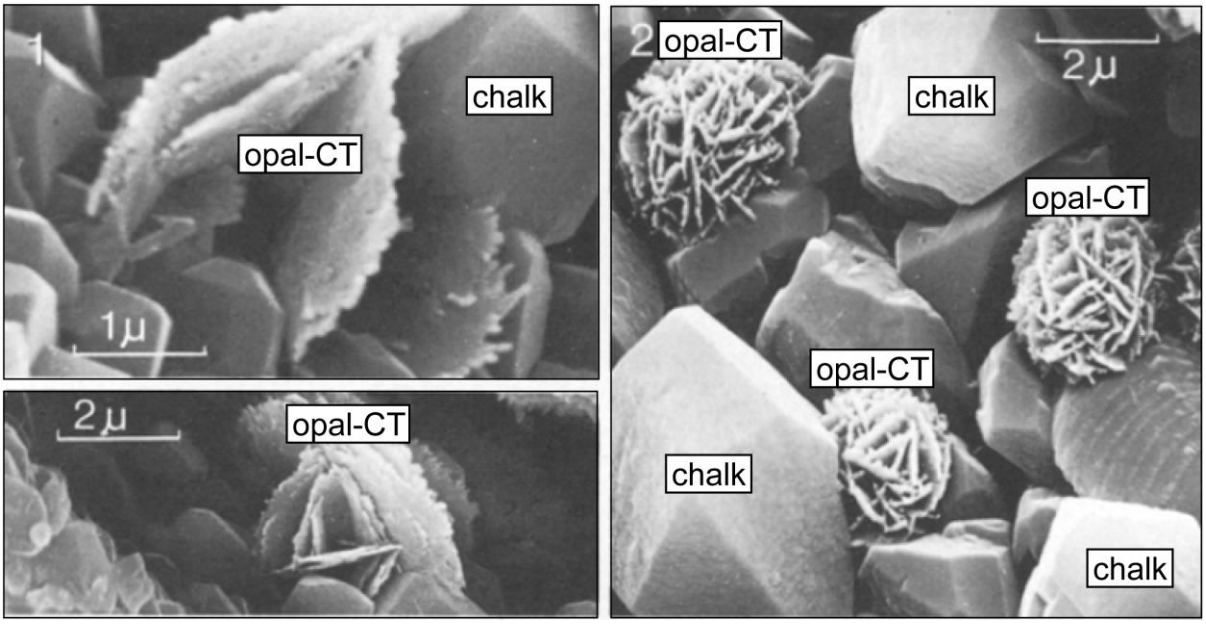


Figure 2.3: Scanning electron microscope images of opal-CT lepispheres in chalk (Flörke *et al.*, 1976)

Opal-CT consists of lepispheres, i.e. spheres of intertwined, microcrystalline cristobalite and tridymite blades (Fig. 2.3) (Jones & Segnit, 1971). These blades are extremely thin (30-50 nm) and intersect each other in order to form small lepispheres with diameters between 5-15 μm (Fig. 2.3) (DeMaster, 2003). Opal-CT is exclusively diagenetic in origin, as it is formed by authigenic silica precipitation (Williams & Crerar, 1985). To precipitate opal-CT, the silicic acid concentration of the

pore fluids must exceed opal-CT solubility. When the silicic acid concentration is sufficiently high, monomeric silicic acids start to polymerise. Williams and Crerar (1985) suggest that the preferred polymerisation of six-membered rings consisting of silica-tetrahedra leads to the precipitation of cristobalite and tridymite blades which consist of planar networks of these rings (Fig. 2.4).

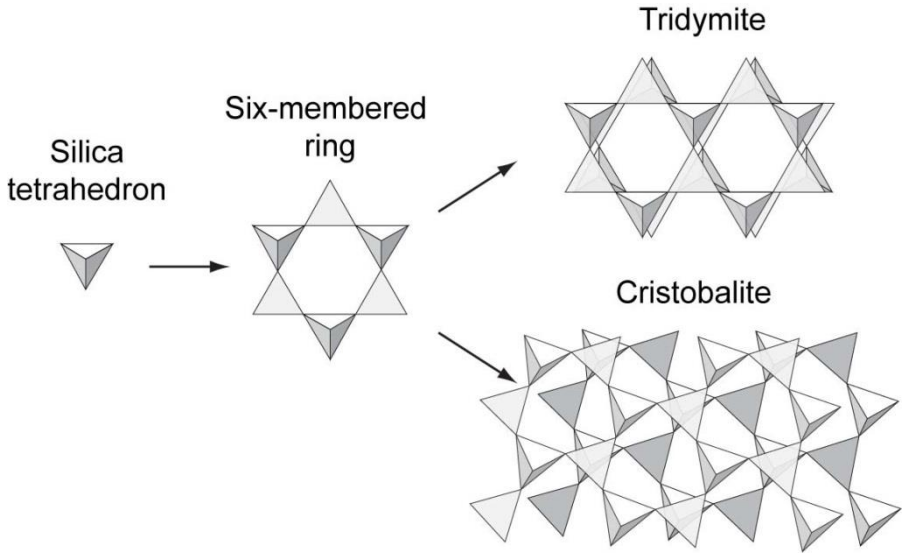


Figure 2.4: Atomic structure of silica tetrahedron, six-membered ring of tetrahedra and tridymite and cristobalite after Deer *et al.* (2004)

The growth of opal-CT lepispheres from cristobalite and tridymite blades appears to start with the precipitation of cristobalite (rather than tridymite) blades due to its favourable orientation of silica tetrahedra (Jones & Segnit, 1972; Flörke *et al.*, 1976). Stacking faults during cristobalite precipitation has been suggested to lead to twinning according to the twinning laws of tridymite and thereby control lepisphere growth (Flörke *et al.*, 1976). Overall, the growth of opal-CT is poorly understood and future experimental work is required to unravel the governing processes.

2.1.3.Quartz

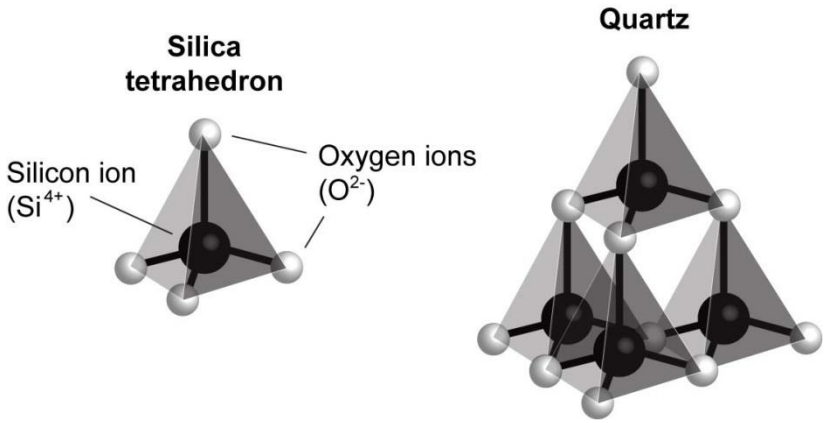


Figure 2.5: Atomic structure of a silica tetrahedron and quartz

Quartz consists of a continuous framework of silicon-oxygen tetrahedra which are made up of one silicon and four oxygen ions (Fig. 2.5). Because each oxygen ion is shared between two tetrahedra in the continuous structure of quartz, its overall formula is SiO2. Quartz is commonly divided into α- and β-quartz based on its stability. At normal pressures, α- quartz is stable below 573°C and β-quartz is stable above 573°C. Accordingly, α- quartz is transformed to β-quartz at temperatures of and above 573°C. During this transformation the silica-oxygen tetrahedra become slightly twisted, changing the symmetry of quartz from trigonal (α-quartz) to hexagonal (β-quartz).

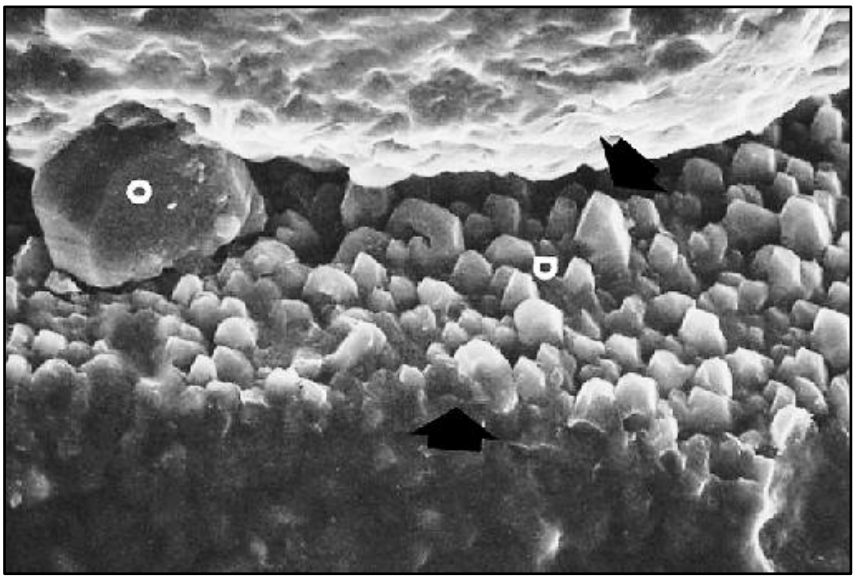


Figure 2.6: Scanning electron microscope image of authigenic quartz (Welton, 1984)

In sedimentary rocks, quartz is either detrital or authigenic in origin. Detrital quartz is usually the result of weathering, transport and deposition of quartz-rich rocks, whereas authigenic quartz is precipitated from pore fluids. The formation of authigenic quartz typically requires pore fluids to be saturated with respect to quartz and sufficient thermal energy to be provided (Heaney, 1994). If these conditions are reached, micro-crystalline quartz is precipitated, typically on the surface of pre-existing quartz grains (Fig. 2.6).

2.2. SILICA DIAGENESIS

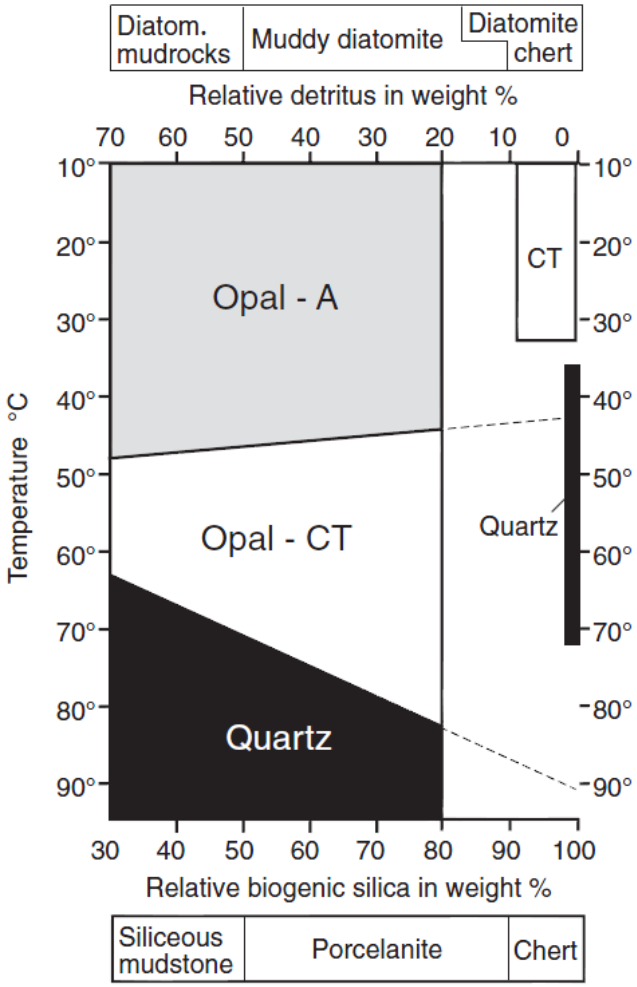


Figure 2.7: Phase diagram for silica diagenesis (Behl, 2011)

Silica diagenesis describes two transformations of opal-A to opal-CT and of opal-CT to quartz which are both dissolution/precipitation reactions (Fig. 2.7). The evidence that the opal-A/CT and opal-CT/Q transformations are dissolution/precipitation reactions have been summarised by Williams and Crerar (1985). The first and most direct piece of evidence may be scanning electron microscope images showing precipitated opal-CT in partially dissolved biogenic opal-A (Fig. 2.8).

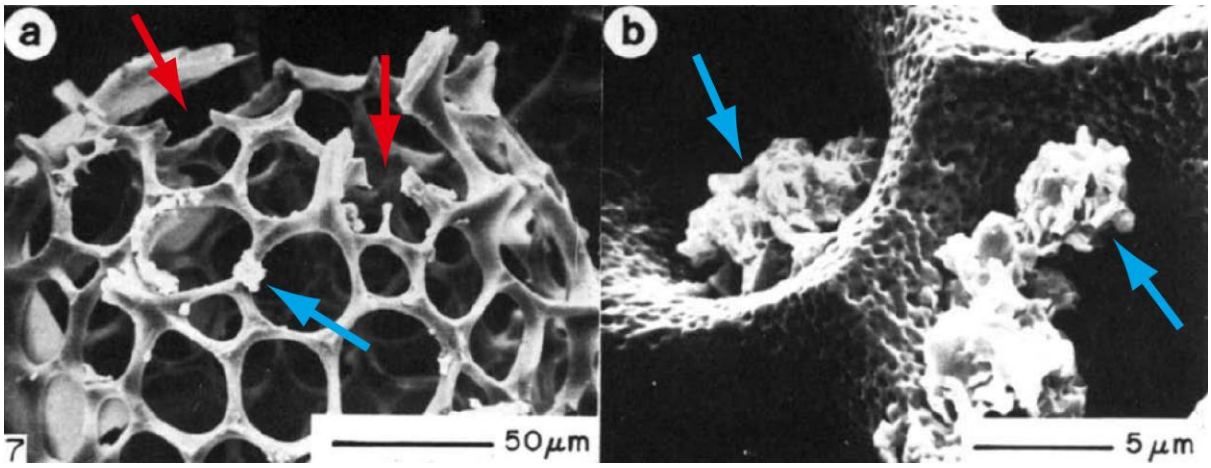


Figure 2.8: Scanning electron microscope image of: a) opal-CT lepispheres (blue arrows) on the surface of a partially-dissolved radiolarian skeleton (red arrows) and b) close-up of (a) (from Kastner *et al.*, 1977)

The second evidence is the strength of the Si-O bond. Experiments have shown that silica diagenesis occurs at energy levels far below the activation energy that is required to break the Si-O bonds (Mizutani, 1966; 1967; Ernst & Calvert, 1969; Mizutani, 1970). The third piece of evidence is that the kinetics of a first-order nucleation and growth reaction fit experimental data better than the kinetics of a zero-order solid state reaction (Stein and Kirkpatrick, 1976).

2.2.1. Kinetics

There are two approaches to the study of reaction rates (i.e. kinetics) of silica diagenesis. The first approach is to study the opal-A/CT and opal-CT/Q transformation as a whole by reproducing them under controlled conditions in the laboratory. In the laboratory, the transformation ratio is

documented at different times and temperatures to describe the transformation, for example by Arrhenius' (1889) equation:

$$k = A \cdot \exp\left(\frac{-E}{RT}\right) \tag{2.1}$$

where k is the transformation rate, A is the frequency factor, E is the activation energy, R is the gas constant, and T is the temperature. Table 2.1 summarises the kinetic parameter derived for the opal-A/CT and opal-CT/Q transformation.

Transformation	Activation energy [kcal/mol]	Frequency factor [a^{-1}]	Reference
Opal-A/CT	17.00	$6.30 \cdot 10^{9}$	Mizutani (1966)
Opal-CT/Q	14.30	$4.09 \cdot 10^{9}$	Mizutani (1966)
Opal-CT/Q	23.36	$1.17 \cdot 10^{9}$	Ernst and Calvert (1969)
Opal-CT/Q	27.49	$4.24 \cdot 10^{11}$	Dralus *et al.* (2011)

Table 2.1: Kinetic parameters of opal-A/CT and opal-CT/Q transformation

The differences between these parameters are siginificant and presumably highlight that these transformations were influenced by other factors than time and temperature, for example surface area or pH. As such these parameters may only predict the opal-A/CT and opal-CT/Q transformation under certain conditions.

The second approach is based on studying the chemical reactions during opal-A/CT and opal-CT/Q transformation separately. This involves studying opal-A and opal-CT dissolution, opal-CT and quartz precipitation, as well as a series of chemical reactions that silica undergoes in solution. It has been shown that opal-A and opal-CT dissolution is influenced by time, temperature, pressure, pH and surface area (Williams *et al.*, 1985; Hinman, 1990; Dove & Rimstidt, 1994; Icenhower & Dove, 2000). Silica dissolution strongly depends on time and temperature as the dissolution rate increases exponentially with time and temperature (Iler, 1979; Williams *et al.*, 1985; Dove & Rimstidt, 1994; Icenhower & Dove, 2000). Pressure, on the other side, hardly changes silica solubility and therefore

has a lesser influence on the dissolution (Iler, 1979; Dove & Rimstidt, 1994). Silica solubility also increases with the pH for basic solutions (Williams *et al.*, 1985; Hinman, 1990). Another influence on silica solubility is the surface area; exceptionally large surface areas of biogenic silica, for example, can strongly increase the solubility (Williams & Crerar, 1985; Williams *et al.*, 1985).

Silica precipitation is also controlled by numerous factors; including time, temperature, pH and organic content. Time and temperature appear to have a strong control on silica precipitation (Rimstidt & Barnes, 1980). It has also been suggested that the precipitation rate of opal-CT depends on the pH of the solution (Williams & Crerar, 1985). The higher the pH of the solution is, the higher is the precipitation rate of opal-CT (Kastner *et al.*, 1977). It is probably worth noting that carbonate-rich rocks usually increase the pH, whereas clay-rich rocks reduce the pH of the pore fluids. Hinman (1990) showed that organic content can cause a similar effect, as organic acids often reduce the pH of pore fluids.

2.2.2. Water release

	Opal-A	Opal-CT	Quartz
Total water content [wt.%]	8.0-17.0	3.0-10.0	0.5-2.5
Molecular water [wt.%]	7.0-16.5	2.7-9.9	0.5-1.4
Silanol groups [wt.%]	0.5-1.0	0.1-0.3	0.2-0.9
Storage type	Fluid inclusions	Atomic structure	Atomic structure

Table 2.2: Water content and storage mechanics in silica minerals (Langer & Flörke, 1974; Flörke *et al.*, 1976; Flörke *et al.*, 1982; Graetsch *et al.*, 1985; Flörke *et al.*, 1991; Graetsch *et al.*, 1994; Graetsch & Ibel, 1997; Herdianita *et al.*, 2000; DeMaster, 2003)

During silica diagenesis, the total water content decreases from opal-A to opal-CT to quartz which leads to the release of significant amounts of water (Tab. 2.2). In these minerals, water occurs in two types: as molecules or in silanol group (e.g. Langer & Flörke, 1974). It is furthermore stored in two ways; as fluid inclusions or as surface atoms (e.g. Flörke *et al.*, 1982; Flörke *et al.*, 1991).

Table 2.2 shows that the total water content is reduced by up to 14 wt.% and that the storage mechanics changes from fluid inclusions to surface atoms during opal-A/CT transformation. During

opal-CT/Q transformation, the total water content decreases by up to 7.5 wt.% as a result of a reduced amount of molecular water. The water release during silica diagenesis is important, as it may cause pore fluid overpressure and enhanced fluid flow in the host strata which in turn may trigger slope failures or sediment remobilisations (Davies & Clark, 2006; Davies *et al.*, 2006; Davies *et al.*, 2008).

2.2.3. Physical properties

Differences in the structure of opal-A, opal-CT and quartz can result in significant changes of the physical properties of the host strata during silica diagenesis. These changes can, for example, be documented in terms of host rock porosity changes (Tab. 2.3).

Reference	Region	Method	Opal-A	Opal-A/CT	Opal-CT	Opal-CT/Q	Quartz
Isaacs (1981)	Monterrey Formation, USA	Lab	63 (55-70)	30	33 (25-40)	18	15 (10-20)
Tada and Iijima (1983)	Northern Japan	Lab	65 (50-80)	<15	34 (25-42)	0	22 (10-34)
Compton (1991)	Monterrey and Sisquoc Formation, USA	Lab	56 (44-67)	25	31 (19-43)	16	15 (2-27)
Guerin and Goldberg (1996)	Offshore New Jersey, USA	Wireline	-	20	-	-	-
Chaika and Dvorkin (2000)	Monterrey Formation, USA	Lab	>55	>12	<43	-	-
Spinelli *et al.* (2007)	Shikoku Basin, offshore Japan	Wireline	60	15	45	7	38
Kim *et al.* (2007)	East Japan Sea	Wireline	71 (64-78)	17	55 (42-67)	18	36 (32-39)
Meadows and Davies (2009)	North Sakhalin Basin, Russia; Northeast Atlantic margin	Seismic	52	13 (11-14)	40 (38-41)	-	-

Table 2.3: Average porosities of opal-A, opal-CT and quartz rich sedimentary rocks and av. porosity reductions associated with the opal-A/CT and opal-CT/Q transformations. Note that all numbers are volume percentages.

Isaacs (1981) documents abrupt host rock porosity reductions associated with the opal-A/CT and opal-CT transformation in the highly-siliceous rocks of the Monterey Formation, USA (Tab. 2.3). These porosity reductions are explained by matrix collapse of the host rock due to dissolution of opal-A and opal-CT, respectively. Furthermore, Isaacs (1981) suggests that the porosity reduction during opal-CT/Q transformation is enhanced by quartz precipitation.

Tada and Iijima (1983) document a porosity reduction associated with the opal-A/CT transformation in highly-siliceous rocks of Northern Japan (Tab. 2.3). This porosity is also explained by matrix collapse of the host rock as a result of opal-A dissolution. In contrast to Isaacs (1981), Tada and Iijima (1983) observe no porosity reduction associated with the opal-CT/Q transformation. This contrast has been related to differences in host lithology, permeability, burial-, transformation rate or cementation between the siliceous rocks of Northern Japan and the USA.

Compton (1991) confirms the observation of Isaacs (1981) that the opal-A/CT and opal-CT/Q transformation are associated with abrupt porosity reductions in highly-siliceous rocks of the Monterrey and Sisquoc Formation, USA (Tab. 2.3). Furthermore, Compton (1991) highlights the influence of the initial host rock composition on silica diagenesis by suggesting that high initial opal-A contents can lead to high initial host rock porosities which are abruptly reduced during opal-A/CT transformation.

Guerin and Goldberg (1996) show that the opal-A/CT transformation can also lead to a reduction of the porosity of siliceous chalks, offshore New Jersey (Tab. 2.3). They utilise subsurface p- and s-wave velocity data to infer drastic increases in the shear- (300%) and bulk modulus (60%) of the host rock associated with the opal-A/CT transformation. These changes led them to suggest that opal-CT precipitation abruptly increases the host rock rigidity.

Chaika and Dvorkin (2000) confirm the results of Isaacs (1981) and Compton (1991) that the opal-A/CT transformation is associated with a porosity reduction in the siliceous rocks of the Monterrey Formation, USA (Tab. 2.3). Two patterns of porosity reduction are observed; a gradual and an abrupt one. Chaika and Dvorkin (2000) explain the gradual porosity reduction by authigenic clay

(smectite or illite) precipitation and the abrupt porosity reduction by silica (opal-CT or quartz) addition, rather than opal-A dissolution, as suggested by Isaacs (1981), Tada and Iijima (1983) and Compton (1991).

Spinelli *et al.* (2007) highlight the porosity reduction as well as p-wave velocity increase associated with silica diagenesis using well data from Ocean Drilling Program Sites 1173 and 1177 of the Shikoku Basin, offshore Japan (Tab. 2.3). Based on kinetic data of Mizutani (1970), Spinelli *et al.* (2007) explain the porosity reduction during opal-CT/Q transformation by rock matrix collapse due to opal-CT dissolution followed by quartz precipitation, as previously suggested by Isaacs (1981).

Kim *et al.* (2007) investigate the effect of silica diagenesis on the host rock properties using well data of Ocean Drilling program sites 127/128 in the East Japan Sea (Tab. 2.3). In addition to documenting the expected effect of silica diagenesis on the physical rock properties (porosity, density and velocity), Kim *et al.* (2007) were able to show that silica diagenesis can also lead to an increase of the electrical resistivity of the host strata.

Meadows and Davies (2009) introduce a new technique to estimate the porosity reduction during opal-A/CT transformation from seismic reflection data. This technique is based on the relief produced by the volume reduction during diagenesis. Meadows and Davies (2009) apply this technique to examples of the opal-A/CT transformation in the North Sakhalin Basin, Russia and the Faeroe-Shetland, Vøring and Møre Basins, Northeast Atlantic margin. These examples produce results in the range of values reported by previous studies (Tab. 2.3).

Thyberg *et al.* (2010) document authigenic quartz aggregates (chains, nests and clusters) in the Upper Cretaceous mudstones of the northern North Sea using scanning electron microscopy and cathodoluminescence. The precipitation of these aggregates could have been sourced by opal-A or opal-CT dissolution. Thyberg *et al.* (2010) also highlight that these aggregates coincide with density and p-wave velocity increases of the host strata.

2.2.4. Seismic studies

Studying silica diagenesis using seismic reflection data provides a new approach that nicely complements detailed, analytical studies based on well data. Silica diagenesis can be studied with seismic reflection data because the opal-A/CT and opal-CT/Q transformations lead to bulk density and p-wave velocity increases (see above) which results in positive acoustic impedance contrasts and seismic reflections.

Hein *et al.* (1978) may have been the first to relate a seismic reflection to the opal-A/CT transformation using seismic reflection data of the Bering Sea. This seismic reflection is produced by a bottom-simulating reflector; i.e. a reflector that is sub-parallel to the present seafloor (e.g. Fig. 2.9).

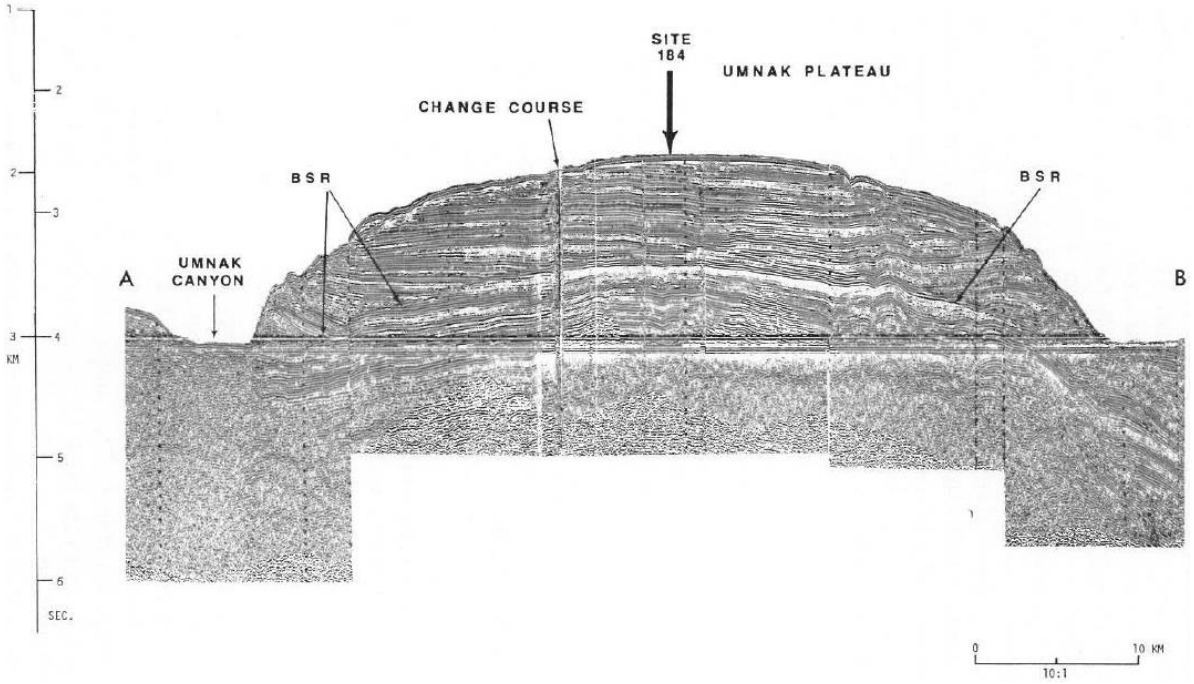


Figure 2.9: Seismic section showing the bottom-simulating reflector (BSR) associated with the opal-A/CT transformation in the Bering Sea (Hein *et al.*, 1978)

Pisciotto (1981) confirms that the opal-A/CT transformation can produce seismic reflections using seismic data of the western North Atlantic, the southern Bering Sea and the northwest Pacific. Hammond and Gaither (1983) examine the seismic reflection produced by the opal-A/CT transformation in the Bering Sea and highlight the importance of distinguishing between seismic reflections produced by silica diagenesis, sequence boundaries and fluid contacts. After these pioneer

studies, seismic reflections produced by silica diagenesis were identified in numerous sedimentary basins worldwide (Hempel *et al.*, 1989; Bohrmann *et al.*, 1992; Kuramoto *et al.*, 1992; Riis & Fjeldskaar, 1992; Mayerson & Crouch, 1994; Brekke *et al.*, 1999; Brekke, 2000). Even though these studies were able to identify 'diagenetic' reflections, it was very difficult to gain insights into silica diagenesis from the available seismic data.

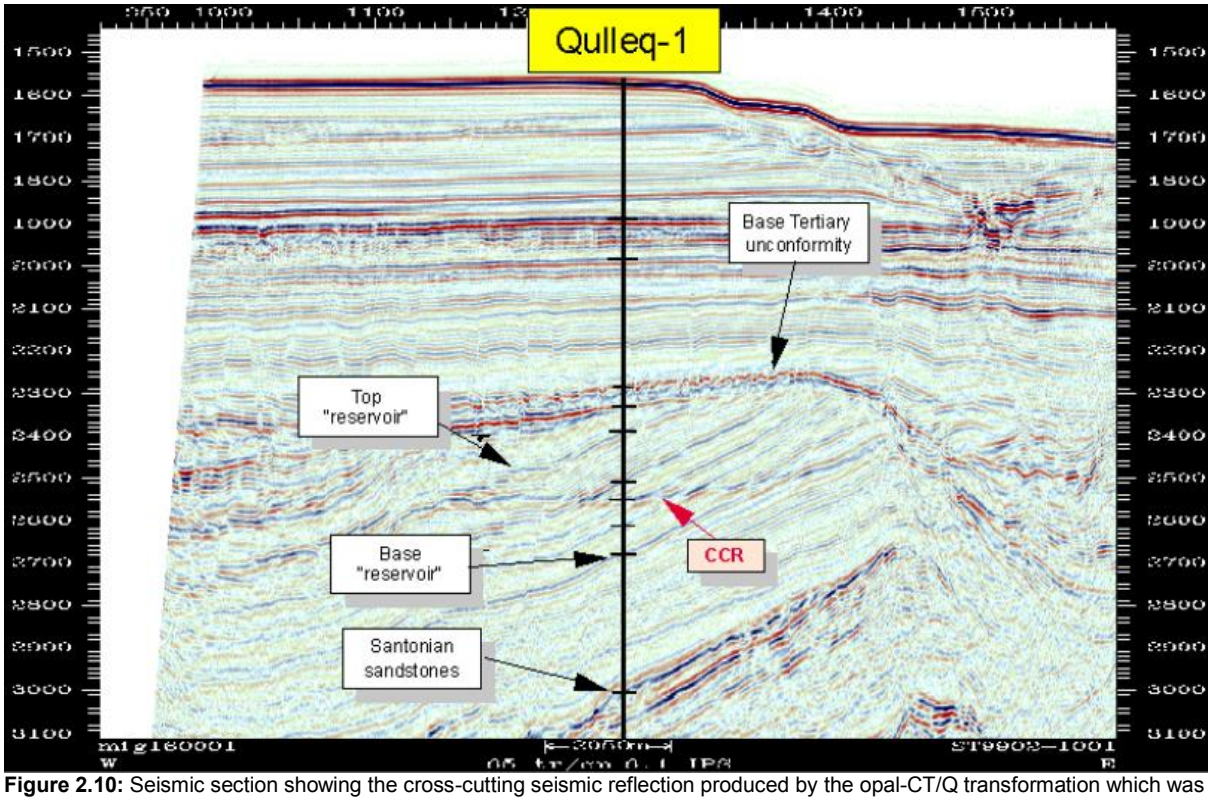


Figure 2.10: Seismic section showing the cross-cutting seismic reflection produced by the opal-CT/Q transformation which was misinterpreted as an oil-water contact and drilled by Qulleq-1 (Pegrum *et al.*, 2001).

Another set of studies was presumably motivated by the misinterpretation of a seismic reflection produced by the opal-CT/Q transformation in the Fylla area, offshore SW Greenland (Fig. 2.10). In this area, the cross-cutting seismic reflection produced by the opal-CT/Q transformation was misinterpreted as an oil-water-contact and drilled by Qulleq-1 (Fig. 2.10) (Isaacson & Neff, 1999; Pegrum *et al.*, 2001). To avoid these misinterpretations, Pedersen *et al.* (2005) and Selnes *et al.* (2013) provide amplitude-versus-offset responses of fluid contacts and silica transformations. Berndt *et al.* (2004) and Ireland *et al.* (2011) furthermore characterise seismic reflections produced by gas hydrates, silica-, clay- or carbonate diagenesis.

In addition to these studies which primarily examine the seismic expression of the opal-A/CT or opal-CT/Q transformation, several studies have focussed on deriving the extent, controls and effects of silica diagenesis using seismic reflection data. Davies and Cartwright (2002) and Neagu *et al.* (2010), for example, used seismic reflection data to map the opal-A/CT transformation over an area of 10 000 and 7800 km^2 on the Northeast Atlantic and Norwegian margin, respectively. They also use the reflection morphology to infer the age of fossilisation (cessation of upward migration) of the opal-A/CT transformation. Furthermore, Davies (2005) and Meadows and Davies (2007) use seismic reflection data to highlight the influence of the host lithology on the opal-A/CT transformation and to derive the effect of silica diagenesis on compaction (e.g. Fig. 2.11).

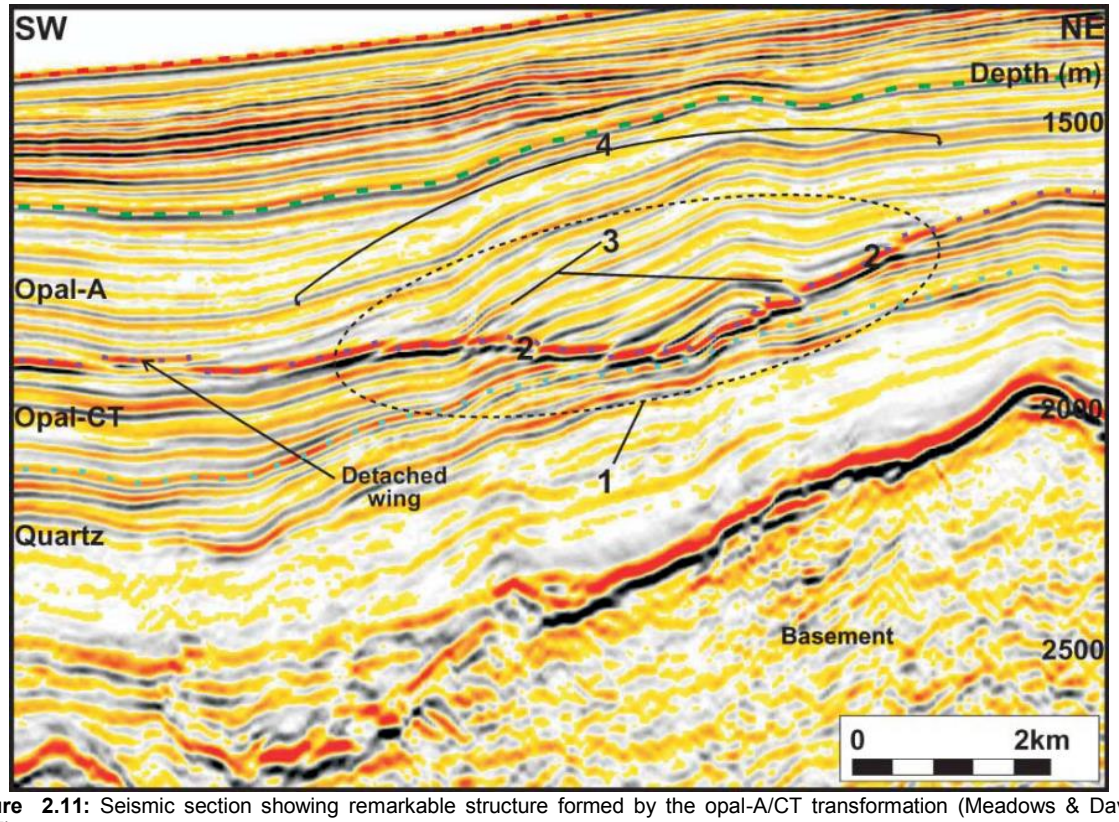


Figure 2.11: Seismic section showing remarkable structure formed by the opal-A/CT transformation (Meadows & Davies, 2007)

Seismic reflection has also been used to suggest that silica diagenesis can promote fluid flow (Davies *et al.*, 2008), prime clastic intrusions (Davies *et al.*, 2006), destabilise slopes (Volpi *et al.*, 2003; Davies & Clark, 2006), and drive polygonal faulting (Shin *et al.*, 2008; Davies *et al.*, 2009; Cartwright, 2011; Davies & Ireland, 2011). These studies provide new insights into silica diagenesis on a scale (metre to kilometre) that is difficult to cover by field and well studies.

3. STUDY AREA

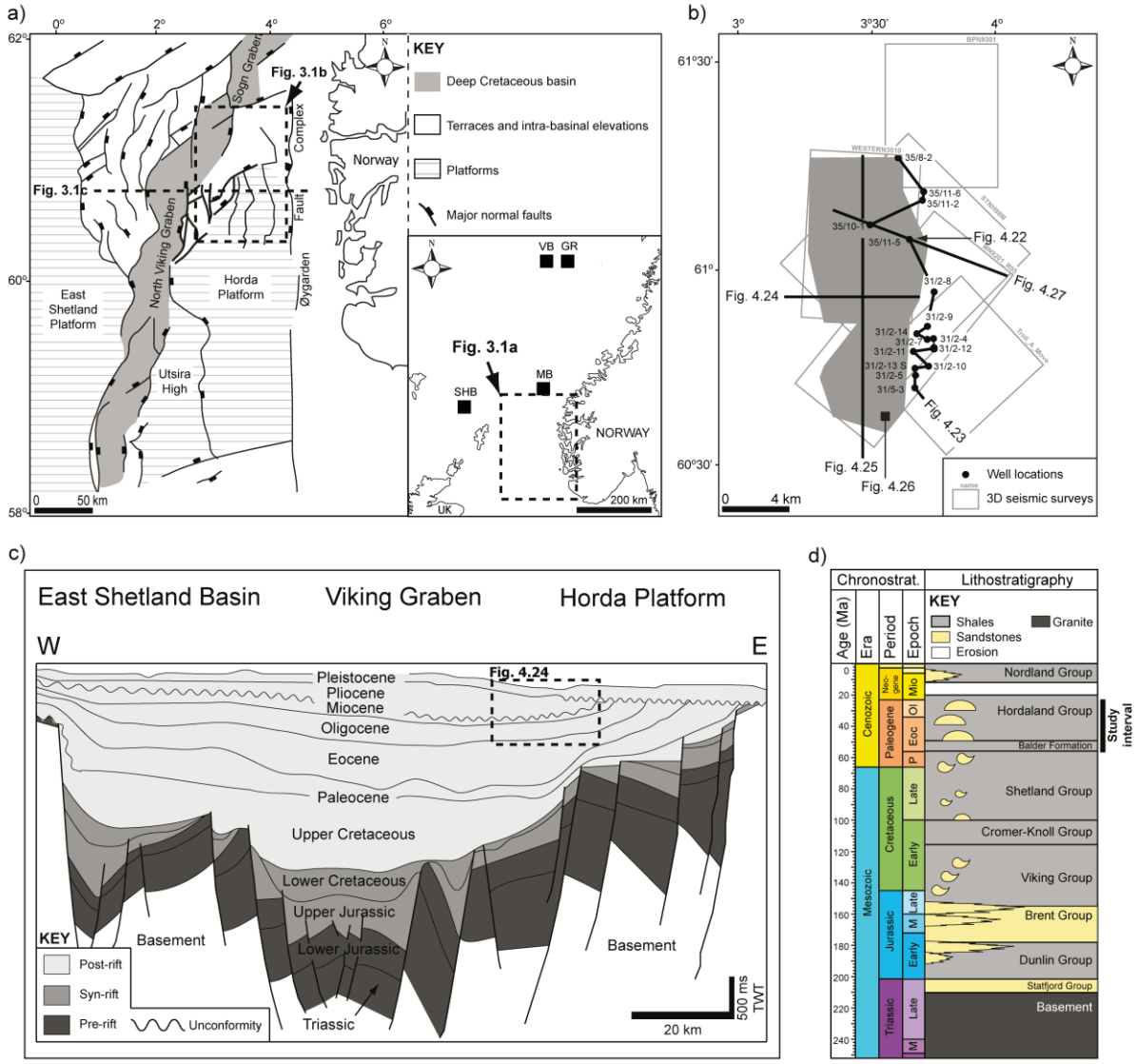


Figure 3.1: a) Simplified map of the North Viking Graben (NVG), offshore Norway, highlighting the major faults, the Horda- and East Shetland Platform (after Holgate *et al.*, 2013), the inserted regional map shows previous studies of silica diagenesis in the VB: Vøring Basin (Davies & Cartwright, 2002), GR: Gjallar Ridge (Ireland *et al.*, 2011), SHB: Faeroe-Shetland Basin (Davies, 2005)and the MB: Møre Basin (Neagu *et al.*, 2010), b) Basemap showing the surface well locations and 3-D seismic surveys used in this study, c) Geoseismic section illustrating the major faults and stratigraphic units (after Holgate *et al.*, 2013) and d) Simplified stratigraphic column for the NVG. Location of the basemap (Fig. 3.1b) and geoseismic section (Fig. 3.1c) is illustrated in Fig. 3.1a.

The study area is located in the North Viking Graben, offshore Norway (Fig. 3.1). The Viking Graben formed in the late Middle Jurassic-to-earliest Cretaceous in response to crustal extension (Fig. 3.1c). The main Late Jurassic rift phase was characterised by rapid subsidence and the formation of large-displacement normal faults that bounded graben and half-graben basins (e.g. Badley *et al.*, 1988; Yielding, 1990; Faerseth *et al.*, 1997). At the beginning of the post-rift phase, in the Early Cretaceous,

a change from fault- to thermally-controlled subsidence occurred (Joy, 1993; Brekke, 2000; Jordt *et al.*, 2000; Kyrkjebø *et al.*, 2001; Faleide *et al.*, 2002). The post-rift period was tectonically quiet, although two major uplift phases occurred in the North Viking Graben: an early Palaeocene phase, which was related to rifting, magmatism and the break-up NE Atlantic (e.g. Nadin & Kusznir, 1995), and a Middle Miocene phase which was related to the reorganisation of the North Atlantic plate (e.g. Løseth *et al.*, 2013). Understanding the tectono-stratigraphic evolution of the North Viking Graben is crucial, as it helps reconstructing the spatial and temporal evolution of silica diagenesis.

The post-rift succession in the North Viking Graben is up to 5 km thick and dominated by marine mudstones of the Shetland, Rogaland and Hordaland groups (Fig. 3.1c, d). This study focuses on the *c.* 800 m thick Hordaland Group, which was probably deposited in the distal reaches of a prograding delta (Rundberg & Eidvin, 2005). Deposition of the Hordaland Group started during the Eocene (Rundberg, 1989), with sediments primarily sourced from the Shetland-Scotland area and Scandinavia (Rundberg & Eidvin, 2005; Anell *et al.*, 2012; Eidvin *et al.*, 2014). During the Early Oligocene, Scandinavia became the dominant sediment source and a westward-thinning wedge was deposited along the western Norwegian margin (Rundberg & Eidvin, 2005; Eidvin *et al.*, 2014). This wedge, in addition to much of the Hordaland Group, consist of organic-rich, argillaceous mudstones (Rundberg & Eidvin, 2005). The Hordaland Group also contains siltstone- and sandstone-rich successions, such as the Frigg, Grid and Skade formations. These formations were primarily sourced from the Shetland-Scotland area, despite the main sediment supply having shifted, at this time, to the east (Eidvin *et al.*, 2014). During the Early Miocene, regional intra-plate shortening led to erosion of Hordaland Group mudstones above a long-wavelength dome (e.g. Rundberg & Eidvin, 2005). This uplift event and associated stratigraphic surface marks the transition from the Hordaland to the Nordland Group. Eidvin and Rundberg (2001) estimate the erosional break to last from approximately 6-17 Ma in the northern North Sea and Løseth *et al.* (2013) estimate a net erosion of less than 100 m. It is furthermore worth noting that the Early Palaeocene to Middle Miocene Hordaland Group hosts a regionally-extensive polygonal fault system that has been related to overpressure, regional extension and gravitational sliding (Rundberg, 1989; Jordt, 1996; Clausen *et al.*, 1999).

During the Pliocene and Pleistocene regional uplift of Fennoscandia resulted in a relatively rapid, volumetrically-significant influx of non-siliceous clastic material (Faleide *et al.*, 2002) and deposition of a relatively thick (up to 600 m), clinoform-bearing succession along the eastern flank of the North Viking Graben (Anell *et al.*, 2012; Ottesen *et al.*, 2012).

4. DATA & METHODS

In this study, optical- and scanning electron microscopy are used to analyse the mineralogy of the Cenozoic rocks of the North Viking Graben. Quantitative X-ray diffraction data are combined with wireline data to investigate how silica diagenesis influences the physical properties of the host strata. These analyses were undertaken on 136 cuttings samples taken at regular intervals (every 10 m) from exploration wells 35/10-1 (sampling interval: 1030-1500 m) and 35/11-5 (sampling interval: 900-1790 m) throughout the Hordaland Group. Because cuttings samples of exploration well 35/10-1 produced excellent scanning electron microscopy images of the key silica minerals (opal-A, opal-CT, quartz), optical- and scanning electron microscopy was focussed on this well. Quantitative X-ray diffraction, on the other side, was conducted on samples of both wells (35/10-1 and 35/11-1). These wells were chosen because they offered a suite of complete, high-quality wireline logs that are used to assess the influence silica diagenesis on the physical properties of the host strata. Although correct depth attribution of cuttings can be problematic due to borehole caving, the consistency of the presented data and the absence of outliers indicate that cuttings were correctly depth referenced.

4.1. OPTICAL MICROSCOPY

For an initial assessment of the rock textures, ten polished thin sections (30 μm) were made of cuttings from exploration well 35/10-1 at the Natural History Museum (Fig. 4.1.). These thin sections were analysed with an optical microscope (Brunel SP1500XP) using plane, plane-reflected and cross-polarised light. Different objectives allow magnifications of 5, 10, 40 and 60.

Well 35/10-1

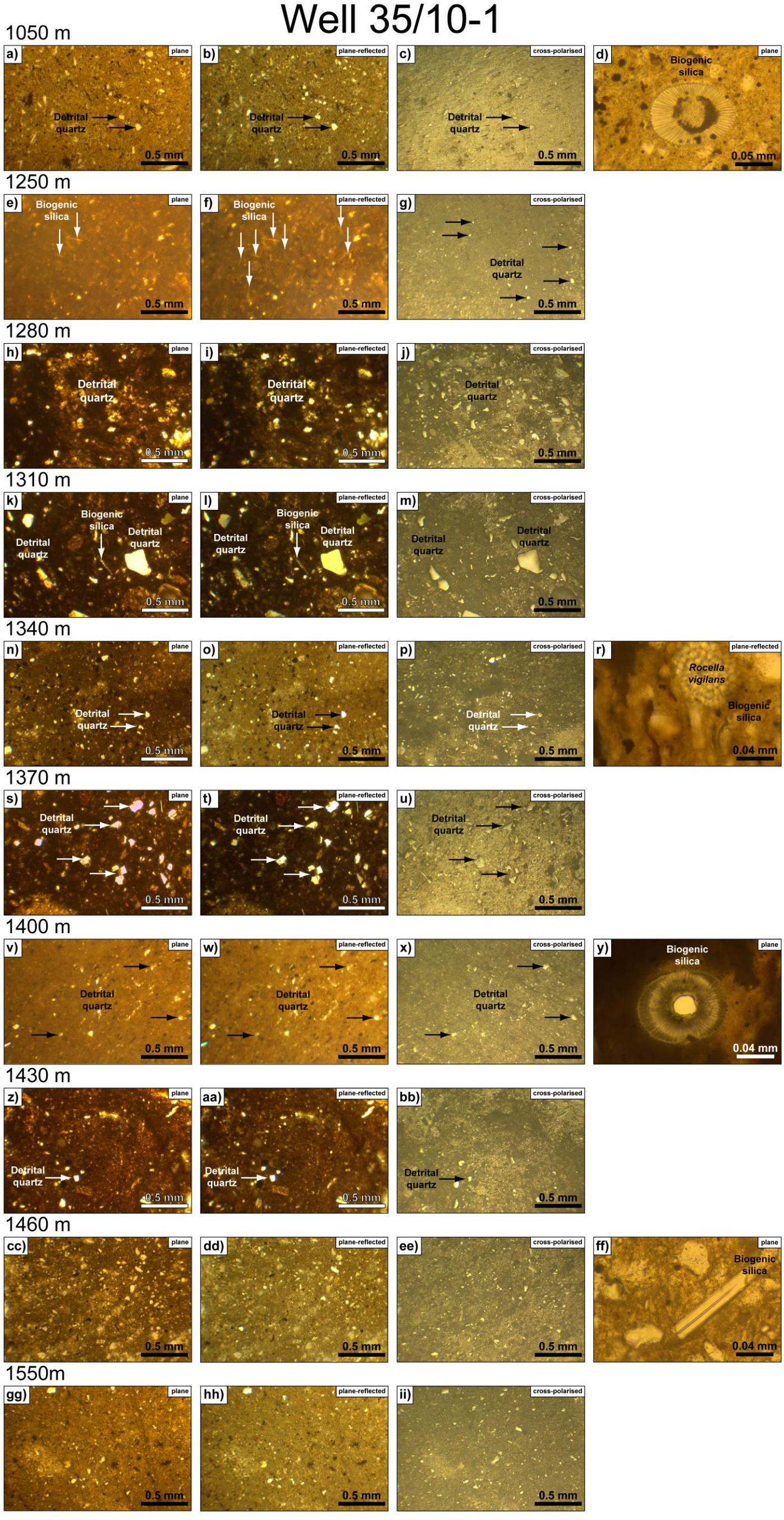


Figure 4.1: Thin section images of plane, plane-reflected and cross-polarised light for exploration well 35/10-1. Note the presence of biogenic opal-A as well as angular, macroscopic quartz grains (0.01-0.2 mm).

4.2. SCANNING ELECTRON MICROSCOPY

Scanning electron microscopy was conducted on cuttings samples from exploration well 35/10-1 to identify the key minerals (opal-A, opal-CT and quartz) based on their textural and morphological characteristics (Fig. 4.2). The samples were prepared by gluing part of the cutting samples to a stub using slow-drying araldite. The samples were silver-coated to avoid artefacts induced by electron build-ups. A Carl Zeiss Ultra Plus Field Emission scanning electron microscope belonging to the Natural History Museum was operated at 5 kV with an aperture size of 30 μm. This microscope has a magnification of up to 100 000 (i.e. a resolution of up to 10 nm), allowing opal-A, opal-CT and quartz to be observed in great detail. The microscope is equipped with an Oxford instruments X-Max energy dispersive X-ray detector that was used to determine the chemical composition of the samples (atomic number greater than five) with a detection limit of the order to 0.2 wt.%.

Well 35/10-1

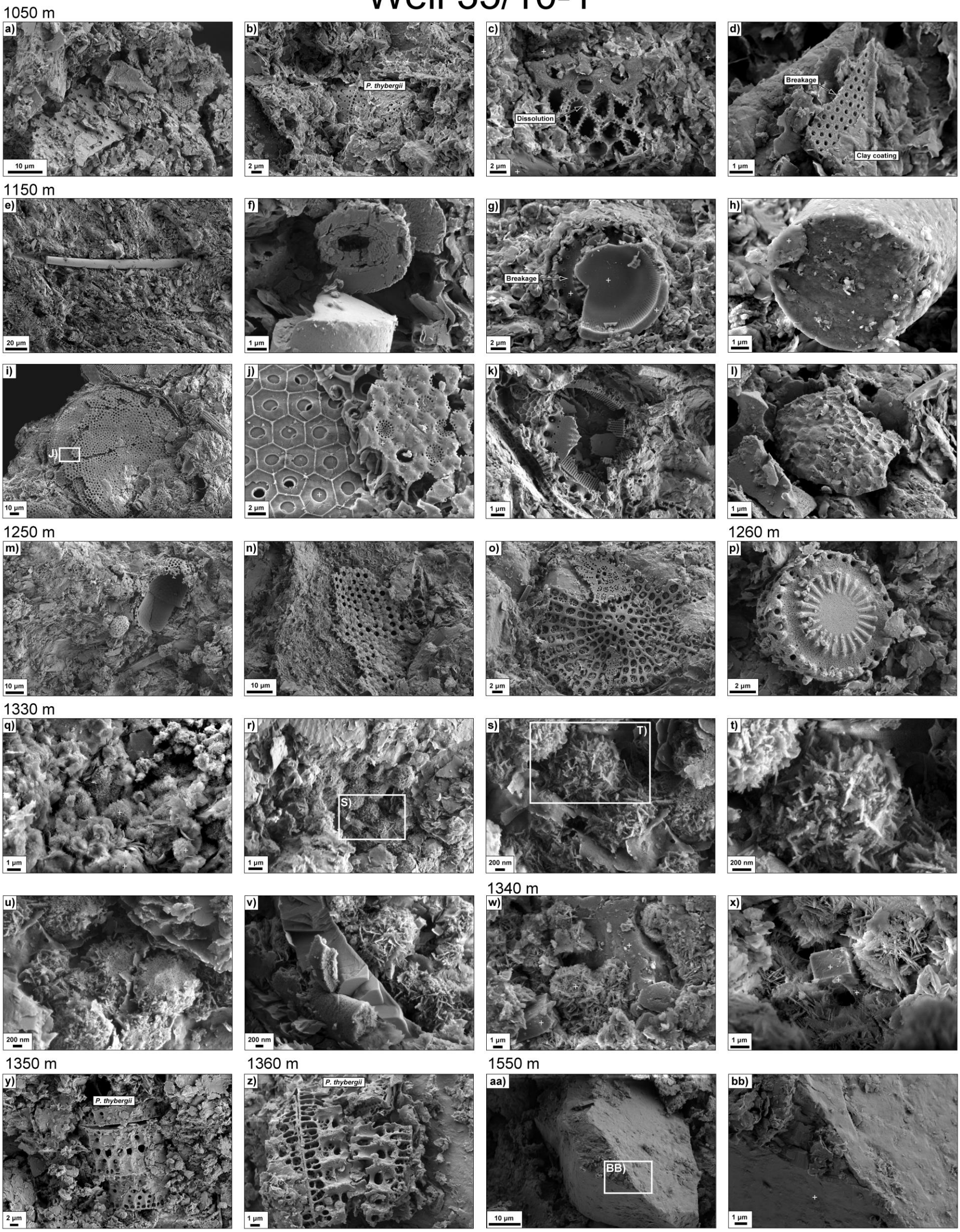


Figure 4.2: Scanning electron microscopy images of cutting samples of exploration well 35/10-1. Note the presence of opal-A (at various depths), opal-CT (at 1330 m) and macroscopic quartz (at 1550 m). White crosses correspond to energy dispersive X-ray diffractograms which are shown on Figure 8.1.

4.3. X-RAY DIFFRACTION

X-ray diffraction was applied to identify and quantify the composition of 136 cuttings samples of wells 35/10-1 and 35/11-5. Sample preparation, analysis and mineral identification are based on Brown *et al.* (1980), Moore and Reynolds (1997), and Hillier (2002). The quantification is based on the whole-pattern-stripping method of Cressey and Schofield (1996) and Batchelder and Cressey (1998). Measurements were conducted on unoriented powder samples using an Enraf-Nonius PDS 120 diffractometer with a curved position-sensitive detector configured in vertical geometry with a 2Θ detection range of 0-120° (Natural History Museum). $CuK\alpha_1$ radiation was selected using a germanium 111 monochromator. Tube-operating conditions were 45 kV and 45 mA with slits restricting the beam to 0.24×5.0 mm (horizontally/vertically) and an acquisition time of 30 min per sample. 2Θ linearisation was conducted using a least-square cubic spline function. Additionally, clay fractions (< 2 μm) of five oriented samples of exploration well 35/10-1 (depth: 1050, 1150, 1250, 310 and 1510 m) were measured after being air-dried, ethylene glycolated, heated to 400°C and heated to 500°C, respectively (Fig. 4.3).

4.3.1. Identification

Clay-, silica- and other minerals were identified by X-ray diffraction. In this study, clay mineral groups rather than specific minerals are discerned. For instance, the presence of smectite is, in accordance with Moore and Reynolds (1997), inferred from the change of the 001 peak from ~5.2° in ethylene glycolated to ~6° in air-dried to ~10° in heated samples (Fig. 4.3). It is furthermore inferred that smectite occurs in mixed-layer illite-smectite rather than in isolation, as the 001 peak in glycolated samples is diffuse rather sharp (Hillier, 2002) (Fig. 4.3). In accordance with Moore and Reynolds (1997), the presence of illite is inferred from characteristic peaks around 9, 18 and 26° (Fig. 4.3). Kaolinite is identified by peaks around 12.3 and 24.9° and discerned from chlorite based on the absence of a peak around 6.3° and the disappearance of the 001 peak during heating to 500°C (Fig. 4.3).

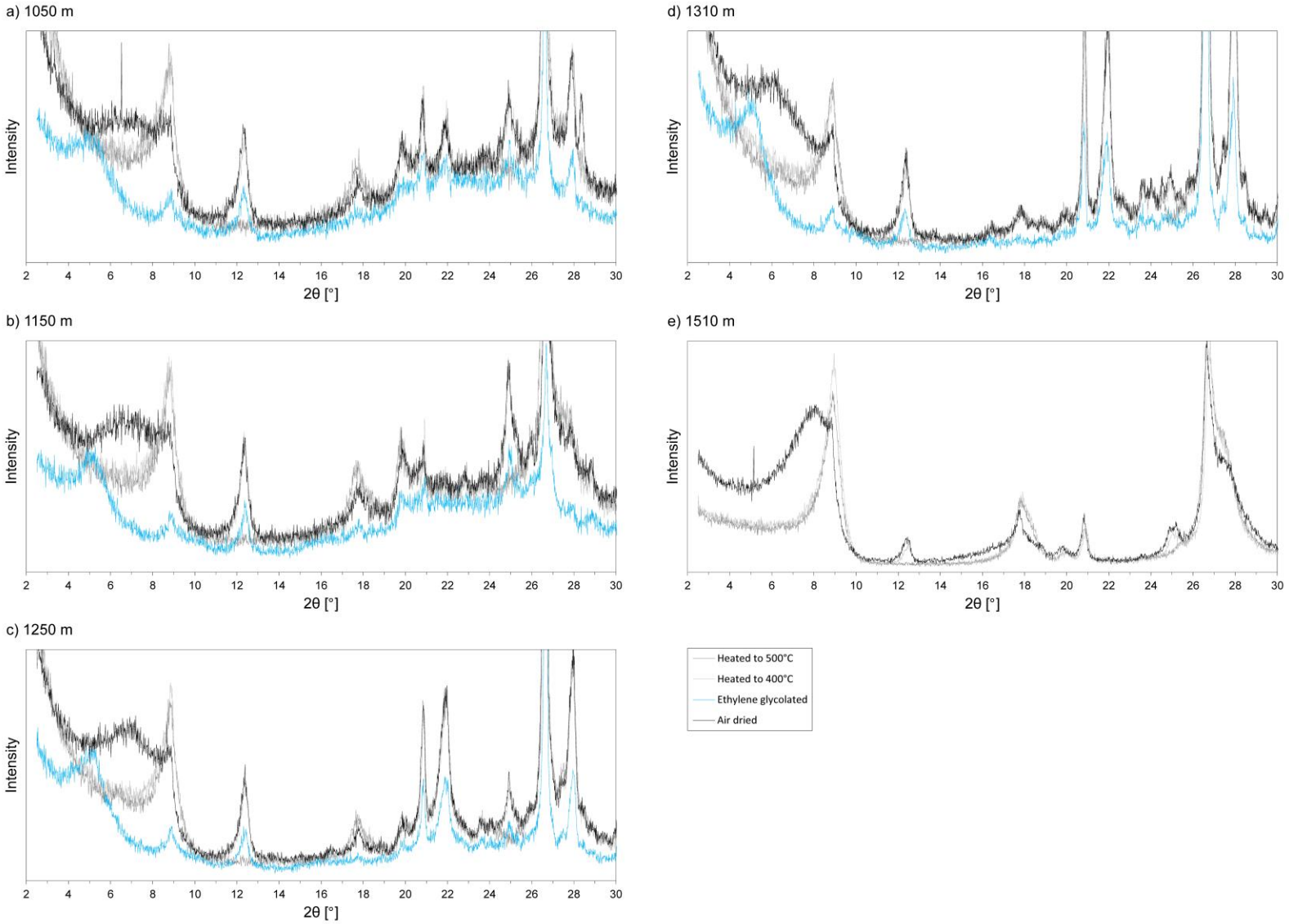


Figure 4.3: X-ray diffractograms of cuttings samples of exploration well 35/10-5 at a) 1050 m, b) 1150 m, c) 1250 m, d) 1310 m and e) 1510 m depth.

Signatures of opal-A, opal-CT and quartz are also observed by X-ray diffraction. The X-ray diffraction pattern of opal-A is a diffuse band between ~10-40° (e.g. Figs. 4.3a,b; 4.4) (Jones & Segnit, 1971; von Rad *et al.*, 1978). Opal-CT is identified from on the asymmetric double-peak between 20-21.5° (e.g. Figs.4.3c,d; 4.4) (Jones & Segnit, 1971; Flörke *et al.*, 1975; Guthrie *et al.*, 1995) and quartz is identified based on the strong 001 peak at 26.6° (e.g. Fig. 4.3, 4.4) (Moore & Reynolds, 1997). The presence of calcite and pyrite is derived from peaks around 29.4 and 33°, respectively, while the presence of barite, sylvite and halite is inferred from peaks 42.8, 28.3 and 31.7, respectively (Swanson *et al.*, 1953; Moore & Reynolds, 1997). The identified minerals and their characteristic features are summarised in Table 4.1.

Minerals	Diagnostic features	2θ [°]	d-spacing [Å]	References
Illite-Smectite	001 peak shift			Moore and Reynolds (1997), Hillier (2002)
	Ethylene glycolated	~5.2	~17	
	Air-dried	~6	~15	
	Heated	~10	~9	
	Diffuse 001 peak Ethylene glycolated			
Illite	001 peak	~9	~10	Moore and Reynolds (1997), Hillier (2002)
	002 peak	~18	~5	
	003 peak	~26	~3.38	
Kaolinite	001 peak	12.3	7.17	Moore and Reynolds (1997), Hillier (2002)
	002 peak	24.9	3.58	
Opal-A	Diffuse band	~10-40	~2.2-8.8	Jones and Segnit (1971) , von Rad *et al.* (1978)
Opal-CT	Asymmetric double-peak	20 & 21.5	4.13-4.44	Jones and Segnit (1971), Flörke *et al.* (1975), Guthrie *et al.* (1995)
Quartz	001 peak	26.6	3.343	Moore and Reynolds (1997)
Calcite	Peak	29.4	3.035	Moore and Reynolds (1997)
Pyrite	200 peak	33	2.709	Moore and Reynolds (1997)
Barite	Peak	42.8	2.11	Swanson *et al.* (1953)
Sylvite	Peak	28.3	3.15	Swanson *et al.* (1953)
Halite	Peak	31.7	2.82	Swanson *et al.* (1953)

Table 4.1: Minerals identified based on their diagnostic features.

4.3.2.Quantification

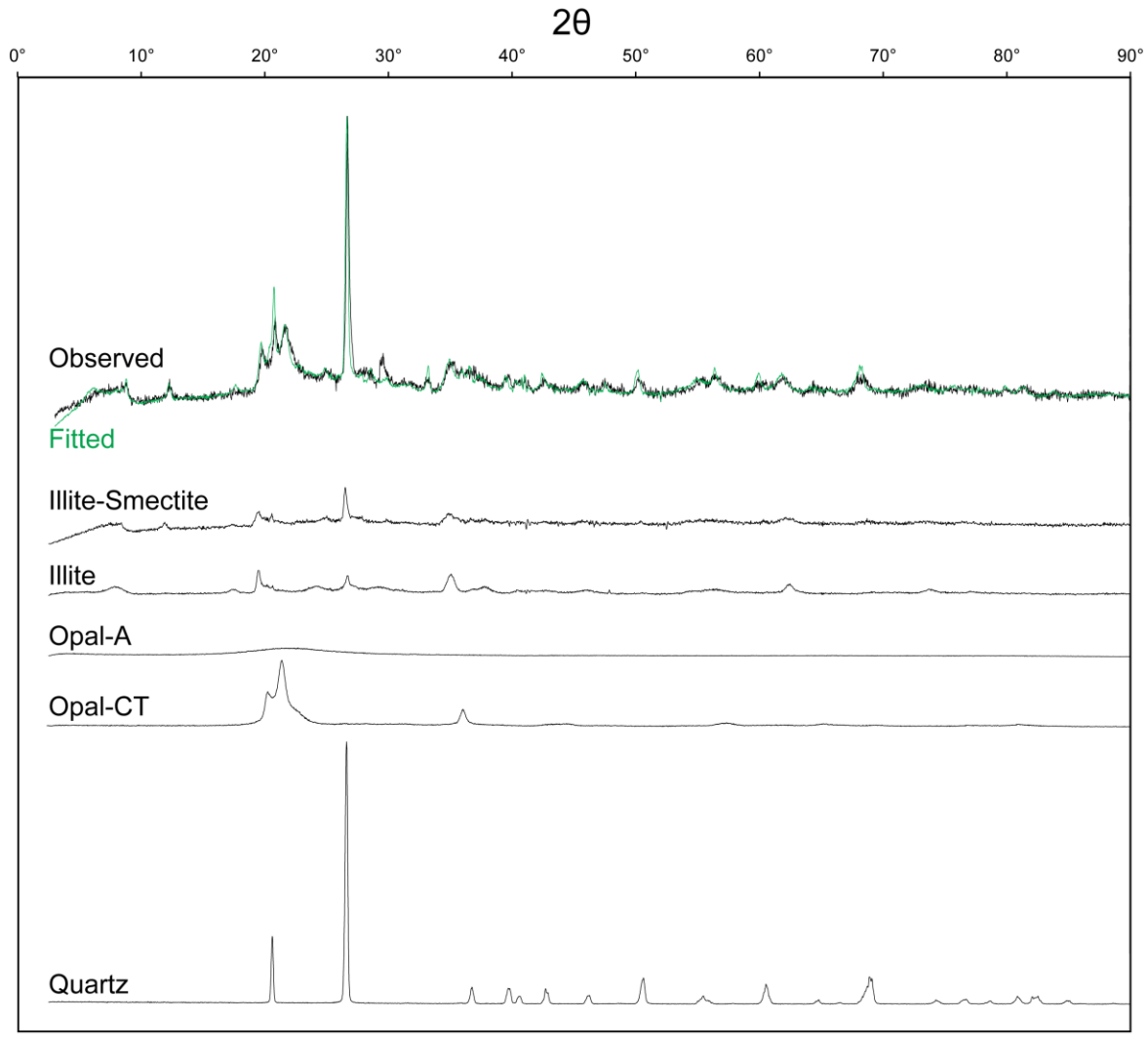


Figure 4.4: Example of X-ray diffractograms showing the observed pattern of measured sample (top black), the fitted composite pattern of identified minerals (top green) and pattern of identified minerals (illite-smectite, illite, opal-A, opal-CT and quartz).

After identifying the minerals present in the samples, their contribution to the whole rock is quantified using the whole-pattern-stripping method described by Cressey and Schofield (1996). This method has been extended to clay-bearing samples by Batchelder and Cressey (1998). Following this method, diffraction patterns of the identified minerals were measured on standards of the Natural History Museum under the same conditions used to measure the samples (see above). Diffraction patterns of the samples are matched to composites of diffraction patterns of identified minerals (Fig. 4.4). In technical terms, the difference between these patterns are minimalized by changing the intensity ratios between them using a generalised reduced gradient algorithm (e.g. Lasdon *et al.*,

1978). This algorithm delivers intensity ratios between diffraction patterns of minerals and samples. These ratios are used to calculate the volume fractions of these mineral in the sample using the correction of Batchelder and Cressey (1998):

$$x_i = \frac{v_i(\mu''/\mu_i)}{\sum_i v_i\,(\mu''/\mu_i)} \tag{4.1}$$

x_i – Volume fraction of phase i

v_i – Intensity ratio between phase i and sample

μ'' – Apparent matrix absorption coefficient

μ_i – Absorption coefficient of phase i

with the absorption coefficients listed in Tab. 4.2.

		Elements			Minerals	
Atomic Number [cm^2/g]	Symbol	Standard atomic weight	Absorption coefficient [cm^2/g]	Name	Chemical formula	Absorption coefficient
1	H	1.008	0.40	Opal-A	SiO_2	34.84
6	C	12.011	4.30	Opal-CT	SiO_2	34.84
8	O	15.999	10.94	Quartz	SiO_2	34.84
11	Na	22.990	15.74	Smectite	$Na_{0.2}Ca_{0.1}Al_2Si_4O_{10}(OH)_2(H_2O)_{10}$	34.59
13	Al	26.982	39.04	Illite/Smectite	-	36.70
14	Si	28.085	48.67	Illite	$K_{0.6}(H_3O)_{0.4}Al_{1.3}Mg_{0.3}Fe^{2+}_{0.1}Si_{3.5}O_{10}(OH)_2{\cdot}(H_2O)$	38.80
16	S	32.066	62.07	Kaolinite	$Al_2Si_2O_5(OH)_4$	29.79
17	Cl	35.451	89.70	Calcite	$CaCO_3$	71.51
19	K	39.098	102.74	Pyrite	FeS_2	192.69
20	Ca	40.078	138.48	Barite	BaSO	219.35
26	Fe	55.845	164.19	Sylvite	KCl	121.49
56	Ba	137.327	310.94	Halite	NaCl	73.70

Table 4.2: Absorption coefficients of chemical elements and minerals calculated according to Batchelder and Cressey (1998).

By repeating this procedure for all cuttings samples, the composition is determined (Figs. 4.5, 4.6). Batchelder and Cressey (1998) estimate the precision of this method to be ±3% in clay-bearing samples lacking an amorphous phase. Because opal-A produces a broad band rather than a sharp peak such as crystalline phases, the applied method is probably less certain. Unfortunately, the uncertainty of this method when applied to amorphous phases has not been quantified. Conley (1998) however suggest that opal-A contents derived by X-ray diffraction (e.g. Eisma & Van der Gaast, 1971) typically exceed opal-A contents derived by wet-chemical digestion techniques by >10%.

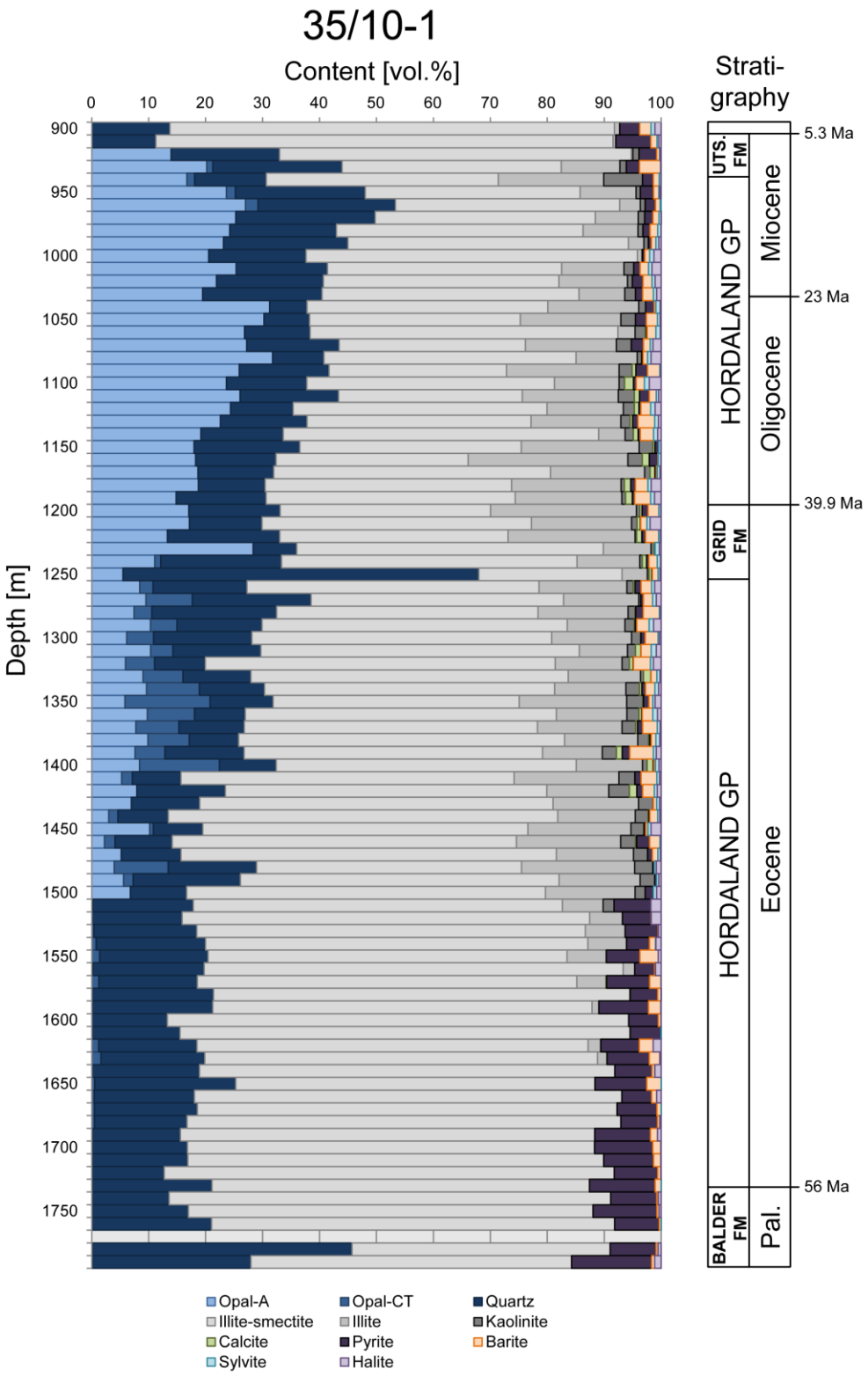


Figure 4.5: Mineral content (in vol. %) of cuttings sample from 900-1790 m depth in exploration well 35/10-1 derived by X-ray diffraction.

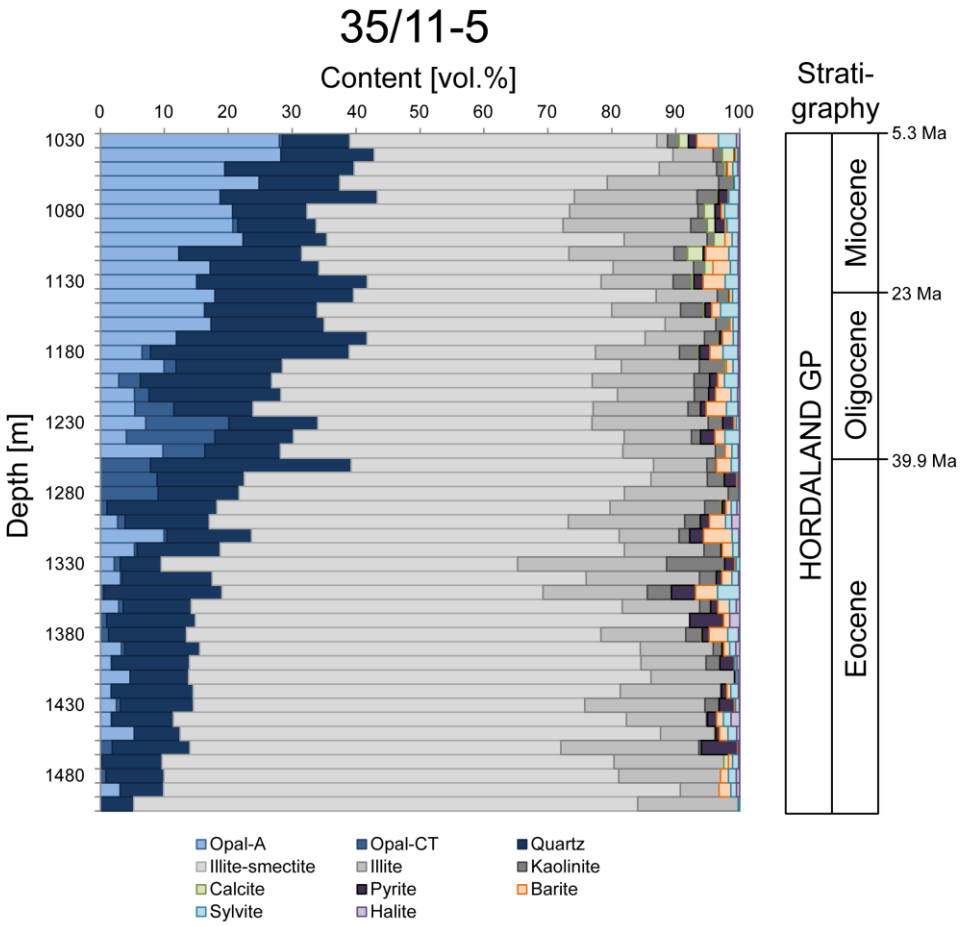


Figure 4.6: Mineral content (in vol. %) of cuttings sample from 1030-1500 m depth in exploration well 35/11-5 derived by X-ray diffraction.

4.4. MINERALOGICAL DATA

4.4.1. Descriptive statistics

This section contains a statistical description of the quantitative X-ray diffraction data. While Figures 4.7 and 4.8 show data of exploration well 35/10-1 and 35/11-5, respectively, Tables 4.3 and 4.4 contain the corresponding statistics.

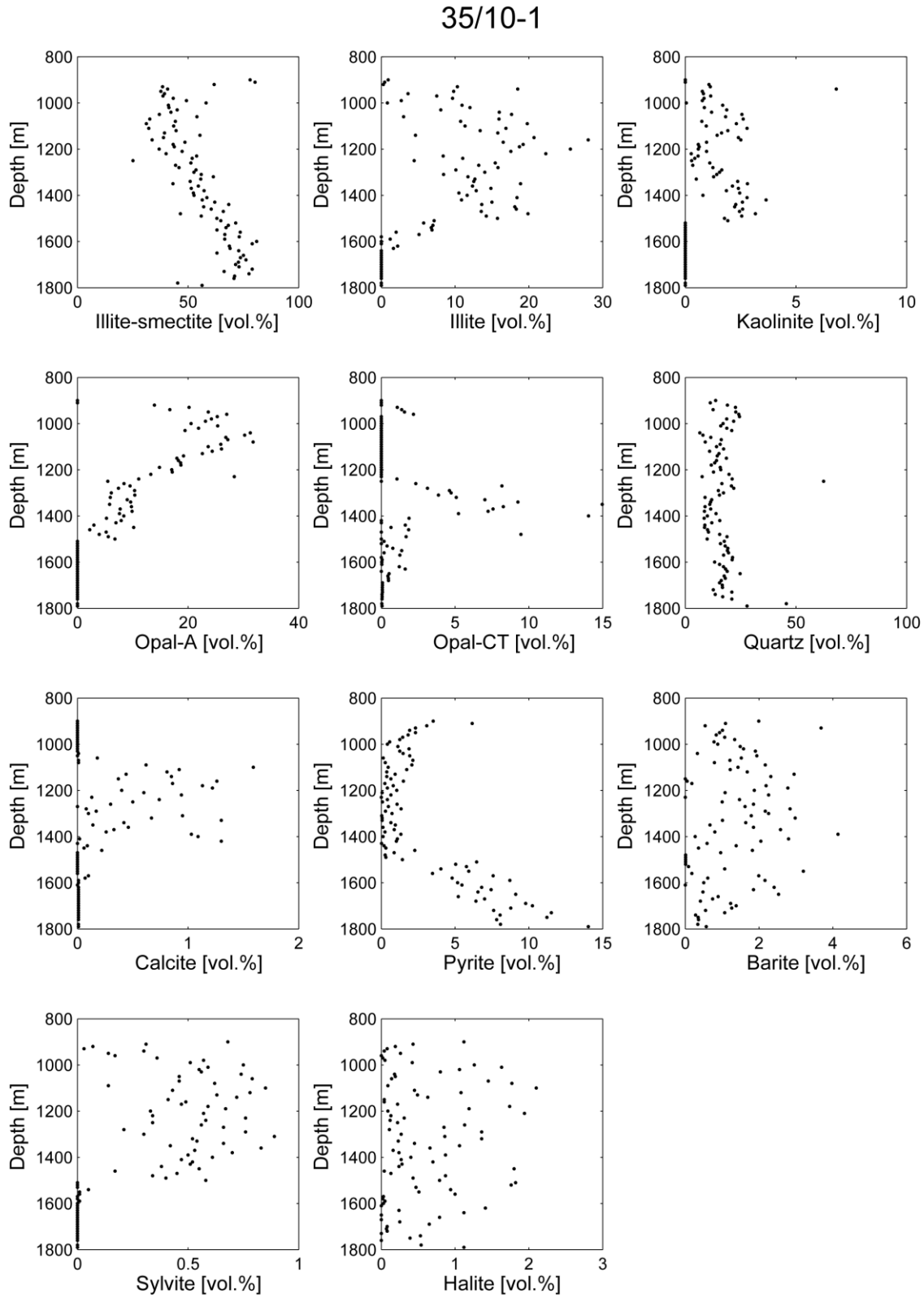


Figure 4.7: Mineral contents with depth of well 35/10-1.

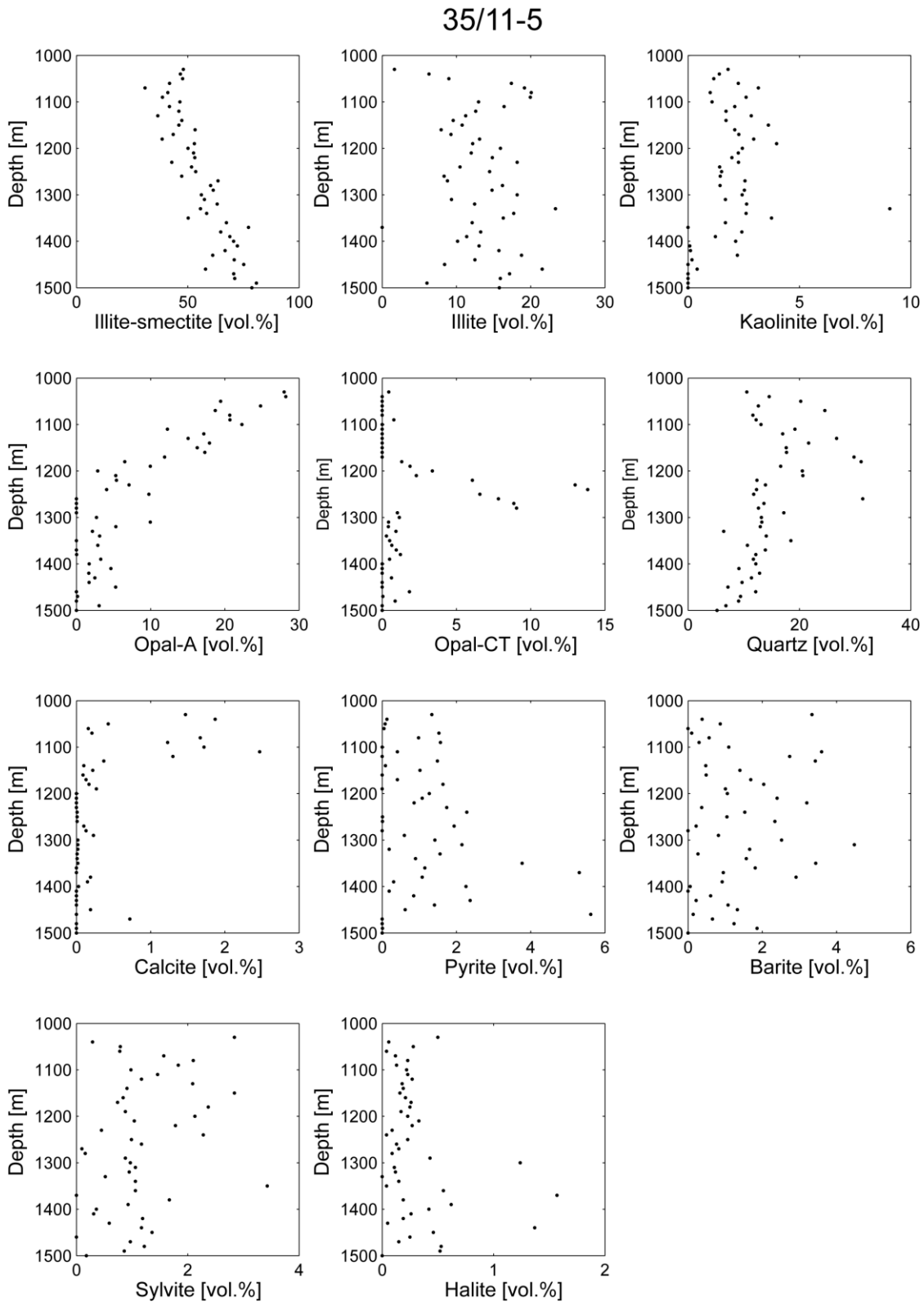


Figure 4.8: Mineral contents with depth of well 35/11-5.

	n	min	max	range	mean	var	sd	skew	kurtosis	se
Illite-Smectite	89	25.12	81.01	55.9	55.59	192.65	13.88	0.03	-1.06	1.47
Illite	89	0	28.04	28.04	9.35	54.61	7.39	0.19	-1.03	0.78
Kaolinite	89	0	6.82	6.82	1.12	1.42	1.19	1.44	3.93	0.13
Opal-A	89	0	31.76	31.76	10.27	101.81	10.09	0.54	-1.11	1.07
Opal-CT	89	0	14.97	14.97	1.57	9.49	3.08	2.47	6.02	0.33
Quartz	89	6.56	62.51	55.94	16.58	54.76	7.4	3.26	16.72	0.78
Calcite	89	0	1.59	1.59	0.26	0.17	0.41	1.52	1.09	0.04
Pyrite	89	0	14.03	14.03	3.05	11.49	3.39	1.15	0.3	0.36
Barite	89	0	4.14	4.14	1.29	0.88	0.94	0.59	-0.18	0.1
Sylvite	89	0	0.89	0.89	0.35	0.08	0.28	0.03	-1.44	0.03
Halite	89	0	2.1	2.1	0.58	0.33	0.57	0.94	-0.21	0.06

Table 4.3: Statistics of mineralogical data of exploration well 35/10-1 with n – number of samples, min – minimum, max – maximum, range – range, mean – arithmetic mean, var – variance, sd – standard deviation, skew – skewness, kurtosis – kurtosis and se – standard error.

	n	min	max	range	mean	var	sd	skew	kurtosis	se
Illite-Smectite	48	30.86	80.84	49.99	55.85	152.03	12.33	0.2	-0.92	1.78
Illite	48	0	23.34	23.34	13.19	23.33	4.83	-0.36	0.11	0.7
Kaolinite	48	0	9.06	9.06	1.88	2.28	1.51	2.05	8.4	0.22
Opal-A	48	0	28.22	28.22	8.17	72.08	8.49	0.85	-0.59	1.23
Opal-CT	48	0	13.84	13.84	1.81	11.49	3.39	2.21	3.99	0.49
Quartz	48	5.21	31.38	26.16	14.91	37.33	6.11	1.09	0.78	0.88
Calcite	48	0	2.47	2.47	0.33	0.36	0.6	2.04	3.05	0.09
Pyrite	48	0	5.62	5.62	1.08	1.59	1.26	1.85	3.89	0.18
Barite	48	0	4.48	4.48	1.34	1.35	1.16	0.82	-0.3	0.17
Sylvite	48	0	3.43	3.43	1.15	0.59	0.77	0.87	0.46	0.11
Halite	48	0	1.57	1.57	0.3	0.10	0.32	2.45	5.99	0.05

Table 4.4: Statistics of mineralogical data of exploration well 35/11-5 with n – number of samples, min – minimum, max – maximum, range – range, mean – arithmetic mean, var – variance, sd – standard deviation, skew – skewness, kurtosis – kurtosis and se – standard error.

These statistics are calculated according to standard definitions (see Everitt & Skrondal, 2002) in R (2014), i.e. the arithmetic mean ($\bar{x}$) is:

$$\bar{x} = \frac{1}{n}\sum_{i=1}^{n} x_i \tag{4.2}$$

where x are the sample values and n is the number of samples. The (unbiased) sample variance (σ_x^2) and standard deviation (σ_x) are:

$$\sigma_x^2 = \frac{1}{n-1}\sum_{i=1}^{n}(x_i - \bar{x})^2 \tag{4.3}$$

The skewness (b_1) is:

$$b_1 = \frac{m_3}{\sigma_x^3} \tag{4.4}$$

$$m_3 = \frac{1}{n}\sum_{i=1}^{n}(x_i - \bar{x})^3 \tag{4.5}$$

The kurtosis (b_2) is:

$$b_2 = \frac{m_4}{\sigma_x^4} - 3 \tag{4.6}$$

$$m_4 = \frac{1}{n}\sum_{i=1}^{n}(x_i - \bar{x})^4 \tag{4.7}$$

The standard error (se) is:

$$se = \frac{\sigma_x}{\sqrt{n}} \tag{4.8}$$

4.4.2.Correlation

To explore for mineral transformations, mineral contents are cross-plotted and correlation coefficients are calculated using R (2014). The Pearson (1895) correlation coefficient (r_{xy}) is:

$$r_{xy} = \frac{c_{xy}}{\sigma_x \sigma_y} \tag{4.9}$$

with:

$$c_{xy} = \frac{1}{n-1}\sum_{i=1}^{n}(x_i - \bar{x})(y_i - \bar{y}) \tag{4.10}$$

where c_{xy} is the (unbiased) covariance of two sample sets x_i and y_i.



Figure 4.9: Cross-plots between mineral contents in exploration well 35/10-1, ordered and coloured by the absolute value of the correlation coefficients (yellow: 0-0.16, green: 0.17-0.39, red: 0.40-1.00).

	Barite	Opal-CT	Quartz	Kaolinite	Sylvite	Pyrite	Illite	Illite-Smectite	Opal-A	Depth	Calcite	Halite
Barite	1.00	0.10	-0.04	0.11	0.19	-0.17	0.18	-0.22	0.10	-0.22	0.26	0.02
Opal-CT	0.10	1.00	-0.21	0.26	0.27	-0.31	0.26	-0.13	-0.12	0.04	0.17	0.03
Quartz	-0.04	-0.21	1.00	-0.33	-0.36	0.26	-0.34	-0.20	-0.16	0.11	-0.12	-0.15
Kaolinite	0.11	0.26	-0.33	1.00	0.43	-0.54	0.65	-0.47	0.36	-0.37	0.19	0.01
Sylvite	0.19	0.27	-0.36	0.43	1.00	-0.80	0.53	-0.50	0.62	-0.62	0.49	0.31
Pyrite	-0.17	-0.31	0.26	-0.54	-0.80	1.00	-0.70	0.60	-0.62	0.68	-0.43	-0.17
Illite	0.18	0.26	-0.34	0.65	0.53	-0.70	1.00	-0.68	0.48	-0.45	0.44	0.10
Illite-Smectite	-0.22	-0.13	-0.20	-0.47	-0.50	0.60	-0.68	1.00	-0.78	0.67	-0.38	-0.07
Opal-A	0.10	-0.12	-0.16	0.36	0.62	-0.62	0.48	-0.78	1.00	-0.82	0.27	0.10
Depth	-0.22	0.04	0.11	-0.37	-0.62	0.68	-0.45	0.67	-0.82	1.00	-0.23	-0.10
Calcite	0.26	0.17	-0.12	0.19	0.49	-0.43	0.44	-0.38	0.27	-0.23	1.00	0.16
Halite	0.02	0.03	-0.15	0.01	0.31	-0.17	0.10	-0.07	0.10	-0.10	0.16	1.00

Table 4.5: Ordered correlation coefficients between mineral contents and depth of exploration well 35/10-1.



Figure 4.10: Cross-plots between mineral contents in exploration well 35/11-5, ordered and coloured by the absolute value of the correlation coefficients (yellow: 0-0.16, green: 0.17-0.39, red: 0.40-1.00).

	Opal-CT	Pyrite	Barite	Sylvite	Kaolinite	Quartz	Illite-Smectite	Depth	Opal-A	Calcite	Halite	Illite
Opal-CT	1.00	0.10	-0.06	-0.05	0.03	0.04	-0.11	-0.03	-0.27	-0.24	-0.19	0.03
Pyrite	0.10	1.00	0.05	0.05	0.08	-0.02	0.05	0.22	-0.29	-0.22	0.27	0.04
Barite	-0.06	0.05	1.00	0.55	0.08	0.27	-0.18	-0.13	0.02	0.15	0.10	-0.26
Sylvite	-0.05	0.05	0.55	1.00	0.21	0.28	-0.44	-0.33	0.24	0.19	-0.13	0.01
Kaolinite	0.03	0.08	0.08	0.21	1.00	0.22	-0.44	-0.31	0.08	-0.06	-0.33	0.32
Quartz	0.04	-0.02	0.27	0.28	0.22	1.00	-0.65	-0.52	0.21	0.02	-0.15	-0.15
Illite-Smectite	-0.11	0.05	-0.18	-0.44	-0.44	-0.65	1.00	0.87	-0.67	-0.41	0.41	-0.21
Depth	-0.03	0.22	-0.13	-0.33	-0.31	-0.52	0.87	1.00	-0.85	-0.56	0.26	0.11
Opal-A	-0.27	-0.29	0.02	0.24	0.08	0.21	-0.67	-0.85	1.00	0.64	-0.22	-0.18
Calcite	-0.24	-0.22	0.15	0.19	-0.06	0.02	-0.41	-0.56	0.64	1.00	-0.12	-0.03
Halite	-0.19	0.27	0.10	-0.13	-0.33	-0.15	0.41	0.26	-0.22	-0.12	1.00	-0.34
Illite	0.03	0.04	-0.26	0.01	0.32	-0.15	-0.21	0.11	-0.18	-0.03	-0.34	1.00

Table 4.6: Ordered correlation coefficients between mineral contents and depth of exploration well 35/11-5.

4.5. WELL DATA

This study uses lithology information based on cutting descriptions, bottom-hole temperatures and core porosities of the Norwegian Petroleum Directorate (NPD, 2014). Furthermore, wireline data of sixteen exploration wells including gamma ray, neutron porosity, bulk density and p-wave velocity logs, are used (Tab. 4.7).

Wells	Depth range [m]	Wireline data	Others
35/8-2	26-4356	AIMP, CALI, DT, GR, NPHI, RHOB, VELC, VSH	BHT
35/11-6	27-3997	CALI, DRHO, DT, DTS, GR, NPHI, RD, RHOB, RM, RMIC, VELC	BHT
35/11-2	23-4035	AIMP, CALI, DT, GR, NPHI, RD, RHOB, RM, RMIC, SP, VELC, VSH	BHT
35/10-1	23-3860	AIMP, CALI, DT, GR, NPHI, RHOB, SP, VELC	BHT, XRD
35/11-5	27-3768	AIMP, CALI, DRHO, DT, GR, NPHI, RD, RHOB, RM, RMIC, SP, VELC, VSH	BHT, XRD
31/2-8	361-3386	AC, CALI, DEN, GR, NEU, RDEP, RMED, RMIC	BHT
31/2-9	350-1769	AC, CALI, DEN, GR, NEU, RDEP, RMED, RMIC	BHT
31/2-14	349-1730	AC, CALI, DEN, GR, NEU, RDEP, RMED, RMIC	BHT
31/2-7	353-1668	AC, CALI, DEN, GR, NEU, RDEP, RMED, RMIC	BHT
31/2-4	0-5037	CALI, DRHO, DT, GR, NPHI, RD, RHOB, RM, RSH	BHT, HEL_POR
31/2-12	446-1620	AC, CALI, DEN, GR, NEU, RDEP, RMED, RMIC	BHT
31/2-11	355-1740	AC, CALI, DEN, GR, NEU, RDEP, RMED, RMIC	BHT
31/2-10	343-1839	AC, CALI, DEN, GR, NEU, RDEP, RMED, RMIC	BHT
31/2-13 S	347-2013	AC, CALI, DEN, DT, GR, NEU, RDEP, RHOB, RMED	BHT
31/2-5	348-2530	AC, CALI, DEN, GR, NEU, RDEP, RMED, RMIC	BHT, HEL_POR
31/5-3	351-2254	AC, CALI, DEN, GR, NEU, RDEP, RMED, RMIC, SP	BHT

Table 4.7: Well table (AC-Average sonic travel time, AIMP-acoustic Impedance, BHT-bottom hole temperature, CALI-calliper, DEN-bulk density, DRHO-density correction, DT-interval transit time, DTS-shear wave slowness, GR-gamma ray, HEL_POR-helium porosity, NEU/ NPHI-neutron porosity, RD/RDEP-deep resistivity, RHOB-bulk density, RM/RMED-medium resistivity, RMIC/RSH-micro resistivity, SP-spontaneous Potential, VELC-compressional velocity, VSH-shale volume, and XRD-X-ray diffraction data).

The wireline log quality was checked using caliper and density correction logs according to Rider and Kennedy (2011).

4.5.1. Petrophysics

To constrain the influence of silica diagenesis on compaction, porosity logs were derived from wireline data for all sixteen exploration wells. First, clay volumes were calculated from the neutron porosity and bulk density logs using a standard method described by Rider and Kennedy (2011). Three end-member points (i.e. clay point, fluid point and matrix point) were defined based on a neutron porosity/bulk density cross-plot. Based on the distance to these end-member points, the clay

volume of each data point was calculated. As the definition of these end-member points is crucial to the precision of the method, lithology information from well reports (NPD, 2014) were used in addition to the data cloud to define the end-member points for each well. The clay point had typically values around 0.6 (neutron porosity) and 2.2. g/cm^3 (bulk density). The pore fluid was assumed to be pore water (i.e. neutron porosity and bulk density to be 1) and the rock matrix to consist of clays (i.e. neutron porosity of 0 and bulk density of 2.2 g/cm^3). Based on these parameters, the clay volume was calculated for each data point as the relative distance between end-member points:

$$V_{clay} = \frac{(\rho_F - \rho_M) \cdot (n - n_M) - (\rho - \rho_M) \cdot (n_F - n_M)}{(\rho_F - \rho_M) \cdot (n_C - n_M) - (\rho_C - \rho_M) \cdot (n_F - n_M)} \quad (4.11)$$

V_{clay} – Clay volume

ρ – Bulk density of data points

ρ_C – Bulk density of clay point (*c.* 2.2 g/cm^3)

ρ_F – Bulk density of fluid point (1 g/cm^3)

ρ_M – Bulk density of matrix point (*c.* 2.2 g/cm^3)

n – Neutron porosity of data points

n_C – Neutron porosity of clay point (0.6)

n_F – Neutron porosity of fluid point (1)

n_M – Neutron porosity of matrix point (0)

Based on the clay volumes, five porosity logs were calculated from bulk density, neutron porosity and sonic logs, and combinations of the neutron porosity/bulk density and neutron porosity/sonic logs. The accuracy of these five porosity logs was assessed by comparing them to core porosities in exploration wells 31/2-5 (Fig. 4.11).

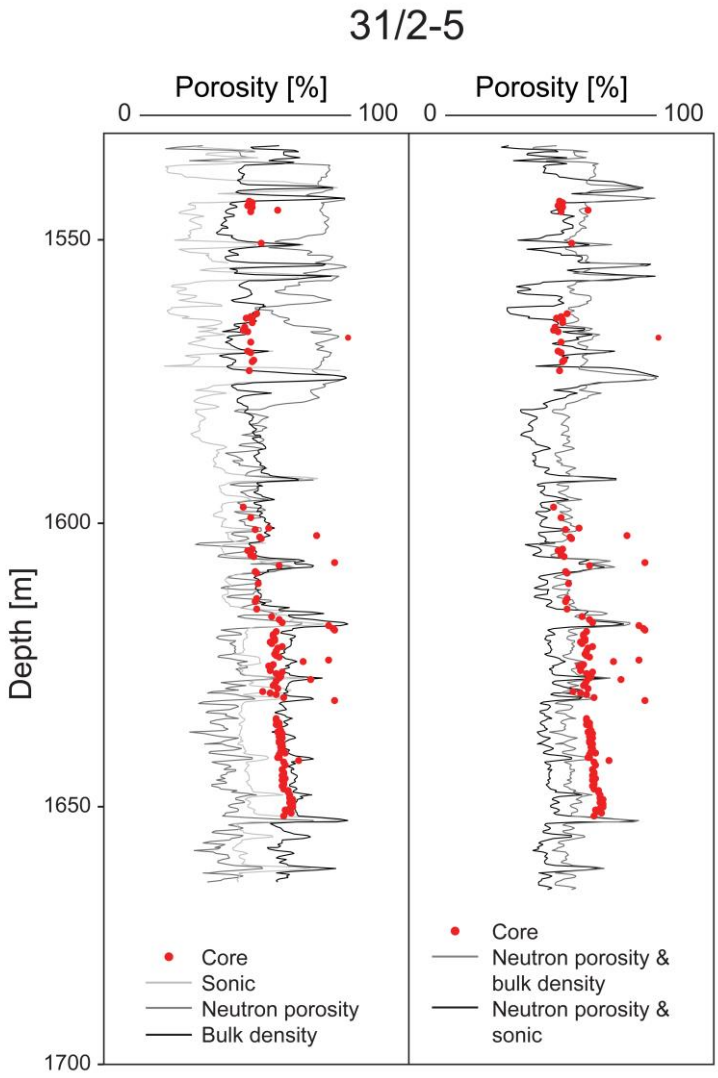


Figure 4.11: Comparison of porosity logs derived from sonic, neutron porosity, bulk density, neutron porosity & bulk density as well as neutron porosity & sonic to core porosities.

This comparison shows that porosity logs derived from bulk density provide the most accurate estimate (average difference <10 %) and therefore have been used in all subsequent analyses. These porosity logs were calculated from clay volume and bulk density:

$$\phi = \frac{\rho_M - \rho - V_{clay} \cdot (\rho_M - \rho_C)}{\rho_M - \rho_F} \tag{4.12}$$

ϕ – (Effective) porosity

ρ_M – Matrix density (2.2 g/cm^3)

ρ – Input bulk density log

V_{clay} – Clay volume (calculated earlier)

ρ_C – Wet clay density (2.3 g/cm^3)

ρ_F – Filtrate density (1 g/cm^3)

4.5.2.Descriptive statistics

This section contains a statistical description of the wireline data used in this study. While Figures 4.12 and 4.13 show data of exploration well 35/10-1 and 35/11-5, Tables 4.8 and 4.9 contain the corresponding statistics calculated using Equations 4.2-4.10 in R (2014).

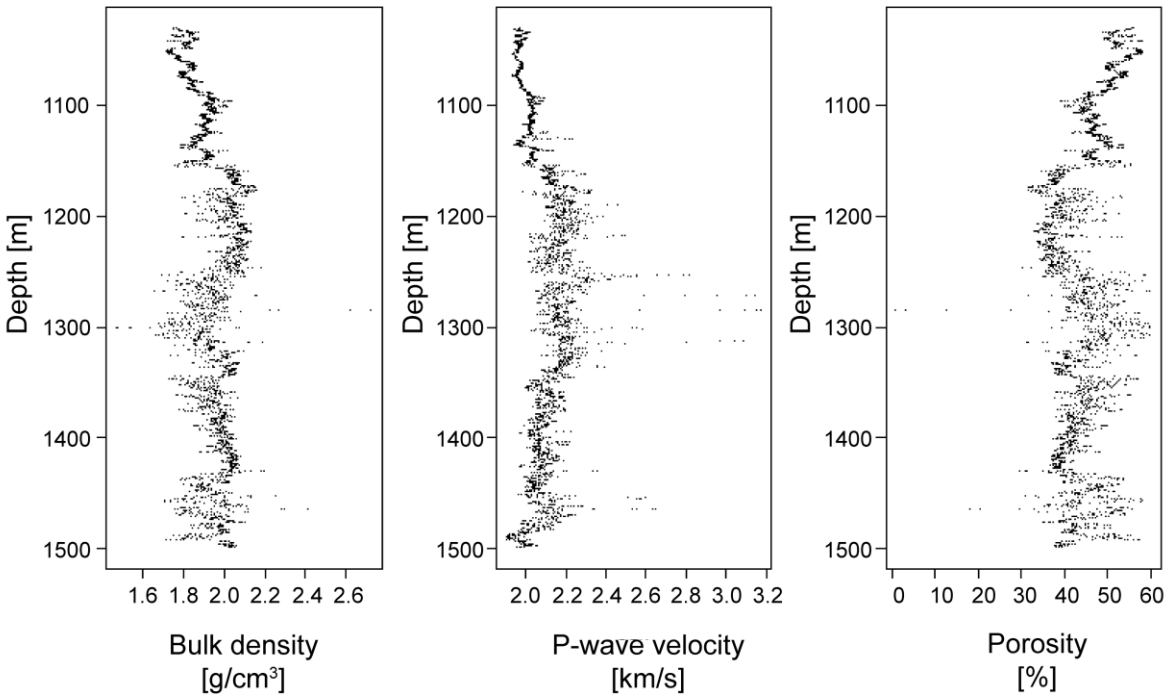


Fig. 4.12: Bulk density, p-wave velocity and porosity logs of well 35/11-5.

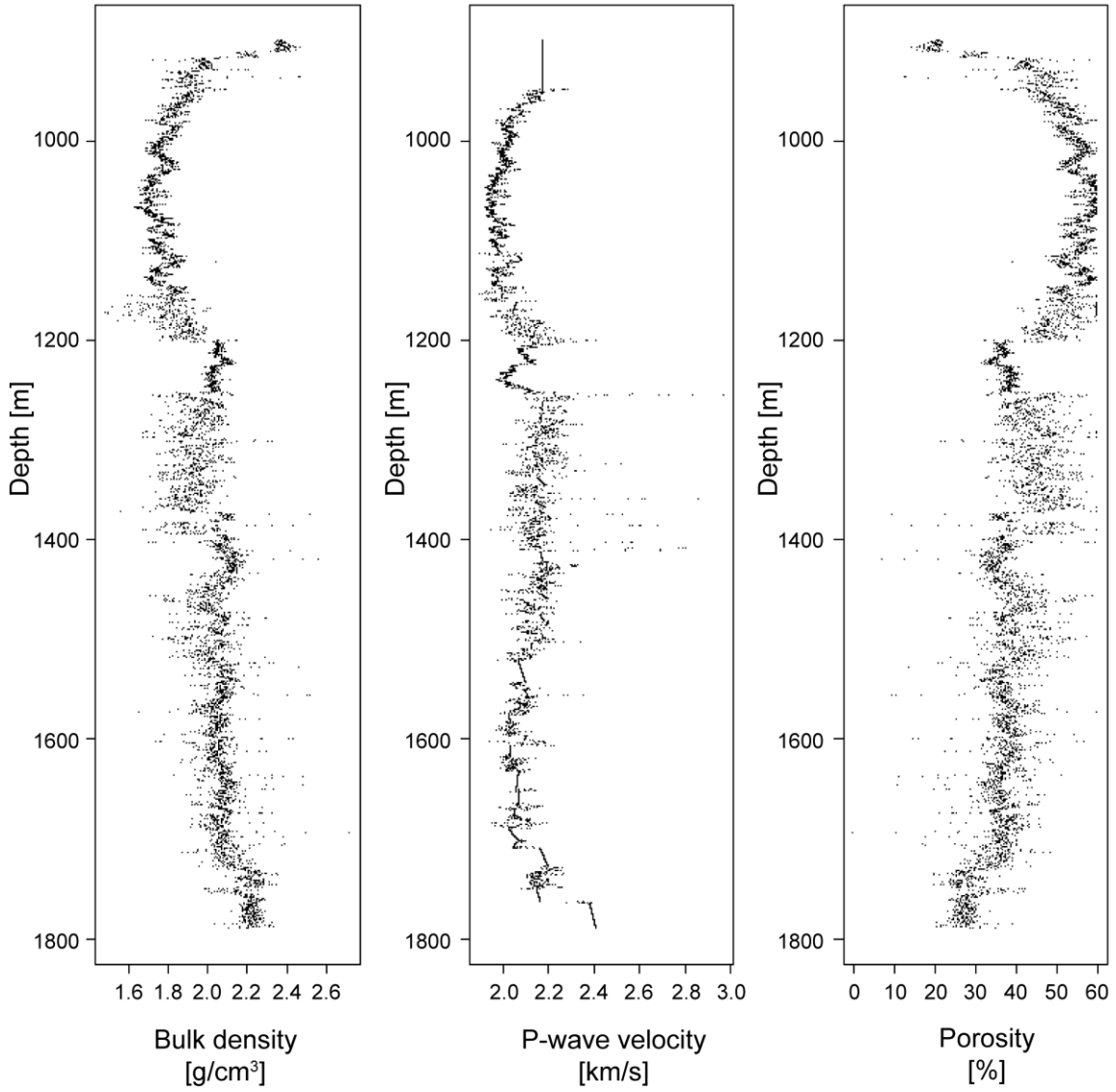


Fig. 4.13: Bulk density, p-wave velocity and porosity logs of well 35/10-1.

	n	min	max	range	mean	var	sd	skew	kurtosis	se
DEN	5840	1.48	2.72	1.24	1.98	0.03	0.16	0.07	-0.32	0
SON	5840	1.9	2.97	1.07	2.11	0.01	0.1	1.38	5.08	0
POR	5840	0.01	60	59.99	42.79	94.67	9.73	-0.08	-0.49	0.13

Table 4.8: Statistics of wireline data of exploration well 35/10-1 with n – number of samples, min – minimum, max – maximum, range – range, mean – arithmetic mean, var – variance, sd – standard deviation, skew – skewness, kurtosis – kurtosis and se – standard error.

	n	min	max	range	mean	var	sd	skew	kurtosis	se
Bulk density	3084	1.47	2.73	1.26	1.94	0.01	0.1	0	1.53	0
P-wave velocity	3084	1.9	3.18	1.27	2.11	0.01	0.12	2.54	15.54	0
Porosity	3084	1.04	60	58.96	44.78	36.48	6.04	-0.1	1.17	0.11

Table 4.9: Statistics of wireline data of exploration well 35/11-5 with n – number of samples, min – minimum, max – maximum, range – range, mean – arithmetic mean, var – variance, sd – standard deviation, skew – skewness, kurtosis – kurtosis and se – standard error.

4.6. DATA INTEGRATION

To investigate the influence of silica diagenesis on the host rock properties, quantitative mineralogical and wireline data are integrated. For the integration, the two data types need to have the same scale. While mineralogical data is based on cuttings samples which were recovered in 10 intervals, wireline data is available every 0.125 m. To match the scales, wireline data is averaged over 10 m intervals. Moreover, two outliers (at 1250 and 1780 m depth) with anomalously-high quartz contents (>40 vol.%) are removed from exploration well 35/10-1. The analysed data is provided in the appendix (Tabs. 8.1, 8.2).

4.6.1.Correlation

The correlation between composition and rock properties is assessed using crossplots and correlation coefficients (Tabs. 4.10, 4.11) (Figs. 4.14, 4.15).

	Illite-Smectite	Illite	Kaolinite	Opal-A	Opal-CT	Quartz	Calcite	Pyrite	Barite	Sylvite	Halite
Bulk density	0.74	-0.46	-0.39	-0.83	-0.01	0.14	-0.29	0.61	-0.10	-0.56	-0.16
P-wave velocity	0.27	-0.08	0.00	-0.51	0.35	0.08	-0.08	0.22	0.01	-0.18	-0.08
Porosity	-0.74	0.46	0.40	0.83	0.02	-0.15	0.28	-0.62	0.11	0.57	0.16

Table 4.10: Correlation coefficients between mineral contents and wireline data in exploration well 35/10-1.

	Illite-Smectite	Illite	Kaolinite	Opal-A	Opal-CT	Quartz	Calcite	Pyrite	Barite	Sylvite	Halite
Bulk density	0.23	0.12	0.05	-0.49	0.34	0.00	-0.38	0.00	-0.09	-0.14	-0.13
P-wave velocity	0.14	0.13	0.26	-0.59	0.46	0.14	-0.47	0.14	0.13	-0.17	-0.04
Porosity	-0.23	-0.12	-0.05	0.49	-0.33	0.00	0.38	0.00	0.09	0.14	0.13

Table 4.11: Correlation coefficients between mineral contents and wireline data in exploration well 35/11-5.

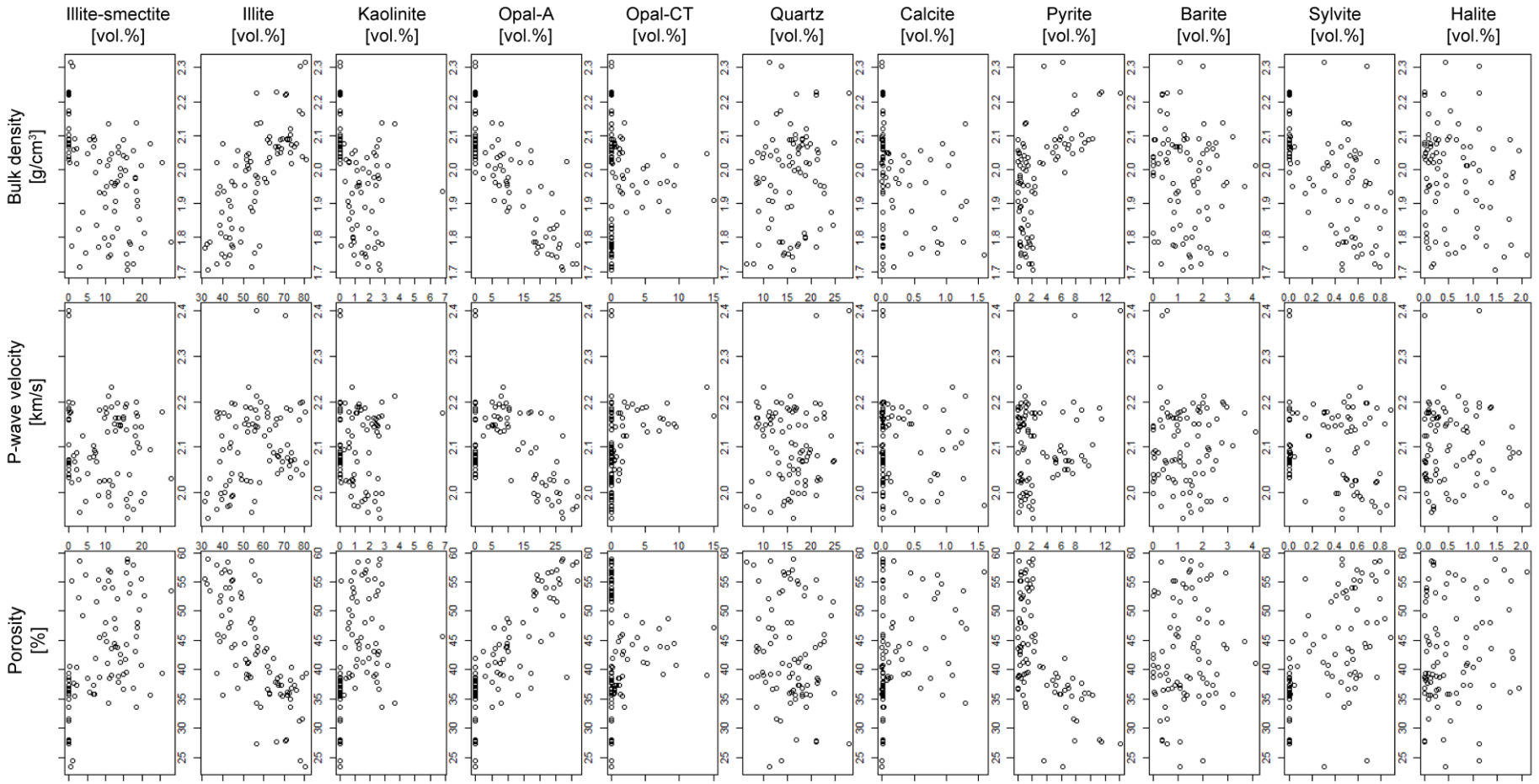


Fig. 4.14: Crossplots of mineral contents versus wireline data of well 35-10-1.

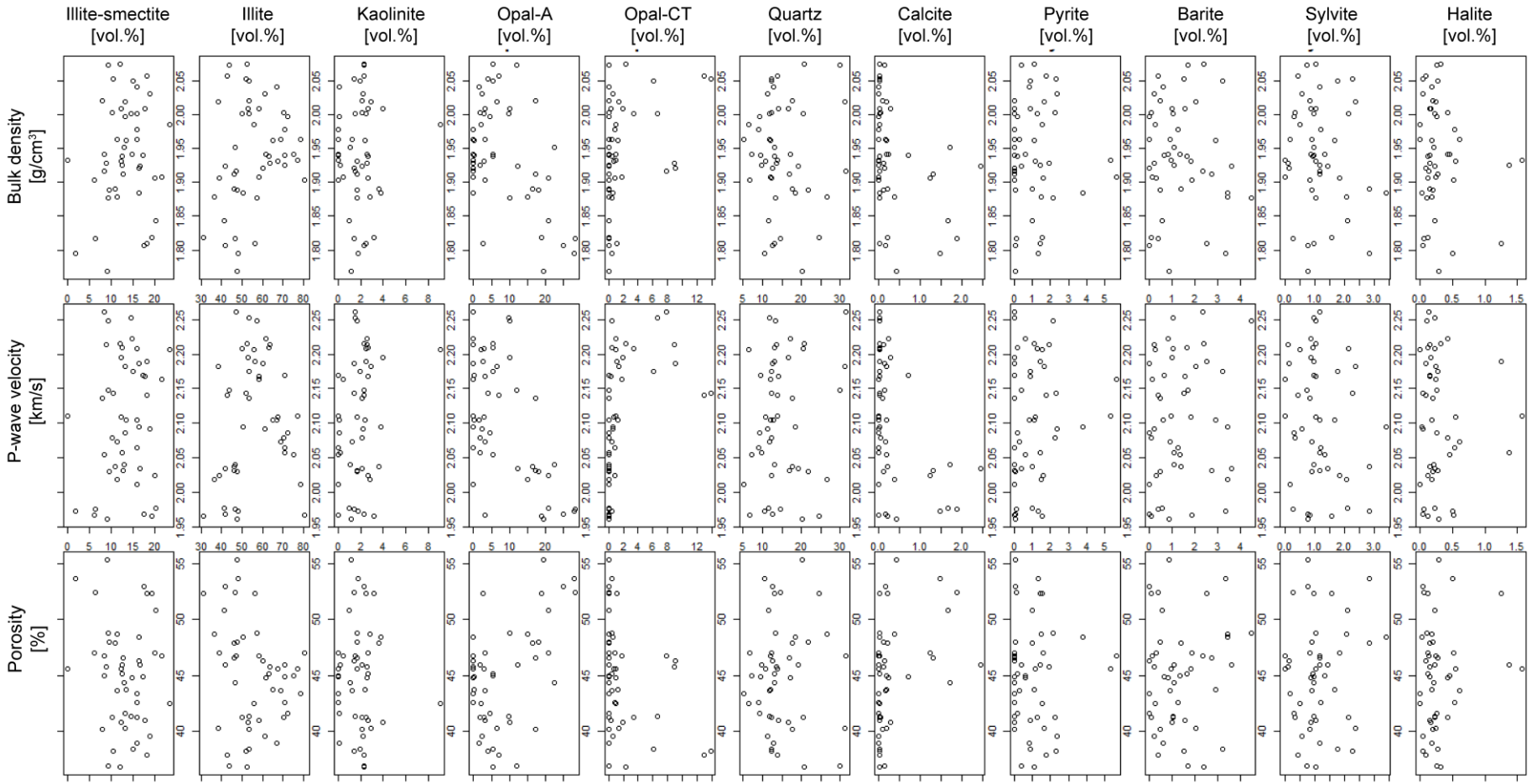


Fig. 4.15: Crossplots of mineral contents versus wireline data of well 35-11-5.

4.6.2. Multiple linear regression analysis

Multiple regression analysis is applied to examine the influence of composition (in particular opal-A, opal-CT and quartz contents) on the physical host rock properties (in particular porosity) while accounting for depth. Multiple linear regression is concerned with the relationship of a set of variables **X** to another variable **y**:

$$\begin{pmatrix} y_1 \\ y_2 \\ \vdots \\ y_n \end{pmatrix} = \begin{pmatrix} 1 & x_{11} & \cdots & x_{k1} \\ 1 & x_{12} & \cdots & x_{k2} \\ 1 & \vdots & \ddots & \vdots \\ 1 & x_{1n} & \cdots & x_{kn} \end{pmatrix} \cdot \begin{pmatrix} \beta_1 \\ \beta_2 \\ \vdots \\ \beta_k \end{pmatrix} + \begin{pmatrix} u_1 \\ u_2 \\ \vdots \\ u_n \end{pmatrix} \tag{4.13}$$

$$\mathbf{y} = \mathbf{X\beta} + \mathbf{u} \tag{4.14}$$

where **y** is the dependent variable; **X** are the independent variables; **β** are the regression coefficients and **u** is the error term (Everitt & Skrondal, 2002). The most common estimator for multiple linear regression is 'ordinary least squares' which minimises the sum of the squared residuals:

$$\widehat{\boldsymbol{\beta}} = \left(\mathbf{X}^{\mathbf{T}}\mathbf{X}\right)^{-\mathbf{1}}\mathbf{X}^{\mathbf{T}}\mathbf{y} \tag{4.15}$$

with $\widehat{\boldsymbol{\beta}}$ referring to the estimated regression coefficients and

$$\widehat{\mathbf{u}} = \mathbf{y} - \mathbf{X}\widehat{\boldsymbol{\beta}} \tag{4.16}$$

being the estimated error term (residual).

To select the appropriate independent variables, all subsets regression is applied. All subsets regression runs all possible models and ranks them based on a predefined criterion. This study uses the Bayesian information criterion or BIC (Schwarz, 1978) which accounts for model fit and the number of variables in the model:

$$\mathrm{BIC} = -2\ln(\hat{\mathrm{L}}) + \mathrm{m} \cdot \ln(\mathrm{n}) \tag{4.17}$$

with $\hat{\mathrm{L}}$ the maximised value of the likelihood function, m the number of free variables and n the number of observations. The BIC is chosen because it penalises the inclusion of additional independent variables in line with the parsimony principle. The ten 'best' models with the lowest BIC are listed in Tabs. 4.12 and 4.13, respectively.

Model	Intercept	Depth	Illite-Smectite	Illite	Kaolinite	Opal-A	Opal-CT	Quartz	Calcite	Pyrite	Barite	Sylvite	Halite	R^2	adR^2	BIC
1	1	0	0	0	0	1	0	0	0	1	0	0	0	0.71	0.71	-95.47
2	1	0	0	0	0	1	1	0	0	0	0	0	0	0.71	0.70	-94.79
3	1	0	0	0	0	1	0	0	0	0	0	0	0	0.70	0.69	-94.42
4	1	1	0	0	0	1	0	0	0	1	0	0	0	0.72	0.71	-93.96
5	1	0	0	0	1	1	0	0	0	0	0	0	0	0.71	0.70	-93.78
6	1	0	0	0	0	1	1	0	0	1	0	0	0	0.72	0.71	-92.46
7	1	0	0	0	0	1	0	0	0	1	0	0	1	0.72	0.71	-92.17
8	1	0	1	0	0	1	0	0	0	0	0	0	0	0.70	0.70	-92.16
9	1	0	0	0	0	1	1	0	0	0	0	0	1	0.72	0.71	-92.13
10	1	0	0	0	1	1	1	0	0	0	0	0	0	0.72	0.71	-92.13
Sum	10	1	1	0	1	10	4	0	0	4	0	0	2	-	-	-

Table 4.12: Ten models with the lowest BIC selected by all subsets regression with data of well 35/10-1.

Model	Intercept	Depth	Illite-Smectite	Illite	Kaolinite	Opal-A	Opal-CT	Quartz	Calcite	Pyrite	Barite	Sylvite	Halite	R^2	adR^2	BIC
1	1	0	0	0	0	1	0	0	0	0	0	0	1	0.30	0.27	-5.68
2	1	0	0	0	0	1	0	0	0	0	0	0	0	0.24	0.23	-5.60
3	1	0	0	0	0	1	1	0	0	0	0	0	0	0.29	0.25	-4.51
4	1	0	0	0	0	1	1	0	0	0	0	0	1	0.32	0.28	-3.31
5	1	0	0	0	0	1	0	0	0	1	0	0	0	0.27	0.23	-3.24
6	1	0	1	0	0	1	0	0	0	0	0	0	0	0.26	0.23	-2.79
7	1	0	0	0	0	1	0	0	0	1	0	0	1	0.31	0.27	-2.52
8	1	0	0	0	0	1	0	1	0	0	0	0	0	0.25	0.22	-2.40
9	1	1	0	0	0	1	0	0	0	0	0	0	0	0.25	0.22	-2.40
10	1	0	0	0	0	1	1	0	0	1	0	0	0	0.31	0.26	-2.35
Sum	10	1	1	0	0	10	3	1	0	3	0	0	3	-	-	-

Table 4.13: Ten models with the lowest BIC selected by all subsets regression with data of well 35/11-5.

To analyse the ten selected models, a series of properties characterising the regression coefficients and the model are calculated. To characterise the model, the coefficient of determination, adjusted coefficient of determination and Bayes information criterion are calculated. To calculate these, the total (TSS), explained (ESS) and residual sum of squares (RSS) are determined:

$$\mathrm{TSS} = \sum_{i=1}^{n} (y_i - \bar{y})^2 \tag{4.17}$$

$$\mathrm{ESS} = \sum_{i=1}^{n} (\hat{y}_i - \bar{y})^2 \tag{4.18}$$

$$\mathrm{RSS} = \sum_{i=1}^{n} (y_i - \hat{y}_i)^2 \tag{4.19}$$

with $\bar{y}$ the arithmetic mean of the dependent variable and $\hat{y}$ the estimated dependent variable. Next, the coefficient of determination (R^2) and the adjusted coefficient of determination ($\mathrm{adj}R^2$) are calculated:

$$R^2 = 1 - \frac{\mathrm{RSS}}{\mathrm{TSS}} \tag{4.20}$$

$$\mathrm{adj}R^2 = 1 - \frac{(1 - R^2)(n - 1)}{n - p - 1} \tag{4.21}$$

with n the number of observations and p the number of predictor variables (Everitt & Skrondal, 2002). The Bayes information criterion is calculated according to Eq. 4.17 (Schwarz, 1978). Furthermore, the absolute and relative regression coefficients are calculated according to Eq. 4.15 using the standardized and unstandardised independent variables, respectively (see Appendix 8.3). To characterise the (unstandardized) regression coefficients, their standard error, t-statistic, p-value and variance inflation index are calculated (Everitt & Skrondal, 2002). The standard error (SE) is:

$$\mathrm{SE}(\hat{\beta}_i)^2 = \hat{\sigma}^2 (X^T X)^{-1} \tag{4.22}$$

with $\hat{\sigma}$ the mean square error. The t-statistic (t) is:

$$t_{\hat{\beta}_i} = \frac{\hat{\beta}_i - 0}{\mathrm{SE}(\hat{\beta}_i)} \tag{4.22}$$

The p-value (p) is the probability of obtaining similar results as observed assuming the null hypothesis (H_0) is true:

$$p = Pr(\hat{\beta}_i|H_0) \tag{4.23}$$

$$H_0: \beta_i = 0 \tag{4.24}$$

The variance inflation factor (VIF) is:

$$VIF = \frac{1}{1 - R^2} \tag{4.25}$$

Model	Predictors	Coefficients		Coefficient statistics				Model statistics		
		absolute	relative	SE	t-statistic	p-value	VIF	R^2	adjR^2	BIC
1	Intercept	37.58	-3.08e-16	1.24	30.22	< 2e-16 ***	-	0.71	0.71	-95.47
	Opal-A	0.63	0.73	0.06	9.79	1.57e-15 ***	1.62			
	Pyrite	-0.46	-0.17	0.19	-2.35	0.0214 *	1.62			
2	Intercept	34.48	-2.69e-16	0.81	42.40	< 2e-16 ***	-	0.71	0.70	-94.79
	Opal-A	0.74	0.85	0.05	14.40	< 2e-16 ***	1.02			
	Opal-CT	0.37	0.13	0.17	2.19	0.0313 *	1.02			
3	Intercept	35.23	-2.74e-16	0.75	46.66	< 2e-16 ***	-	0.70	0.69	-94.42
	Opal-A	0.72	0.83	0.05	13.92	< 2e-16 ***	-			
4	Intercept	28.31	-2.89e-16	5.61	5.05	2.62e-06 ***	-	0.72	0.71	-93.96
	Depth	6.39e-03	0.18	3.78e-03	1.69	0.09 .	3.65			
	Opal-A	0.74	0.85	0.09	8.21	2.54e-12 ***	3.21			
	Pyrite	-0.59	-0.22	0.21	-2.83	5.82e-03 **	1.88			
5	Intercept	34.58	-2.86e-16	0.81	42.50	< 2e-16 ***	-	0.71	0.70	-93.78
	Opal-A	0.69	0.79	0.05	12.56	< 2e-16 ***	1.14			
	Kaolinite	0.90	0.12	0.47	1.94	0.06 .	1.14			
6	Intercept	36.43	-2.96e-16	1.58	23.09	< 2e-16 ***	-	0.72	0.71	-92.46
	Opal-A	0.67	0.76	0.07	9.35	1.31e-14 ***	1.99			
	Opal-CT	0.23	0.08	0.19	1.18	0.241	1.36			
	Pyrite	-0.32	-0.12	0.22	-1.44	0.155	2.17			
7	Intercept	36.91	-3.12e-16	1.34	26.51	< 2e-16 ***	-	0.72	0.71	-92.17
	Opal-A	0.63	0.73	0.06	9.81	1.6e-15 ***	1.62			
	Pyrite	-0.42	-0.16	0.20	-2.16	0.0334 *	1.65			
	Halite	0.97	0.06	0.91	1.06	0.29	1.03			
8	Intercept	42.13	-2.83e-16	4.76	8.84	1.23e-13 ***	-	0.70	0.70	-92.16
	Illite-Smectite	-0.10	-0.16	0.07	-1.15	0.146	3.25			
	Opal-A	0.61	0.70	0.09	6.55	4.33e-09 ***	3.25			
9	Intercept	33.87	-2.77e-16	0.93	36.35	< 2e-16 ***	-	0.72	0.71	-92.13
	Opal-A	0.73	0.84	0.05	16.25	< 2e-16 ***	1.03			
	Opal-CT	0.36	0.13	0.17	2.15	0.03 *	1.02			
	Halite	1.19	0.08	0.90	1.32	0.19	1.01			
10	Intercept	34.18	-2.77e-16	0.84	40.59	< 2e-16 ***	-	0.72	0.71	-92.13
	Kaolinite	0.64	0.08	0.49	1.32	0.191	1.28			
	Opal-A	0.71	0.82	0.06	12.70	< 2e-16 ***	1.21			
	Opal-CT	0.29	0.10	0.18	1.65	0.102	1.14			

Table 4.14: Properties of models selected by all subsets regression using data of well 35/10-1. See above text for description.

Model	Predictors	Coefficients		Coefficient statistics				Model statistics		
		absolute	relative	SE	t-statistic	p-value	VIF	R^2	adjR^2	BIC
1	Intercept	41.39	6.24e-16	1.04	39.78	< 2e-16 ***	-	0.30	0.27	-5.68
	Opal-A	0.30	0.55	0.07	4.29	9.22e-05 ***	1.05			
	Halite	3.59	0.25	1.83	2.00	0.06 .	1.05			
2	Intercept	42.71	6.10e-16	0.82	52.04	< 2e-16 ***	-	0.24	0.23	-5.60
	Opal-A	0.27	0.49	0.07	3.84	3.76ee-04 ***	-			
3	Intercept	43.50	6.15e-16	0.94	46.29	< 2e-16 ***	-	0.29	0.25	-4.51
	Opal-A	0.24	0.43	0.07	3.32	1.82e-03 **	1.08			
	Opal-CT	-0.29	-0.21	0.18	-1.64	0.11	1.08			
4	Intercept	42.20	6.25e-16	1.24	34.07	< 2e-16 ***	-	0.32	0.28	-3.31
	Opal-A	0.27	0.50	0.07	3.69	6.23e-04 ***	1.18			
	Opal-CT	-0.22	-0.16	0.18	-1.18	0.24	1.16			
	Halite	2.99	0.21	1.89	1.59	0.12	1.13			
5	Intercept	41.89	6.05e-16	1.08	38.89	< 2e-16 ***	-	0.27	0.23	-3.24
	Opal-A	0.29	0.54	0.07	4.04	2.06e-04 ***	1.09			
	Pyrite	0.59	0.16	0.49	1.20	0.24	1.09			
6	Intercept	38.56	5.66e-16	4.22	9.14	7.97e-12 ***	-	0.26	0.23	-2.79
	Illite-Smectite	0.07	0.17	0.06	1.00	0.32	1.81			
	Opal-A	0.33	0.61	0.09	3.53	9.87e-04 ***	1.81			
7	Intercept	40.95	6.19e-16	1.18	34.68	< 2e-16 ***	-	0.31	0.27	-2.52
	Opal-A	0.31	0.57	0.07	4.35	8.05e-05 ***	1.12			
	Pyrite	0.40	0.11	0.49	0.81	0.42	1.15			
	Halite	3.25	0.23	1.88	1.73	0.09 .	1.11			
8	Intercept	43.80	6.13e-16	1.60	27.44	< 2e-16 ***	-	0.25	0.22	-2.40
	Opal-A	0.28	0.51	0.07	3.91	3.12e-04 ***	1.04			
	Quartz	-0.08	-0.11	0.10	-0.80	0.43	1.04			
9	Intercept	33.81	5.66e-16	11.21	3.02	4.19e-03 ***	-	0.25	0.22	-2.40
	Depth	6.45e-03	0.19	8.10e-03	0.80	0.43	3.61			
	Opal-A	0.36	0.66	0.13	2.69	0.01 *	3.61			
10	Intercept	42.65	6.09e-16	1.15	37.00	< 2e-16 ***	-	0.31	0.26	-2.35
	Opal-A	0.26	0.48	0.07	3.56	9.19e-04 ***	1.17			
	Opal-CT	-0.30	-0.22	0.18	-1.68	0.10	1.08			
	Pyrite	0.61	0.16	0.48	1.26	0.21	1.09			

Table 4.15: Properties of models selected by all subsets regression using data of well 35/11-5. See above text for description.

Multiple regression is based on five assumptions: (1) low degree of multicollinearity, (2) linearity, (3) homoscedasticity, (4) independence of error, and (6) normality of errors (e.g. Hair *et al.*, 2006). The degree of multicollinearity is assessed using the variance inflation factor (Tabs. 4.14, 4.15). The linearity between dependent and independent variables is examined with residual (Figs. 4.16, 4.17) and partial residual plots (Figs. 4.18, 4.19). These plots show the residuals of the regression with the dependent and independent variables, respectively. Homoscedasticity which is the constancy of errors is also assessed using residual plots. Independence of errors is assessed using partial residual plots (Figs. 4.18, 4.19) and normality of errors is assessed using normal probability plots (Figs. 4.20, 4.21) which show the data with a normal distribution as a linear function. Note that the analysis is performed using R (2014) (see Appendix 8.3).

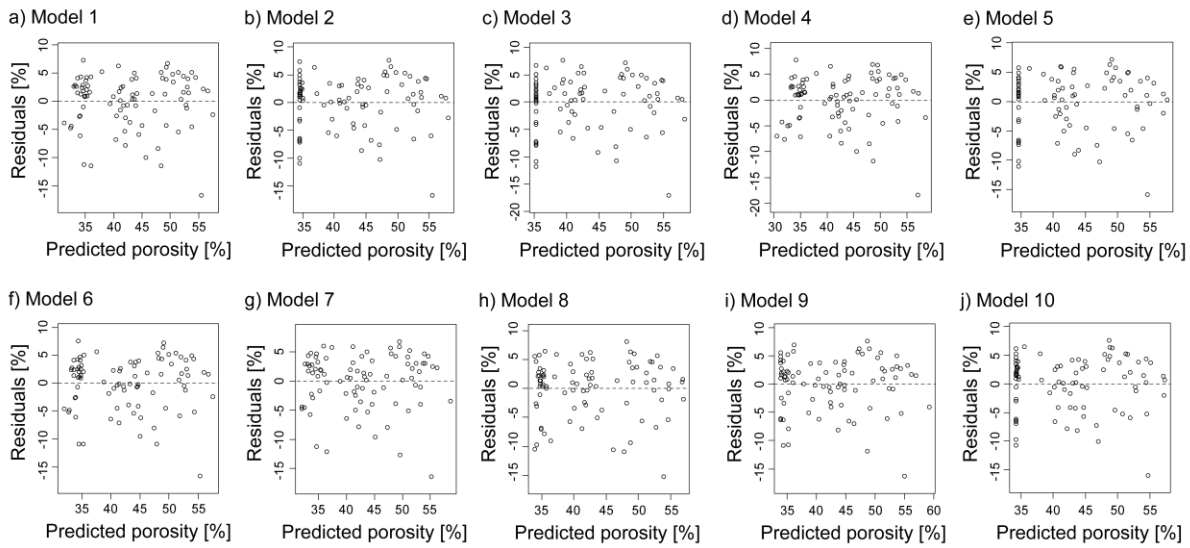


Figure 4.16: Residual plots of models selected by all subsets regression using data of well 35/10-1

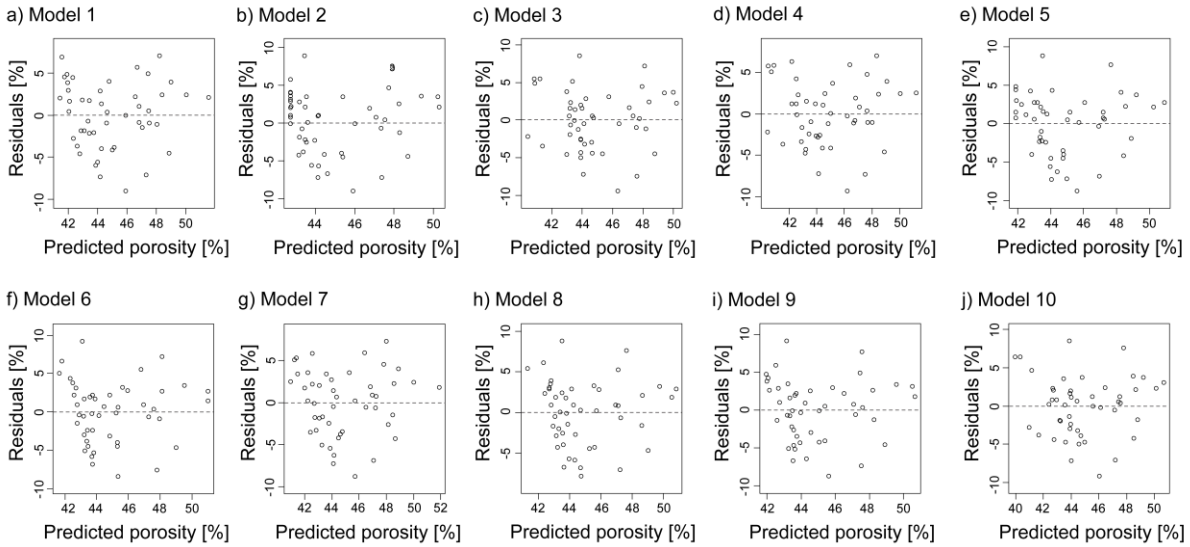


Figure 4.17: Residual plots of models selected by all subsets regression using data of well 35/11-5.

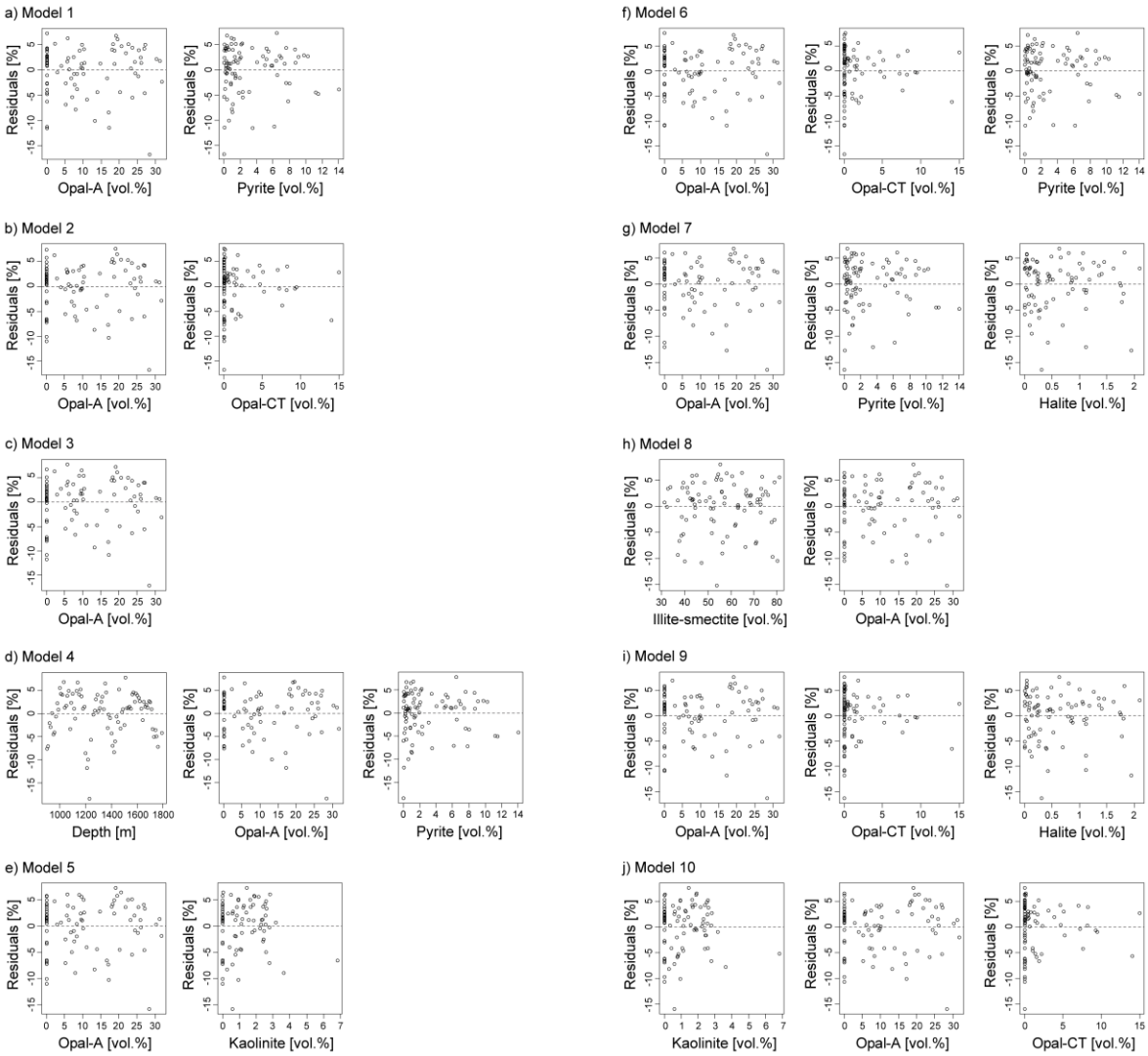


Figure 4.18: Partial residual plots of models selected by all subsets regression using data of well 35/10-1.

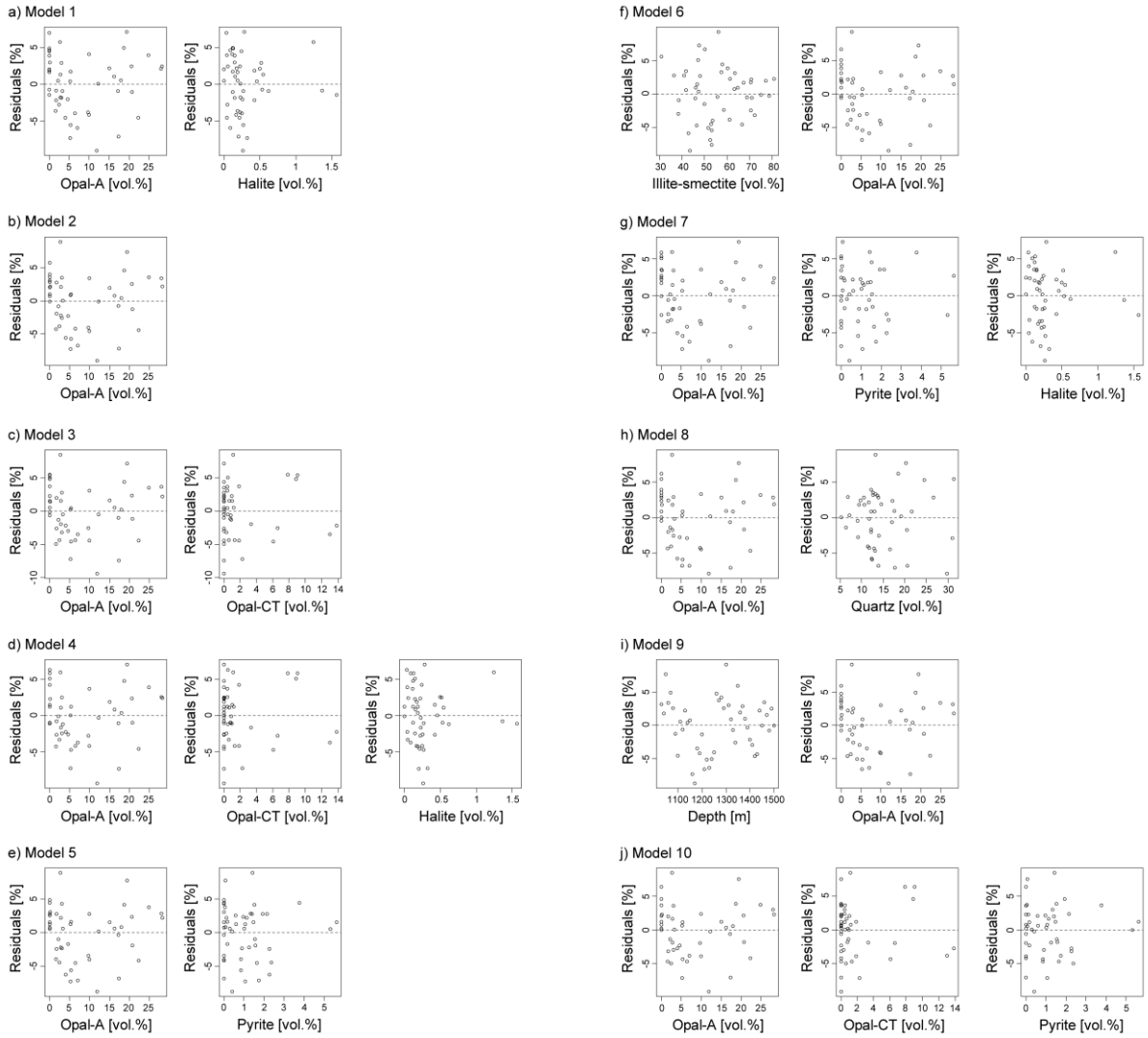


Figure 4.19: Partial residual plots of models selected by all subsets regression using data of well 35/11-5.

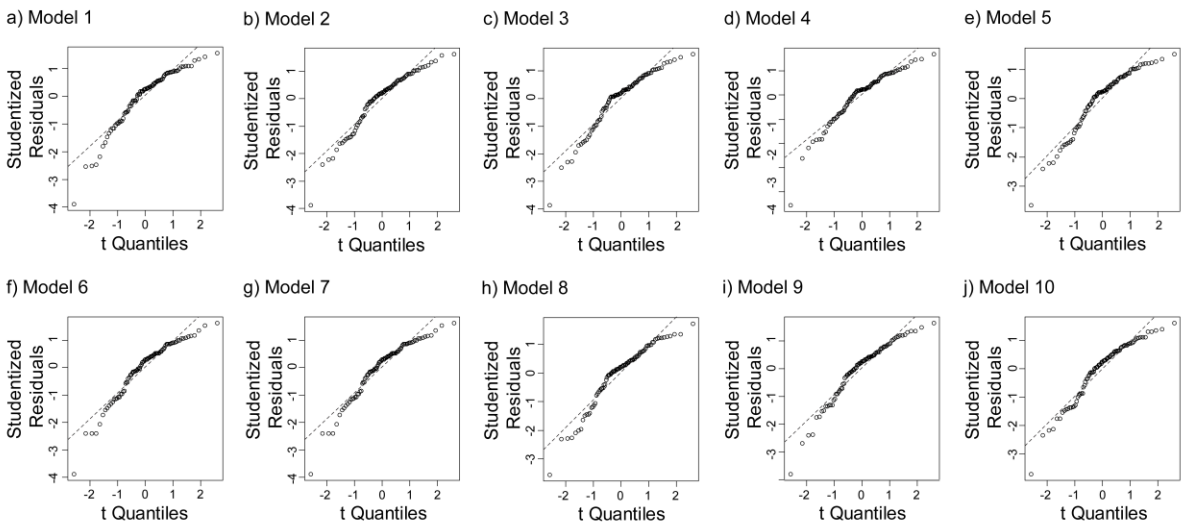


Figure 4.20: Normal probability plots of models selected by all subsets regression using data of well 35/10-1.

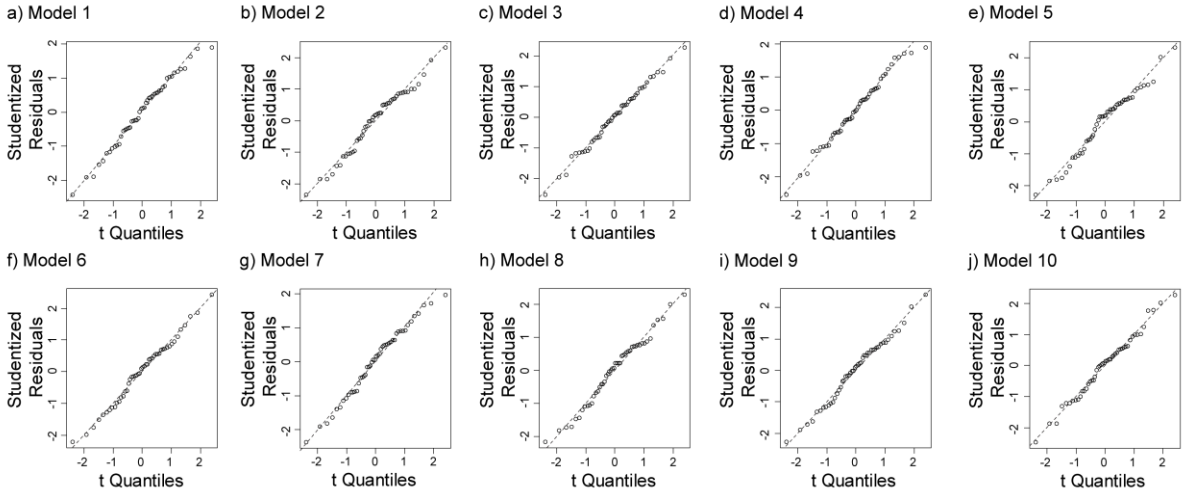


Figure 4.21: Normal probability plots of models selected by all subsets regression using data of well 35/11-5.

4.7. SEISMIC DATA

4.7.1. 3-D seismic reflection data

Five three-dimensional seismic reflection volumes that cover part of the eastern margin of the North Viking Graben (Fig. 3.1) are used in this study. Three of these volumes (MN9201_R05, WESTERN3510, STNH98N) have a line spacing of 25 m and a vertical sampling of 4 ms, and two (NH0301, BPN9301) have a line spacing of 12.5 m and 2 ms vertical sampling. All surveys are time-migrated and zero-phase processed with SEG reverse polarity; i.e. an acoustic impedance increase with depth is represented by a negative reflection event (blue or black), and a decrease in acoustic impedance with depth is represented by a positive reflection event (red or white). The p-wave velocity logs and check shots indicate that the average seismic velocity within and above the interval of interest is 2000±200 m/s, thus allowing vertical measurements made in milliseconds two-way time (ms TWT) to be directly converted to depth (m), as a first order approximation. In conjunction with the determined interval velocity, the dominant frequency for all the seismic datasets is *c.* 50 Hz, suggesting that, in the interval of interest, the seismic data have a vertical resolution of *c.* 10 m and a horizontal resolution of *c.* 20 m.

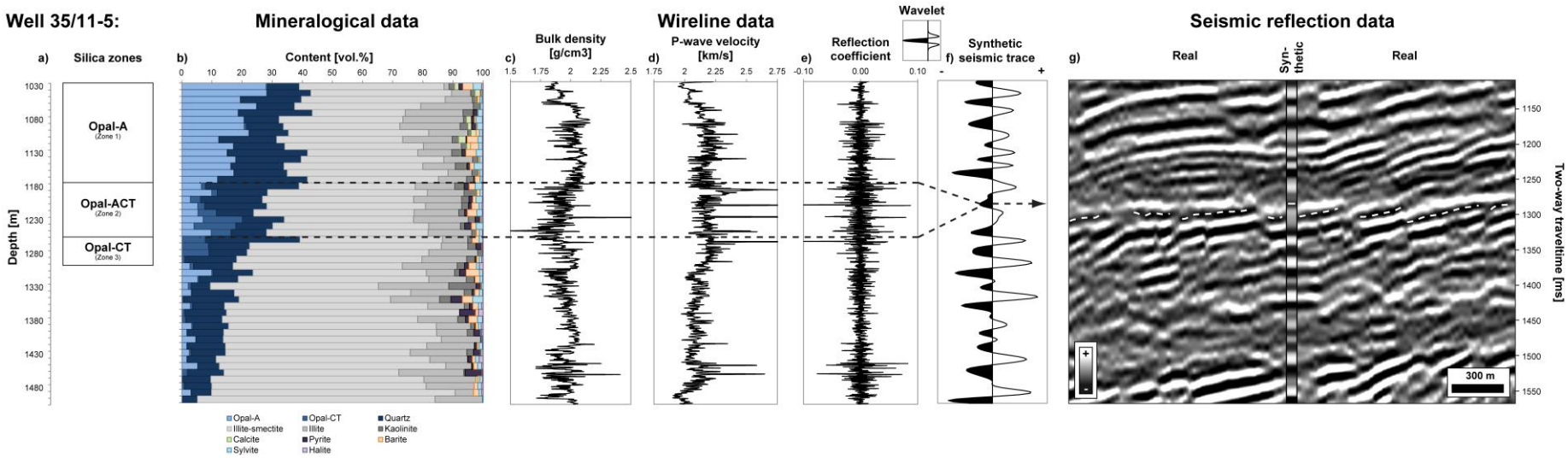


Figure 4.22: Seismic to well tie for exploration well 35/11-5 showing: a) the silica zones, b) mineralogical data, c) bulk density, d) p-wave velocity, e) reflection coefficient, f) extracted wavelet and synthetic seismic trace and g) real seismic trace.

4.7.2. Seismic-to-well tie

To ensure an accurate tie between well data (depth domain) and seismic data (time domain), synthetic seismograms were calculated for each well (e.g. Fig. 4.22). Deterministic, zero-phase wavelets were extracted using the extended Roy White method (Walden & White, 1998). The synthetic seismograms were calculated by convolution of the wavelet, extracted from the seismic traces surrounding the well path, with the reflectivity log, that was derived from the bulk density and p-wave velocity logs (e.g. Fig. 4.22). Establishing an accurate tie between well and seismic data for all wells allowed key stratigraphic boundaries (e.g. mid-Miocene unconformity and Eocene/Oligocene boundary), and the potential opal-A/CT transformation zone (Zone 2), to be identified and mapped in seismic data.

4.7.3. Seismic interpretation

The seismic interpretation involved mapping the seismic reflections associated with the three main stratigraphic boundaries (i.e. Top Eocene, Top Oligocene, mid-Miocene Unconformity), beginning at the well locations. By mapping these reflections away from the well locations and between seismic volumes, it was possible to produce a series of regional maps of these key stratigraphic boundaries. Having established the main stratigraphic framework, the same methodology was applied to interpret the seismic reflection associated with the opal-A/CT transformation (Figs. 4.23-4.25). This reflection required careful mapping, as 'diagenetic' reflections are often slightly discordant with stratigraphic reflections (see Hammond & Gaither, 1983; Berndt *et al.*, 2004; Ireland *et al.*, 2011). A TWT-thickness map, which allow an investigation of spatial variations in thickness of the opal-A zone (Zone 1) was also inferred (Fig. 4.26).

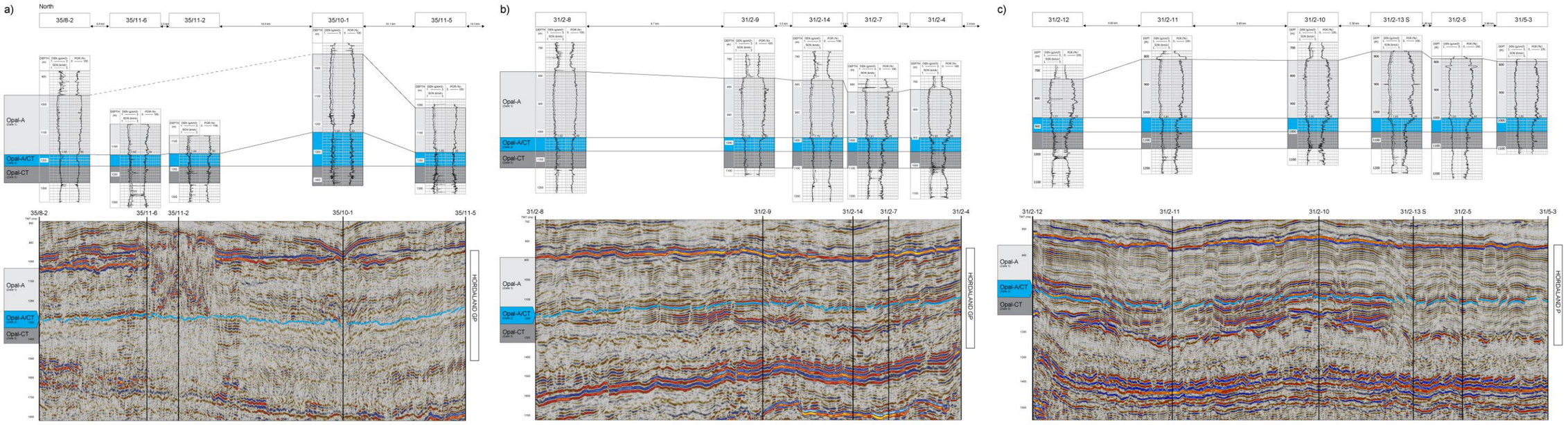


Figure 4.23: Well- and seismic section (N-S) through exploration wells a) 35/8-2, 35/11-6, 35/11-2, 35/10-1, 35/11-5, b) 31/2-8, 31/2-9, 31/2-14, 31/2-7, 31/2-4, and c) 31/2-12, 31/2-11, 31/2-10, 31/2-13 S, 31/2-5, 31/5-3 showing the bulk density logs (left), p-wave velocity (left, dotted) and effective porosity logs (right) , the silica zones (Zones 1-3). Note changes of the wireline logs and seismic reflections across the opal-A/CT transformation zone (Zone 2).

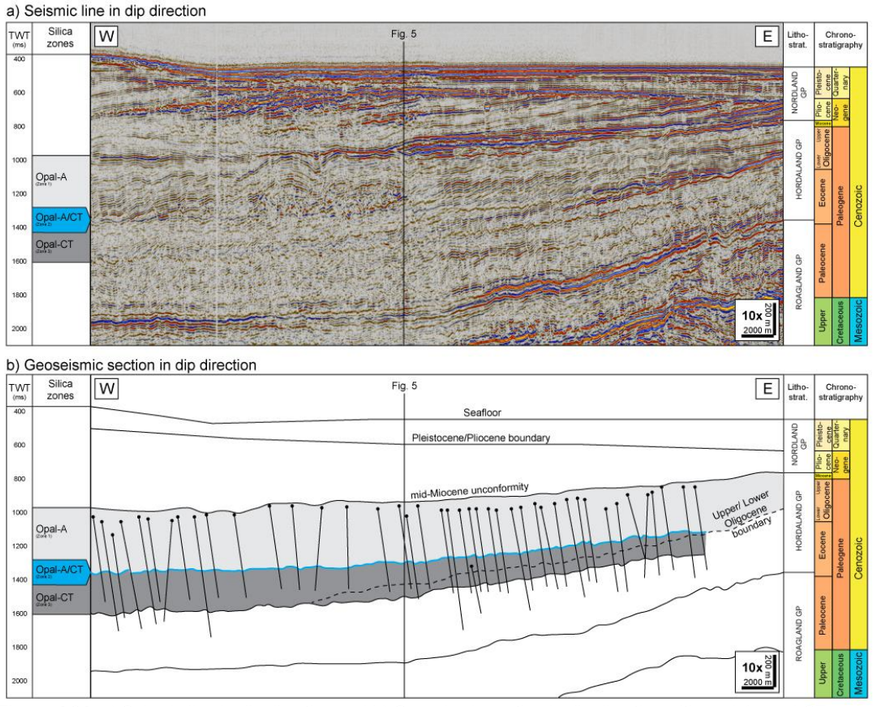


Figure 4.24: a) Seismic line in dip direction and b) Geoseismic section in dip direction with opal-A, opal-CT and quartz zones as well as opal-A/CT and opal-CT/Q transformation zones, litho- and chronostratigraphy and polygonal fault system (PFS). Note the westward-dipping, sometimes discordant reflections associated with the opal-A/CT and opal-CT/Q transformation zone.

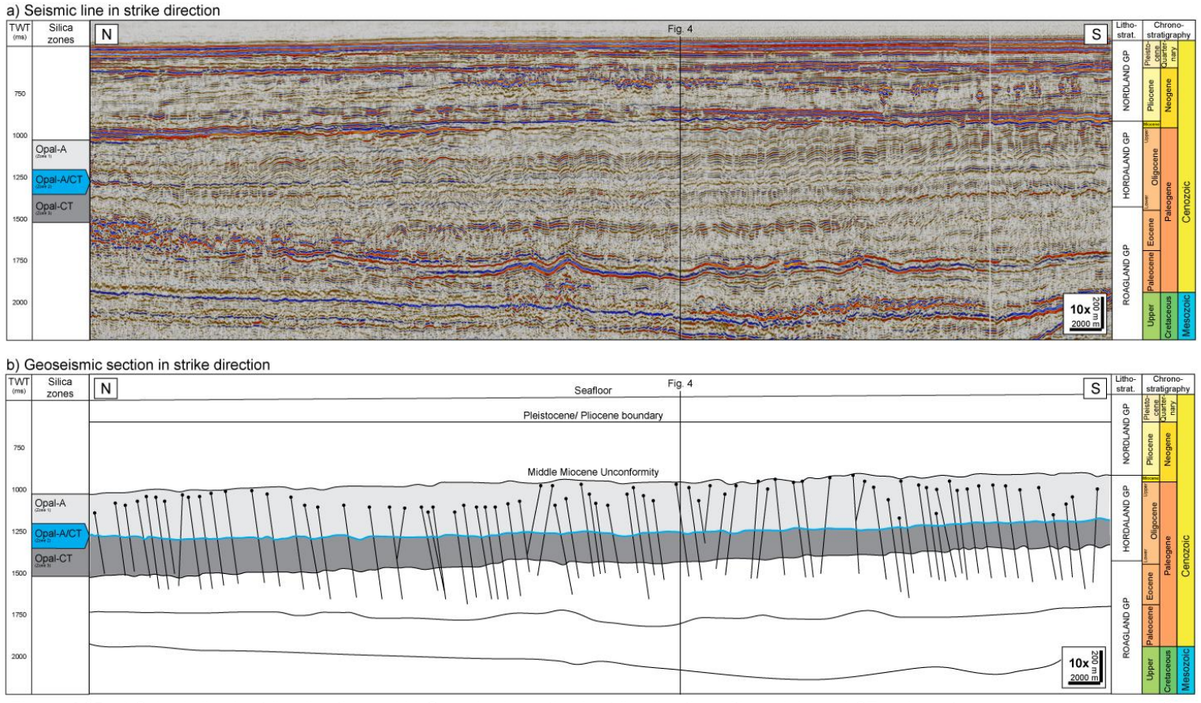


Figure 4.25: a) Seismic line in strike direction and b) Geoseismic section in strike direction with opal-A, opal-CT and quartz zones as well as opal-A/CT and opal-CT/Q transformation zones, litho- and chronostratigraphy and the polygonal fault system (PFS). Note the sometimes discordant reflections associated with the opal-A/CT and opal-CT/Q transformation zone.

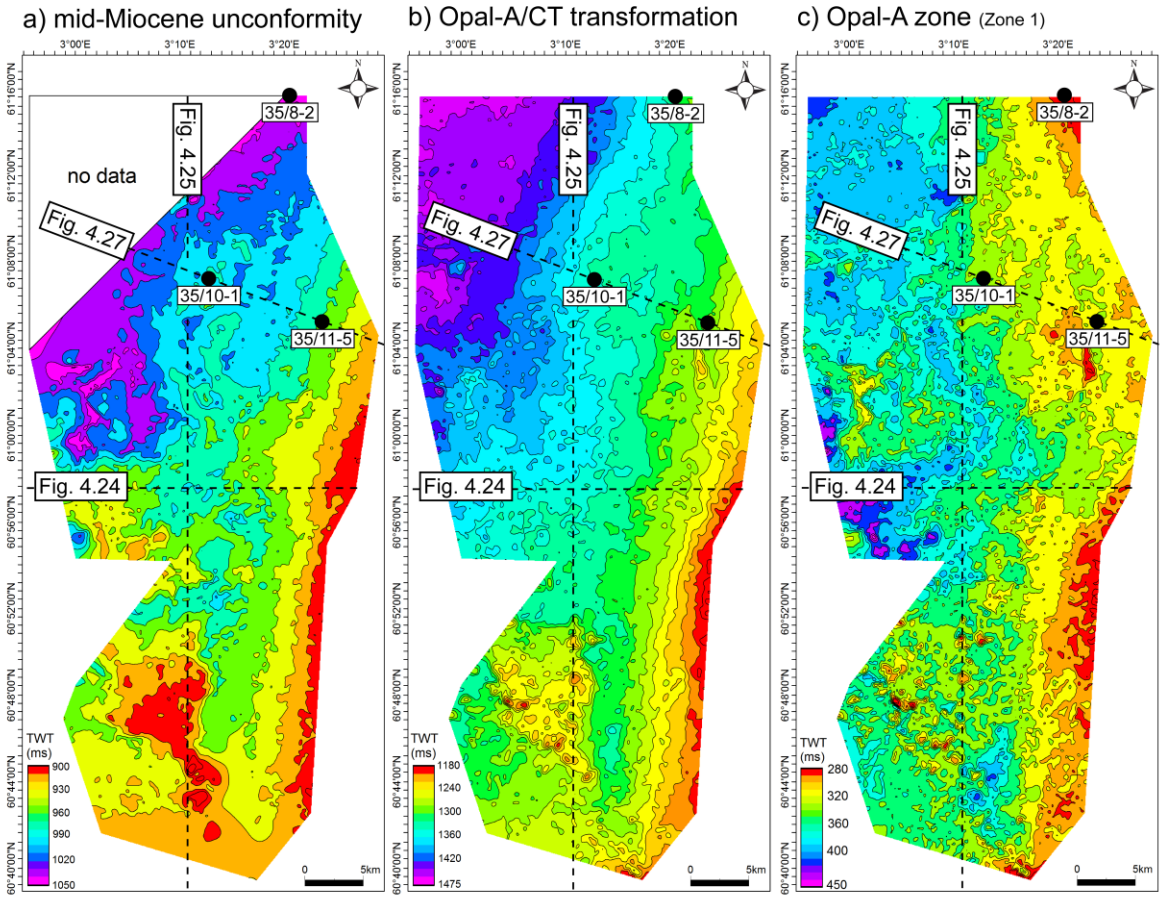


Figure 4.26: Time structure map of: a) the mid-Miocene unconformity, i.e. Top of Zone 1, b) opal-A/CT transformation zone, i.e. Zone 2 and c) Isochron map of the opal-A zone (Zone 1). Note the similarities between the time structure maps of the mid-Miocene unconformity (a) and the opal-A/CT transformation zone (b).

4.8. BASIN MODELLING

Subsurface temperatures calculated during basin modelling allow the simulation of silica diagenesis in space and time. To produce reliable simulation results, boundary conditions are constrained as accurately as possible. Basin modelling is performed with PetroMod 2013 and involves four steps: 1) input, 2) definition of boundary conditions, 3) simulation and 4) calibration. Input data, such as basin geometry, stratigraphy and lithology, are specific to area and stratigraphic interval of interest. To define the basin geometry, an east-west trending seismic section passing through exploration wells 35/10-1 and 35/11-5 is depth-converted (Fig. 4.27). The underlying velocity model is based on well tops of each lithostratigraphic group, and linear velocity-depth functions that are

derived from checkshot data for each of these groups. Chronostratigraphic and lithological units are based on the NPD (2014).

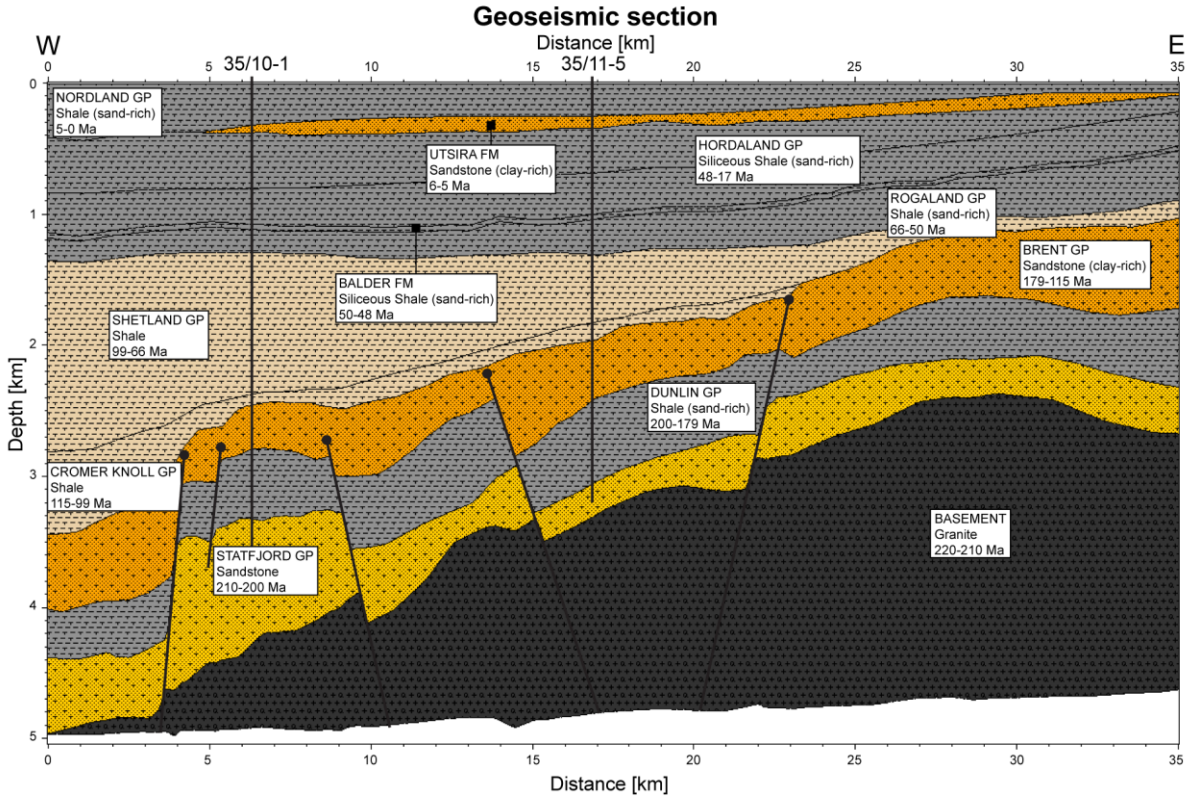


Figure 4.27: Geoseismic section (through exploration wells 35/10-1 and 35/11-5) used to define the geometry, stratigraphy and lithology of all basin models.

The second step comprises the definition of boundary conditions: 1) palaeo water depth, 2) palaeo seafloor temperature and 3) heat flow history (Fig. 4.28). Palaeo water depths were taken from Kyrkjebø *et al.* (2001) and palaeo seafloor temperatures were constrained by oxygen isotope ratios of Jensen and Buchardt (1987) and Anderson *et al.* (1994). The heat flow history was based on a reconstruction by Lucazeau and Le Douaran (1984). This heat flow history reflects initial Triassic and secondary Late Jurassic rift episodes, as well as the far-field effect of the opening of the North Atlantic during the Palaeogene.

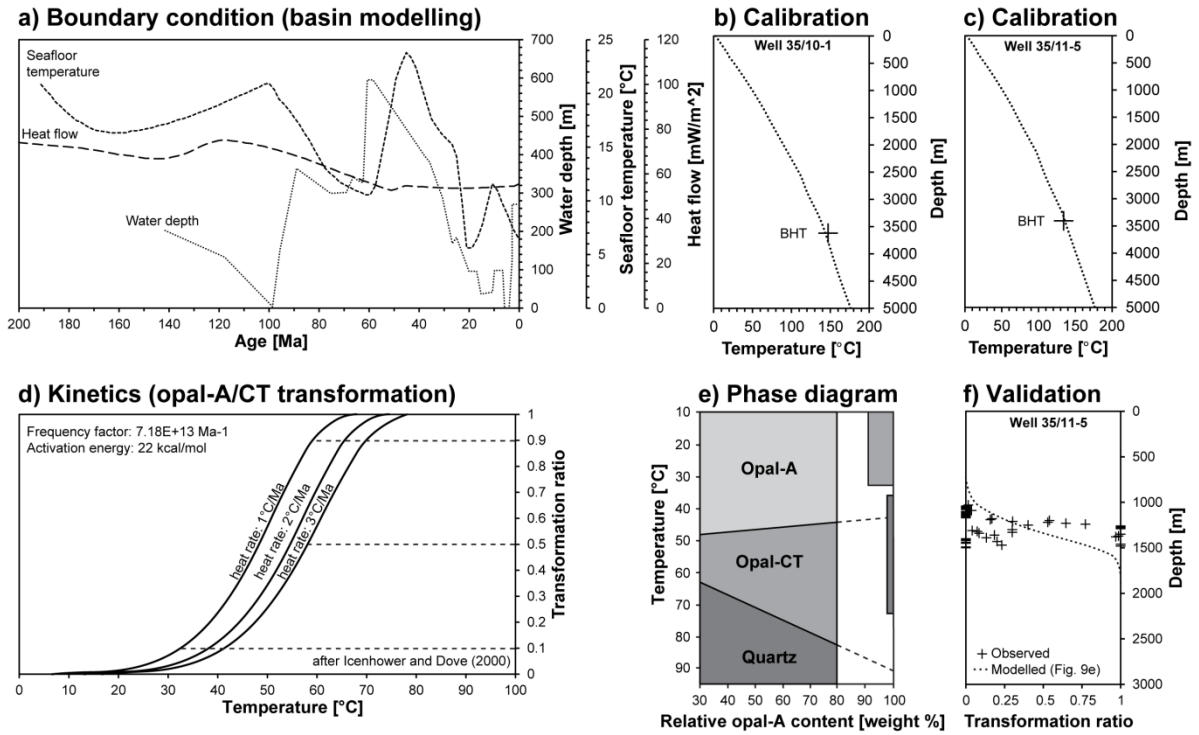


Figure 4.28: a) Boundary conditions used for basin modelling including seafloor temperature (from Jensen & Buchardt, 1987; Anderson *et al.*, 1994), heat flow (after Lucazeau & Le Douaran, 1984) and water depth (from Kyrkjebø *et al.*, 2001). b) Calibration of basin model using bottom hole temperature of exploration well 35/10-1. c) Calibration of basin model using bottom hole temperature of exploration well 35/11-5. d) Kinetic data from Icenhower and Dove (2000) used to model the opal-A/CT transformation. e) Phase diagram for silica diagenesis (from Keller & Isaacs, 1985; Behl, 2011). f) Comparison of transformation ratio observed in exploration well 35/11-5 (see Fig. 3) and predicted by kinetic data from Icenhower and Dove (2000).

The third step comprises the simulation of: 1) deposition and erosion 2) pressure and compaction and 3) temperature. Deposition is simulated by adding layers at the upper surface of the model. Initial layer thickness (d_0) is reconstructed from the current thickness (d_0), current (ϕ_1) and depositional porosities (ϕ_0):

$$d_0(1-\phi_0) = d_1(1-\phi_1) \tag{4.26}$$

which are in turn inferred by decompaction. Erosion is simulated by removing layers at the upper surface. Middle Miocene erosion in the North Viking Graben is, for instance, simulated as the removal of a 70 m sediment column, as suggested by measurements of erosional escarpments by Løseth *et al.* (2013) between 6-17 Ma, as suggested by a detailed biostratigraphic analysis of Eidvin and Rundberg (2001). Pressure is calculated from the overburden weight due to sedimentation and compaction is computed from pore pressure reductions. The temperature calculation is based on heat conduction, convection as well as heat generation from radioactive decay. For the theoretical

background and implementation of these processes, the reader is referred to Hantschel and Kauerauf (2009) and the PetroMod 2013 user manual.

The final step of the basin modelling was the calibration. The model was calibrated by matching the modelled and measured present day temperatures at the bottom-hole of exploration wells 35/10-1 and 35/11-5 (Fig. 4.28b,c). Assuming they have been allowed to re-equilibrate, bottom-hole temperatures are well-constrained and are therefore suitable to calibrate basin models (Hantschel & Kauerauf, 2009). For the calibration, the heat flow of Lucazeau and Le Douaran (1984) was increased by a constant 13 mW/m^2, which reflects the fact that Lucazeau and Le Douaran (1984) derive surface heat flow, whereas our basin model requires heat flow to be added at its base, simulating heat addition from the asthenosphere into the lithosphere. Our study also differs from Lucazeau and Le Douaran (1984) in that we use a more realistic range of thermal conductivities for the crustal lithologies (1.8 $Wm^{-1}K^{-1}$ for shale, 3.2 $Wm^{-1}K^{-1}$ for sandstone and 2.4 $Wm^{-1}K^{-1}$ for granite) instead of a single value (3 $Wm^{-1}K^{-1}$).

4.8.1. Modelling of the opal-A/CT transformation

The opal-A/CT transformation involves a series of chemical reactions that are controlled by multiple factors. In this scenario, the slowest of these reactions typically controls the overall transformation rate. In case of the opal-A/CT transformation, it has been demonstrated that opal-A dissolution is the slowest reaction controlling the overall transformation rate (Williams *et al.*, 1985; Hinman, 1998). It is therefore assumed that the opal-A dissolution kinetics can be utilised to model the opal-A/CT transformation. The dissolution rate of opal-A has been demonstrated to be primarily time-temperature dependent (e.g. Kastner *et al.*, 1977; Keller & Isaacs, 1985; Williams *et al.*, 1985; Dove & Rimstidt, 1994). As a first order approximation, the opal-A/CT transformation is therefore modelled as a time-temperature dependent reaction. The validity of this approach is critically discussed in chapter 6.

To model the opal-A/CT transformation dependent on time and temperature, the transformation rate is described by Arrhenius' law (1889):

$$k = A \cdot \exp\left(-\frac{E}{RT}\right) \tag{4.27}$$

k – Transformation rate

A – Activation energy

E – Frequency factor

R – Gas constant (8.314 J K^{-1} mol^{-1})

T – Temperature

The key parameters in this equation are the frequency factor, which is the frequency at which molecules react, and the activation energy, the threshold energy to initiate the reaction. For opal-A dissolution, these parameters (A=22 kcal/mol and E=7.18·1013 Ma^{-1}) were experimentally derived and summarised by Icenhower and Dove (2000). Because opal-A dissolution seems to control opal-A/CT transformation (see above), these parameters were used to model the transformation. These parameters seem to produce realistic results comparing the predicted transformation temperatures to the temperature scale of the opal-A/CT transformation (Fig. 4.28d,e). This approach is furthermore validated by the match between the modelled and observed opal-A/CT transformation ratios in exploration well 35/11-5 (Fig. 4.28f).

4.9. FAULT ANALYSIS

4.9.1.Seismic interpretation

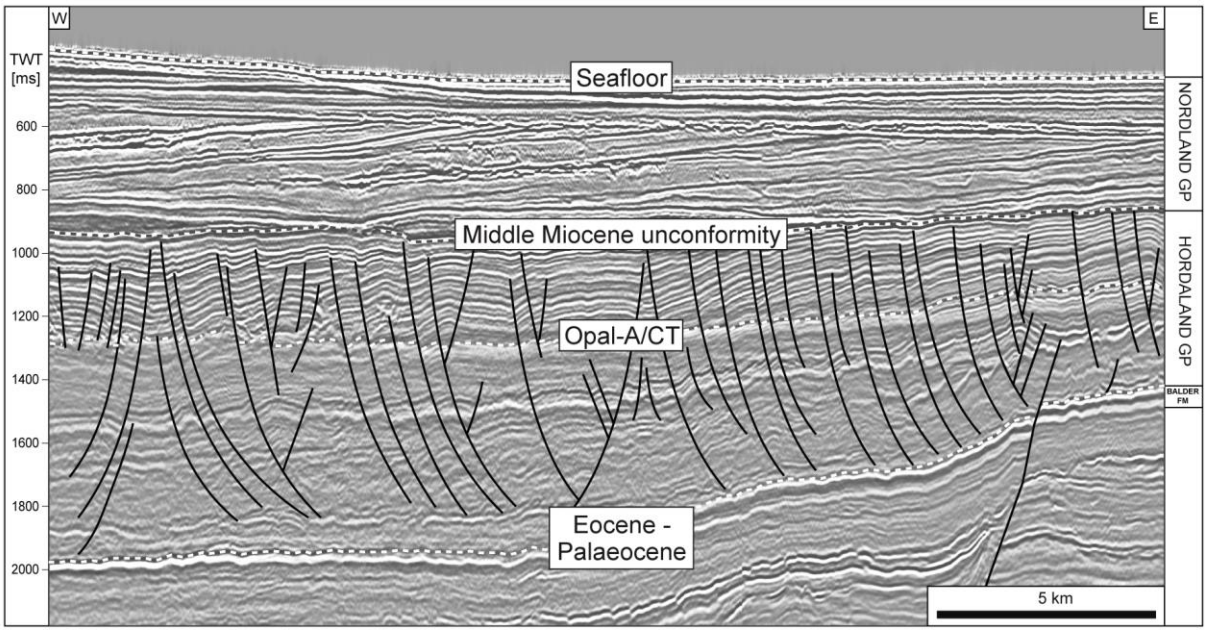


Figure 4.29: Seismic section showing polygonal fault system bound between the top of the Balder Formation and the middle Miocene unconformity.

The key seismic reflections defining the top and base of the Hordaland Group, that bound the polygonal fault system and correspond to the Middle Miocene unconformity and the top of the Balder Formation, are mapped over an area of approximately 740 km^2 (Figs. 4.29, 4.30). A prominent seismic reflection produced by the opal-A/CT transformation was also mapped in the Hordaland Group. The variance/coherency attribute (see Bahorich & Farmer, 1995) was calculated along the opal-A/CT reflection to image the polygonal fault system (Fig. 4.30). As this fault system consists of more than 2500 faults, a representative 6.25 x 6.25 km sub-cube of the original seismic volume was selected in which a detailed, quantitative analysis of 137 faults was conducted (Fig. 4.30).

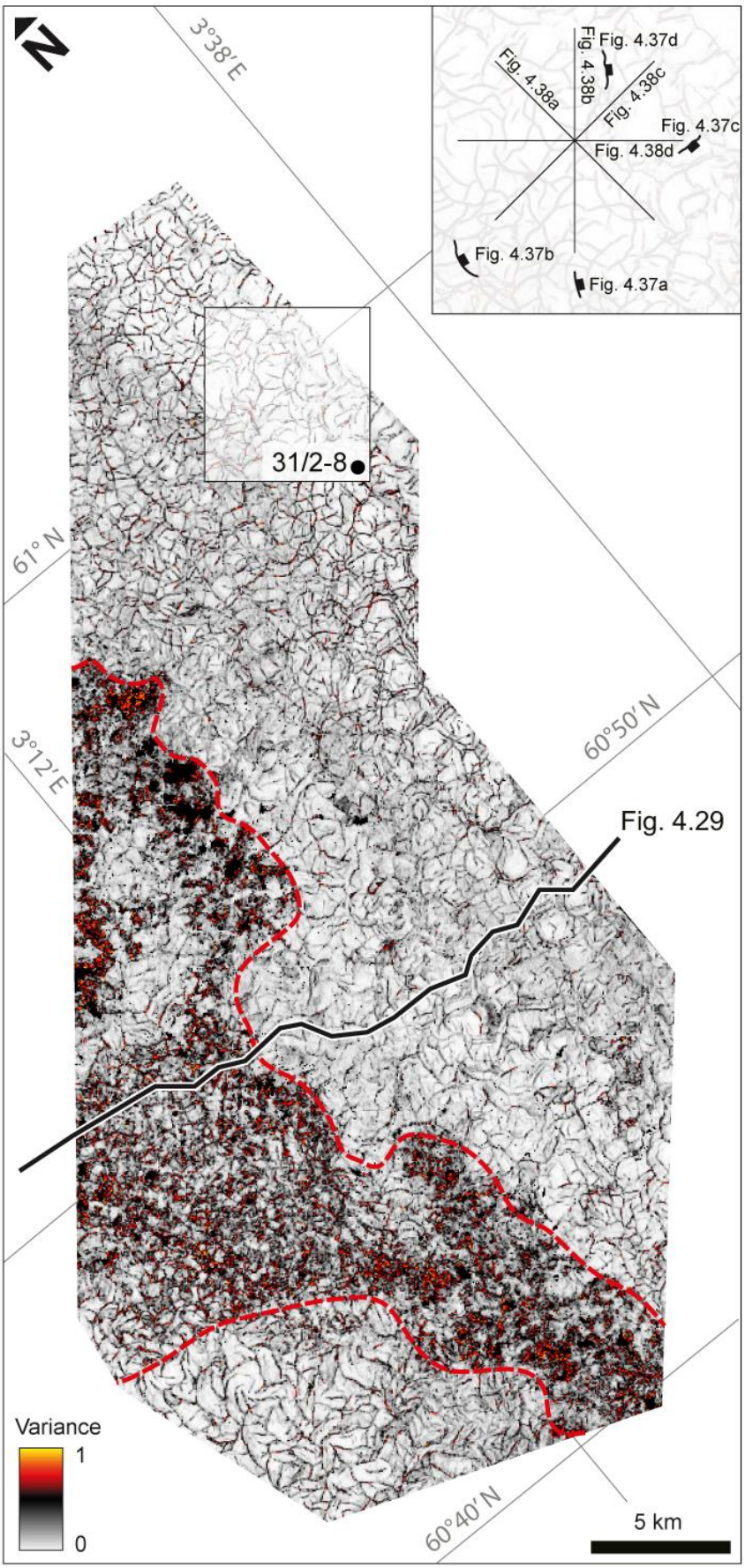


Figure 4.30: Variance attribute map showing polygonal fault pattern in the seismic reflection of the opal-A/CT transformation.

4.9.2.Depth conversion

To ascertain key fault properties (e.g. fault dip and displacement), measurements of fault height and throw need to be obtained in metres rather than milliseconds. For this reason, the selected sub-cube was converted from time to depth using check-shot data of exploration well 31/2-8 (Fig. 4.31). To depth-convert these data, four intervals of the: 1) water column, 2) Nordland Group, 3) Hordaland Group (i.e. the interval containing the polygonal fault system), and 4) the underlying strata were defined. Linear velocity-depth functions were derived for each interval using check-shot data of exploration well 31/2-8. These velocity-depth functions were then used to convert two-way traveltimes (milliseconds) into depths (metres).

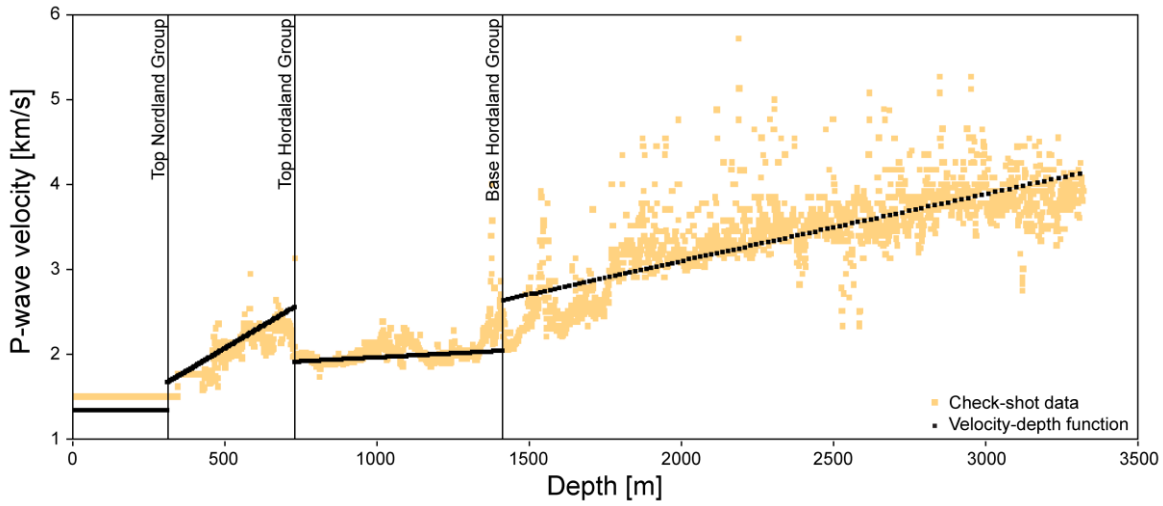


Figure 4.31: P-wave velocity-depth plot showing check-shot data of exploration well 31/2-8 (orange) and linear velocity depth functions (black), derived to convert seismic sub-cube from time to depth.

4.9.3.Fault properties

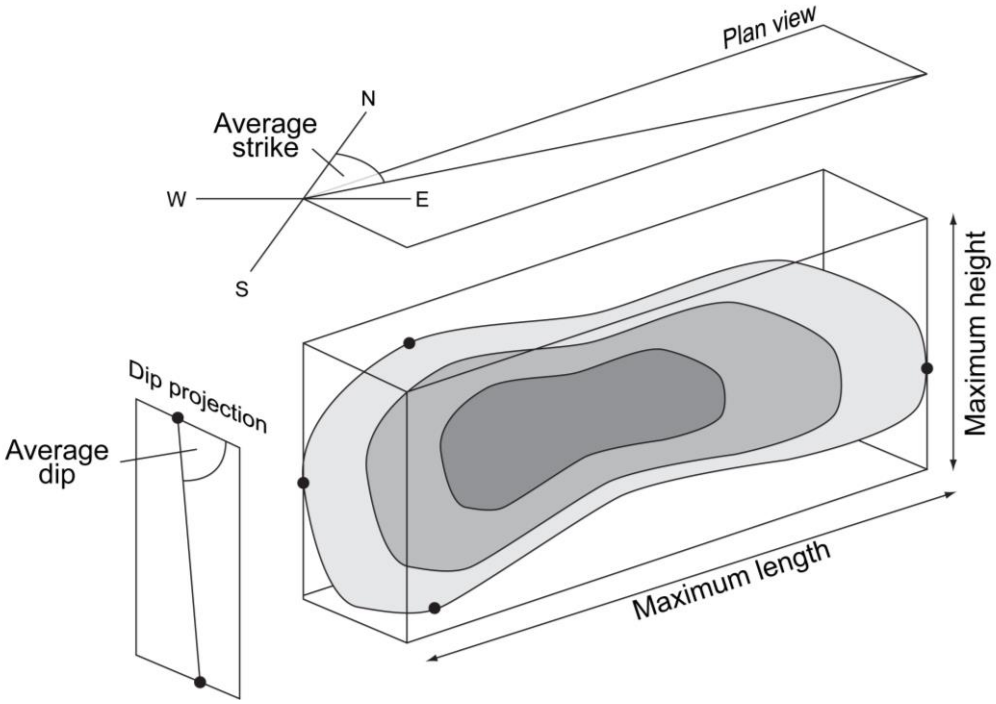


Figure 4.32: 3-D diagram of displacement distribution on normal fault illustrating the key fault properties (average strike, -dip, maximum length and -height) that are extracted in this study.

In order to constrain polygonal fault growth, 137 polygonal faults were mapped in the sub-cube using strike-perpendicular seismic sections and variance attribute slices. These faults were mapped in order to extract their maximum height and length, as well as their average strike and dip (Fig. 4.32). Displacement profiles and contours were also extracted to constrain the growth of these faults. Displacement-depth profiles were extracted from each fault using strike-perpendicular seismic sections that intersect the respective fault centres. This extraction involved the measurement of fault throw (t) and heave (h) and the calculation of the dip-parallel displacement (d):

$$d^2 = t^2 + h^2 \tag{4.28}$$

Two types of displacement-depth profiles were observed: cone-shaped, c-type (e.g. Fig. 4.33a,b) (cf. Muraoka & Kamata, 1983) and asymmetric-cone-shaped b-type displacement-depth profiles (e.g. Fig. 4.33c,d). Based on this distinction, the 137 mapped faults were sorted into two groups (Fig. 4.34). To highlight similarities and differences between these two groups, their

geometries were extracted (Fig. 4.35) and key properties were cross-plotted (Fig. 4.36). Finally, displacement contours of four polygonal faults were produced by: 1) extracting multiple displacement-depth profiles every 25 m along strike, 2) interpolating between these profiles, and 3) creating strike-projections (Fig. 4.37).

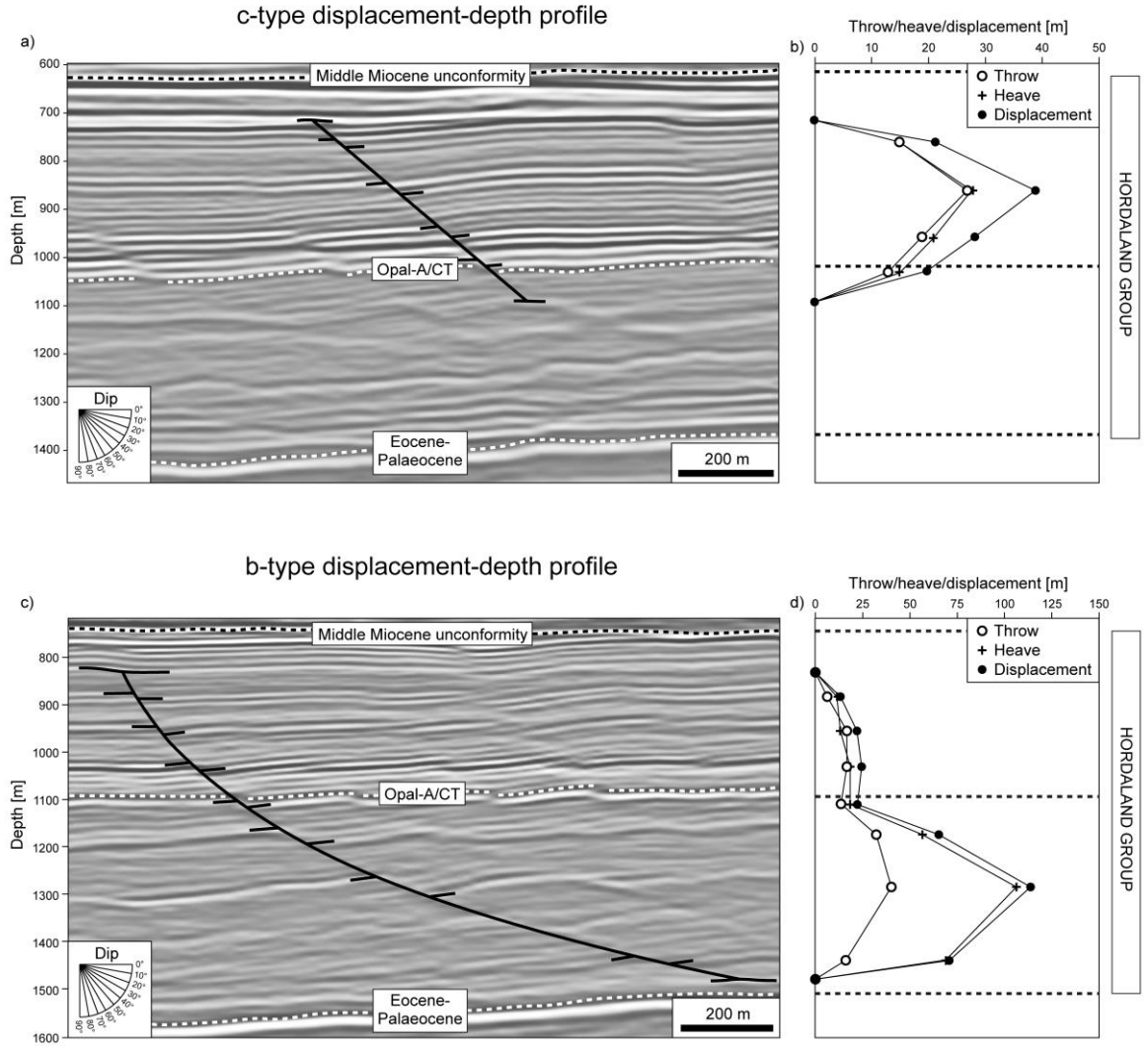


Figure 4.33: a) Example of polygonal fault with planar geometry (dip: c. *45*°) and monoclinal fold at upper fault tip shown in a seismic section without vertical exaggeration. b) Dip-parallel throw, heave and displacement derived from seismic section (a); showing c-type displacement-depth profile; c) Example of polygonal fault with listric geometry (dip: 20-50°) and monoclinal fold at upper fault tip shown in a seismic section without vertical exaggeration; d) Dip-parallel throw, heave and displacement derived from seismic section (c); showing b-type displacement-depth profile. Note that the dip-slip displacement is dominated by the fault heave.

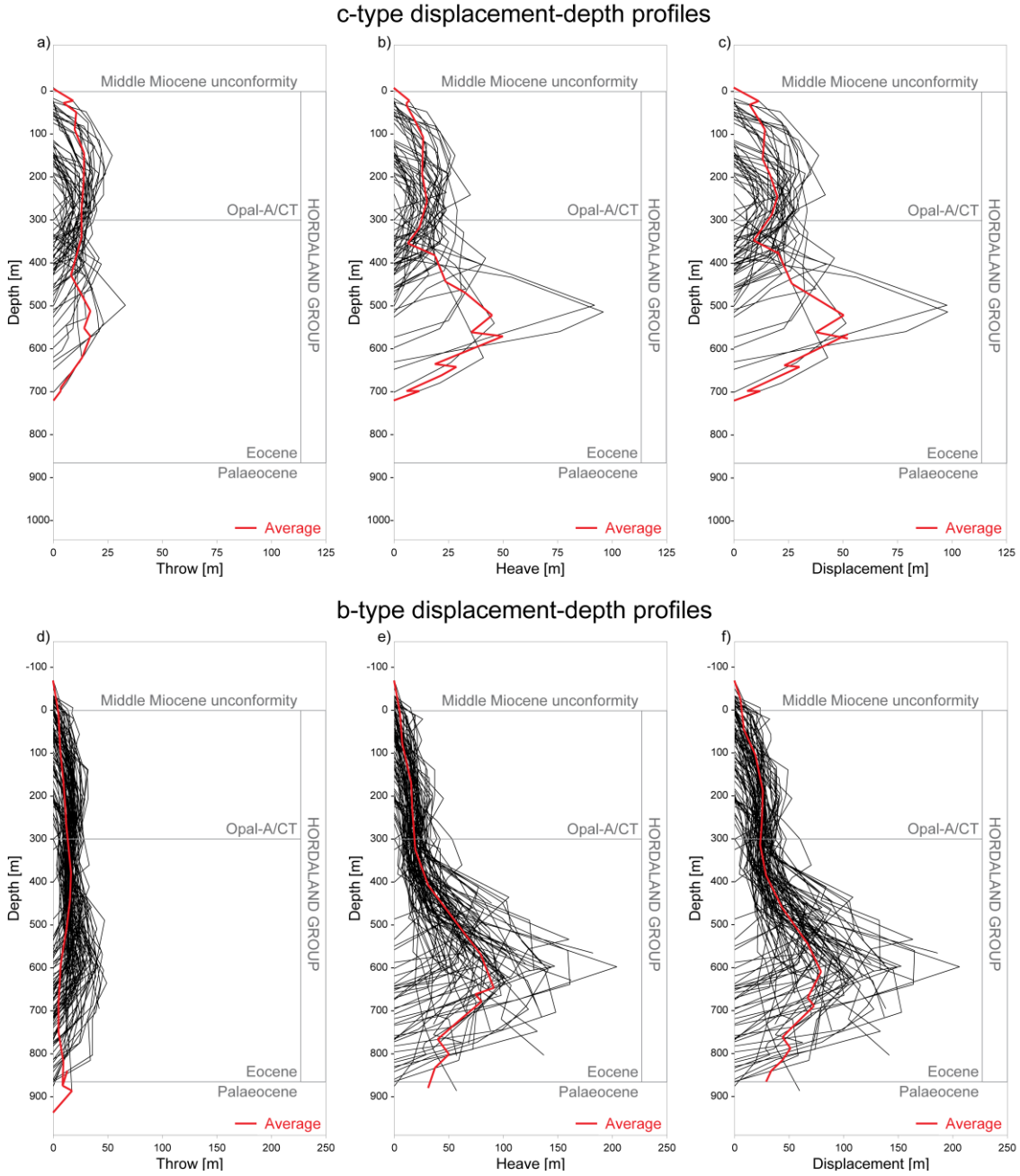


Figure 4.34: Throw-, heave- and displacement-depth profile of c-type (a-c) and b-type faults (d-f). Note that the displacement is dominated by the fault heave and that bulk heave has been accumulated in sediments that have undergone opal-A/CT transformation.

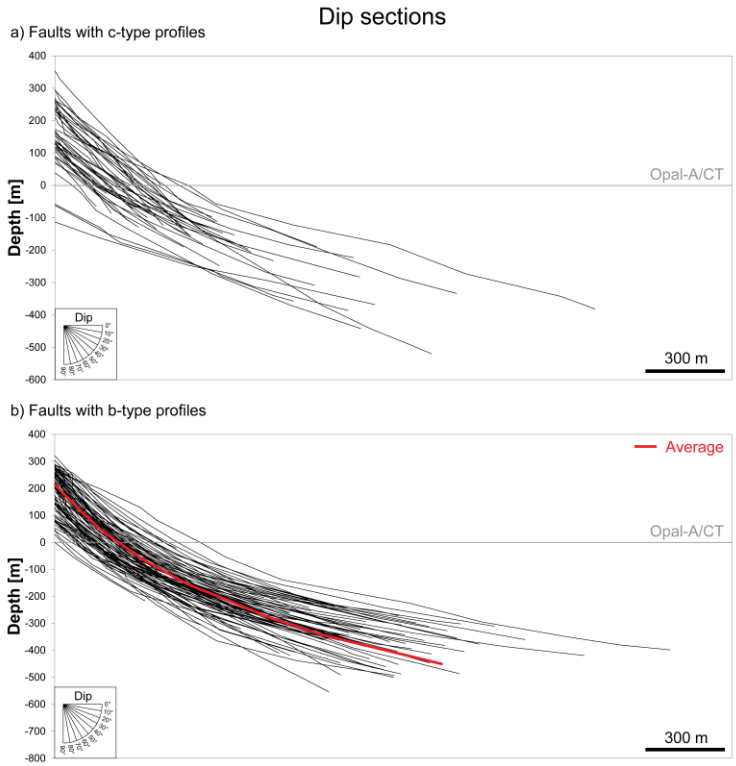


Figure 4.35: a) Planar geometries of faults with c-type displacement-depth profiles and b) Listric geometries of faults with b-type displacement-depth profiles.

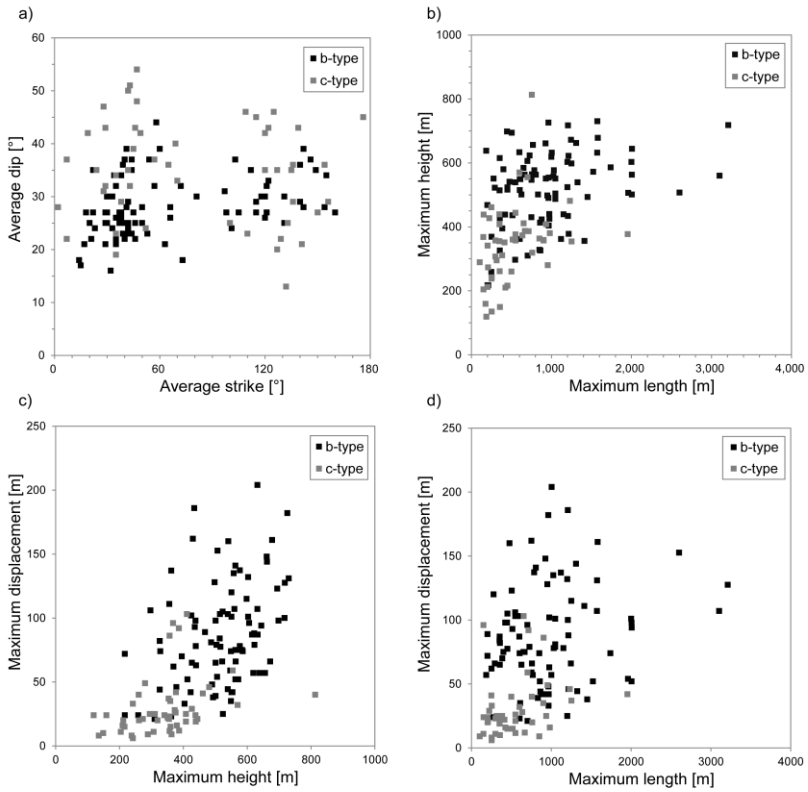


Figure 4.36: Cross-plots of a) average strike and dip, b) maximum length and height, c), maximum height and displacement, and d) maximum length and displacement of 137 polygonal faults with b-type and c-type displacement depth profiles (see Fig. 7.3). Note that these faults show no preferred orientation (a) and that b-type faults are longer, higher and accommodate more displacement than c-type faults (b-d).

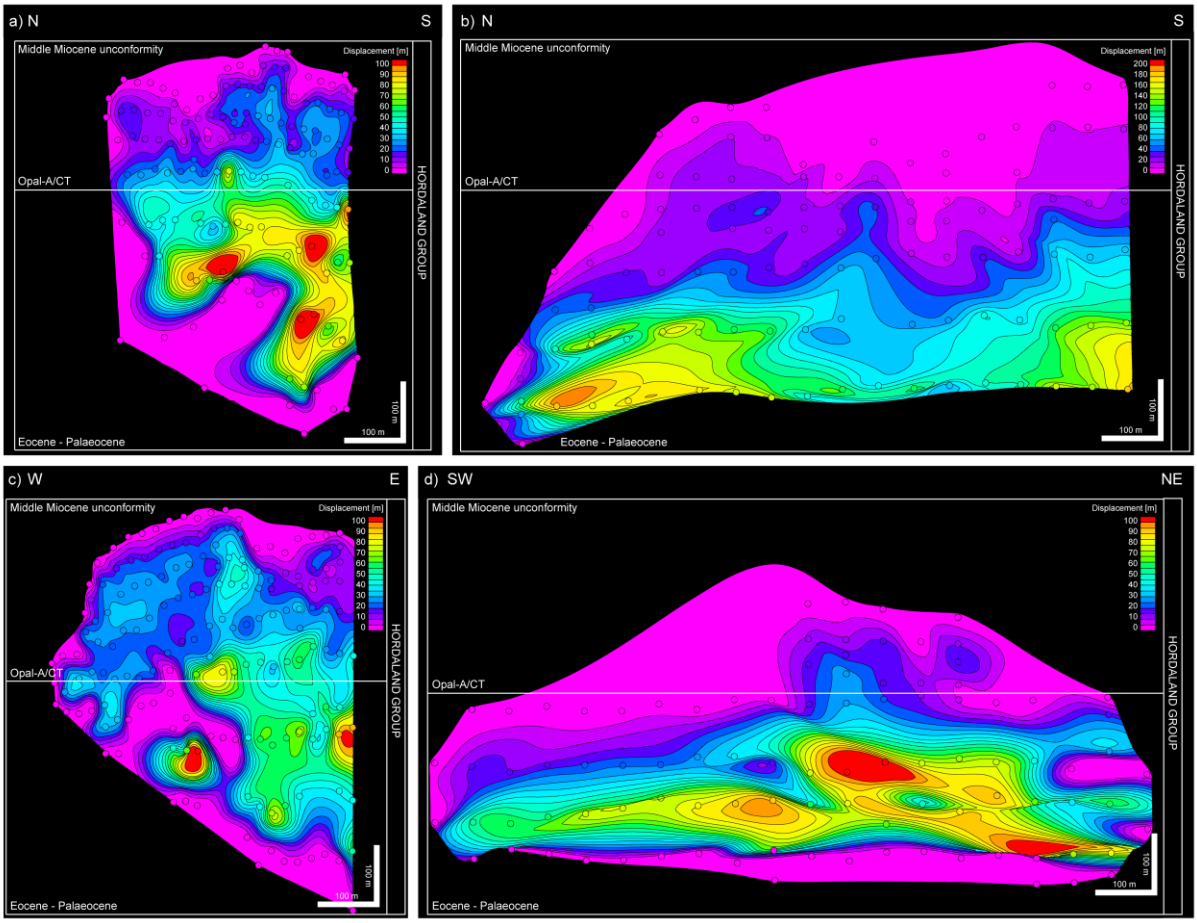


Figure 4.37: Displacement contours of four randomly-selected polygonal faults (a-d). Key observations include: 1) multiple displacement maxima at similar depth levels, 2) high displacement gradients (>1) at base and 3) low displacement gradients (<1) at the top of these faults.

4.9.4. Strain summation

To investigate the influence of silica diagenesis on polygonal faulting, the horizontal strain accumulated by the polygonal fault system is calculated. Horizontal strain is defined as the change in length (Δl) relative to the initial length of the rock volume (l_0):

$$e = \frac{\Delta l}{l_0} \tag{4.29}$$

The initial length of the host rock (l_0) is approximated by the sum of bed segments (l_i) and the change in length is calculated as the sum of the fault heaves (h_i) (Fig. 4.38):

$$\Delta l = \sum_i h_i \tag{4.30}$$

$$l_0 = \sum_i l_i \tag{4.31}$$

This approximation allows the observable strain at the fault surface, not the strain in the surrounding rock, to be quantified. To extract reliable values, strain is extracted from 5405 m long sections, sampling about 30 faults per section covering four directions at different depths.

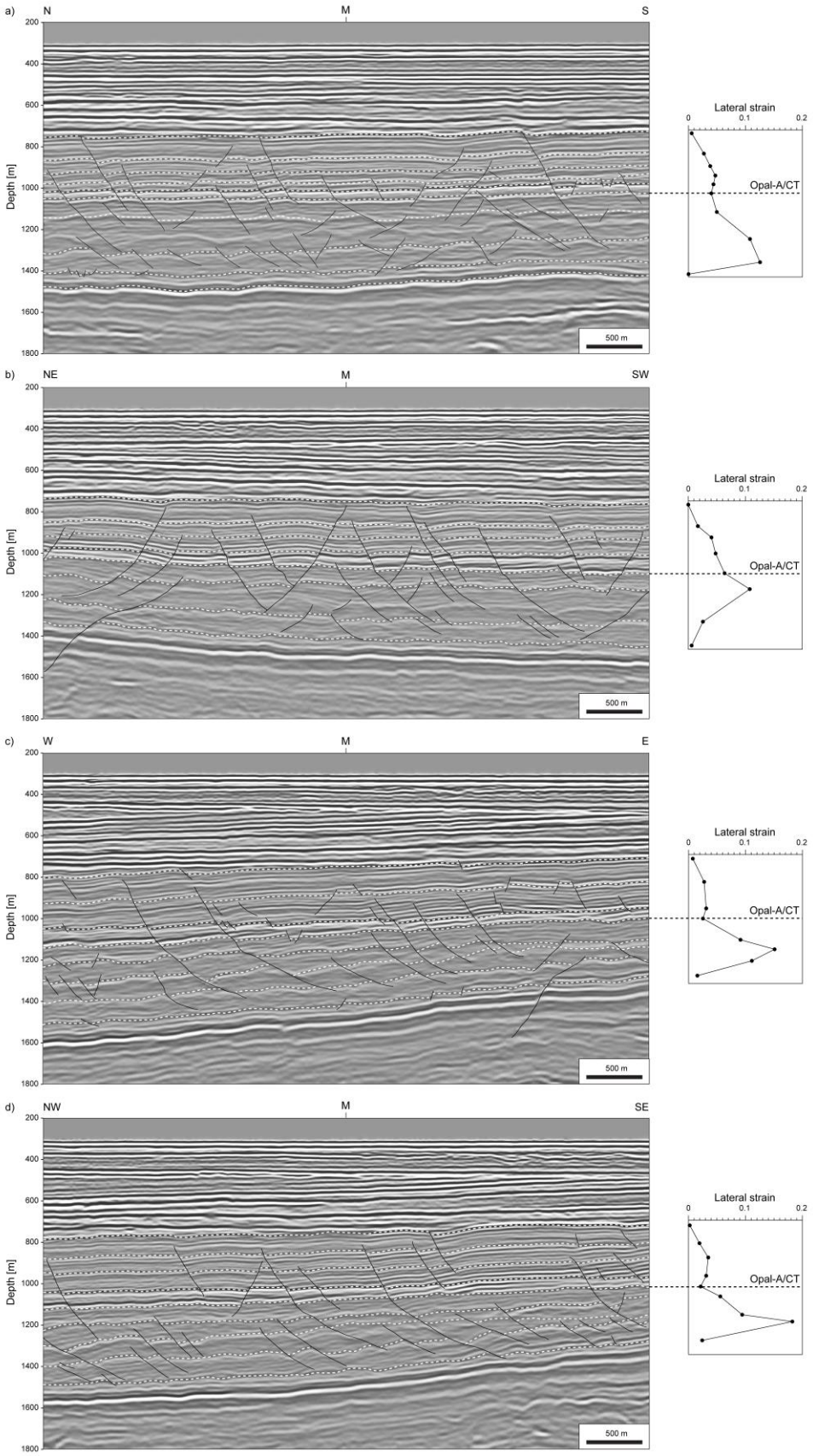


Figure 4.38: Seismic sections with strain profiles in a) N-S, b) NE-SW, c) W-E, and d) NW-SE direction. Location of sections is shown in Figure 4.30.

5. RESULTS

This section summarises observations on the host rock mineralogy, rock properties, diagenetic history and polygonal faulting in the Cenozoic rocks of the North Viking Graben, northern North Sea.

5.1. MINERALOGY

5.1.1. Clay minerals

Clay minerals constitute between 30-95% of the Cenozoic rocks of the northern North Sea with mixed-layered illite-smectite being the largest fraction (Figs. 4.5, 4.6) (Tabs. 4.3, 4.4). X-ray diffraction data reveal mixed-layer illite-smectite contents between 25-81%, illite contents of <28% and kaolinite contents of <9%.

5.1.2. Silica minerals

5.1.2.1. Opal-A

Biogenic opal-A has been previously documented in the Cenozoic mudstones of the North Viking Graben by Rundberg (1989) and Thyberg *et al.* (1999) and optical- and scanning electron microscopy show that biogenic opal-A, in fact, occurs throughout most of the Hordaland Group (Figs. 4.1, 4.2). Its chemical composition is confirmed by energy dispersive X-ray detector (Fig. 8.1). It primarily consists of diatoms, probably *Rocella vigilans* (Fig. 4.1r), *P. thybergii* (Fig. 4.2b,g,y,z), *Coscinodiscus* (Fig. 4.2i,j,n,o), and minor fractions of sponge spicules, silicoflagellates and radiolarians (Rundberg, 1989; Thyberg *et al.*, 1999). Quantitative X-ray diffraction highlights a downward decrease in opal-A content (from about 30 vol.% at 1000 m to less than 10 vol.% at 1300 m) (Figs. 4.7, 4.8).

5.1.2.2. Opal-CT

Although opal-CT has been previously suggested in the Cenozoic mudstones of the North Viking Graben based on X-ray diffraction (Rundberg, 1989; Thyberg *et al.*, 1999), scanning electron microscopy is used to image opal-CT lepispheres in remarkable detail (Fig. 4.2q-x). Its chemical composition is confirmed by energy dispersive X-ray detector (Fig. 8.1q,w,x). These lepispheres are more-or-less spherical and are approximately 2 μm in diameter (Fig. 4.2q-t). They have a dense, unstructured core (Fig. 4.2u) and a porous shell consisting of intersecting blades (Fig. 4.2t). These blades are about 200 nm wide, 200 nm wide long and up to *c.* 15 nm thick, and their edges are highly serrated (Fig. 4.2t). Quantitative X-ray reflections shows that opal-CT occurs in distinct intervals between 1200-1650 m in well 35/10-1 (Fig. 4.7) and between 1200-1400 m in well 35/11-5 (Fig. 4.8). In both wells, the opal-CT content stays below 15 vol.% (Tab. 4.3, 4.4).

5.1.2.3. Quartz

Optical-, scanning electron microscopy and X-ray diffraction data show that quartz is present throughout the Cenozoic rocks of the North Viking Graben (Figs. 4.1-4.6). Optical microscopy also shows that the quartz grains are angular, macroscopic (0.01-0.2 mm; i.e. fine-sand grade) and homogenously distributed in the matrix (Fig. 4.1). Quartz aggregates or overgrowths, as summarised by Weibel *et al.* (2010), are not observed with scanning electron microscopy (e.g. Fig. 4.2aa, bb). Quantitative X-ray diffraction shows that the quartz content is more-or-less constant throughout the succession (Figs. 4.5-4.8) with means of 17 vol.% and 15 vol.% in well 35/10-1 and 35/11-5, respectively.

5.2. ROCK PROPERTIES

This section describes compositional and depth-dependent rock property changes inferred by multiple linear regression analysis. Table 4.12 and 4.13 show the ten 'best' models predicting the host rock porosity from mineral contents and depth, selected by all subsets regression. While all of these models include opal-A content, seven also include opal-CT and pyrite content. Other mineral contents and depth are included in less than seven of the twenty models. Table 4.14 and 4.15 show detailed information of these regression models. For instance, opal-A content is statistically significant (p-value < 0.05) and the regression coefficient is positive in all twenty models. Opal-CT and pyrite content are statistically significant in two and three of the seven models, respectively. In these models, the regression coefficient associated with opal-CT content is positive, while the regression coefficient associated with pyrite is negative.

The validity of the applied multiple linear regression analysis is assessed by testing the underlying assumptions: (1) low degree of multicollinearity, (2) linearity, (3) homoscedasticity, (4) independence of error, and (6) normality of errors (e.g. Hair *et al.*, 2006). For independent variables, the variance inflation factor which quantifies the degree of multicollinearity is <4 (Tabs. 4.14, 4.15). For the models using data of well 35/10-1, the residuals which indicate degrees of linearity, are equally distributed around zero (Fig. 4.16). For models using data of well 35/11-5, the residuals slightly deviate from zero (Fig. 4.17). Moreover, residuals of well 35/10-1 are almost constant, while residual of 35/11-5 are slightly vary. Partial residual plots which indicate error independence do not vary with the independent variables (Fig. 4.18, 4.19). Normal probability plots which highlight the normality of errors show a high degree of normality (Figs. 4.20, 4.21).

5.3. SEISMIC EXPRESSION

In seismic data, the opal-A/CT transformation is shown as a continuous, high amplitude, negative seismic reflection that coincides with the top of the Lower Oligocene succession in the

eastern part of the study area (Fig. 4.23-4.24). In the western part, it cross-cuts the several stratigraphic reflections and correlates to a sharp change in seismic facies from continuous, parallel, medium-to-high amplitude reflections (above) to discontinuous, sub-parallel to chaotic, low amplitude reflections (below) (Fig. 4.24). Overall, the seismic reflection associated with the opal-A/CT transformation covers >1500 km^2 (Fig. 4.26).

5.4. BASIN MODELLING RESULTS

In this section, the basin modelling results, that provide insights into the spatial and temporal evolution of the opal-A/CT transformation, are outlined. To describe the evolution of the transformation, characteristic transformation ratios of 0.1, 0.5 and 0.9, that correspond to 10, 50 and 90% opal-A being transformed to opal-CT, are used (Figs. 5.1, 5.2).

Transformation ratio of 0.1 were first reached during the middle Eocene (44 Ma) (Fig. 5.1a). A transformation ratio of 0.5 was reached during the Late Eocene (35-38 Ma) (Fig. 5.1b). In both cases, these transformation ratios occurred in the lowest part of the Balder Formation (Fig. 5.1a,b).

These transformation ratios subsequently moved upwards, during the Eocene to Miocene through most of the Balder Formation and the lower part of the Hordaland Group (Fig. 5.1). To quantify this movement, the cumulative distance between base of the Balder Formation and the transformation ratios was calculated through time (Fig. 5.2a-c). This distance increase with time and is generally higher in the east compared to the west. The rate (i.e. distance per time) was also calculated (Fig. 5.2d-f). This rate systematically decreases with time until it reaches values around zero from the Miocene onwards.

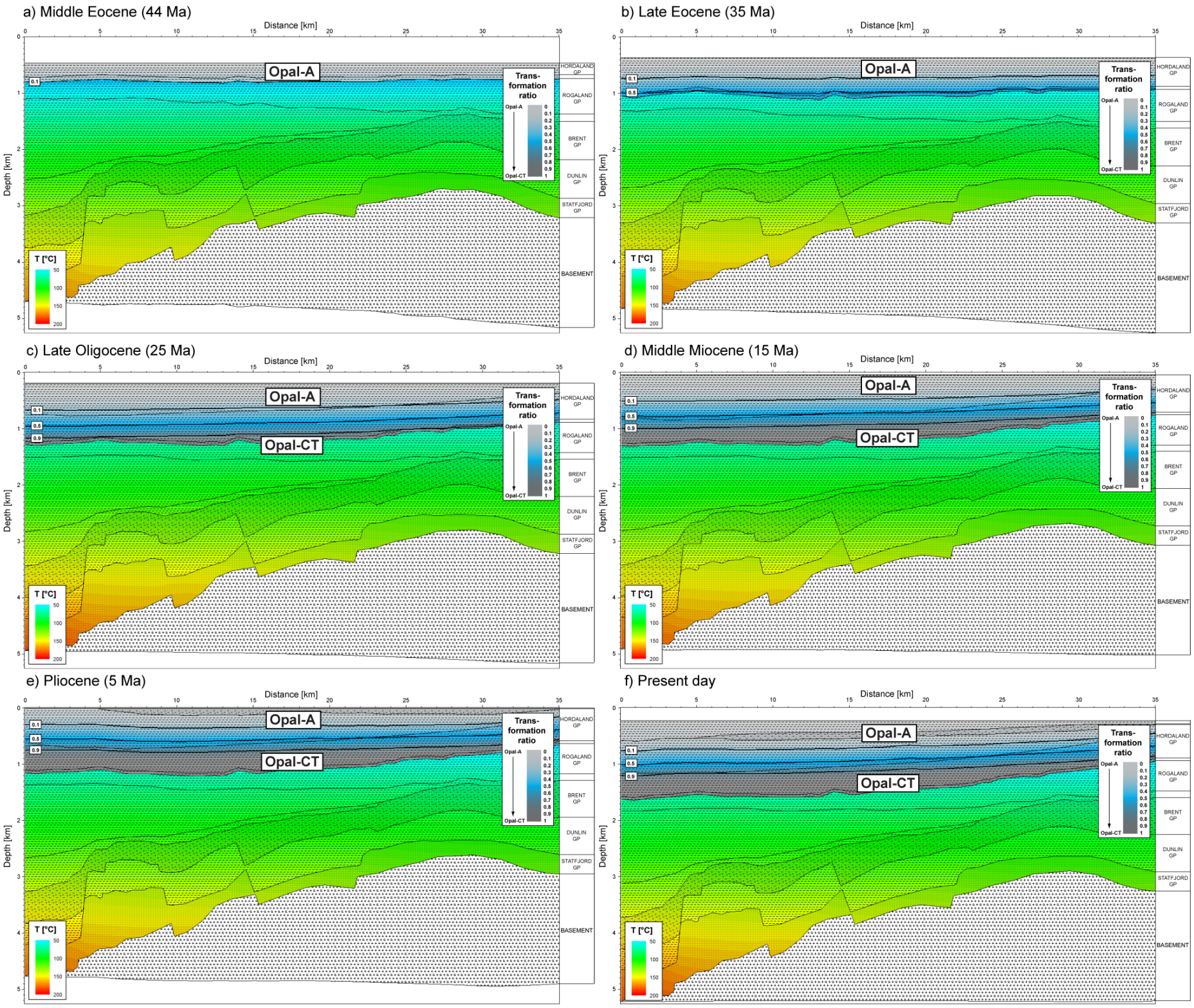


Figure 5.1: Basin modelling results for the a) Middle Eocene (44 Ma), b) Late Eocene (35 Ma), c) Late Oligocene (25 Ma), d) Middle Miocene (15 Ma), e) Pliocene (5 Ma) and present day. Note: 1) the formation of the opal-A/CT transformation zone (a-b), 2) the migration of the zone (a-f) and 3) the decrease in migration (e-f).

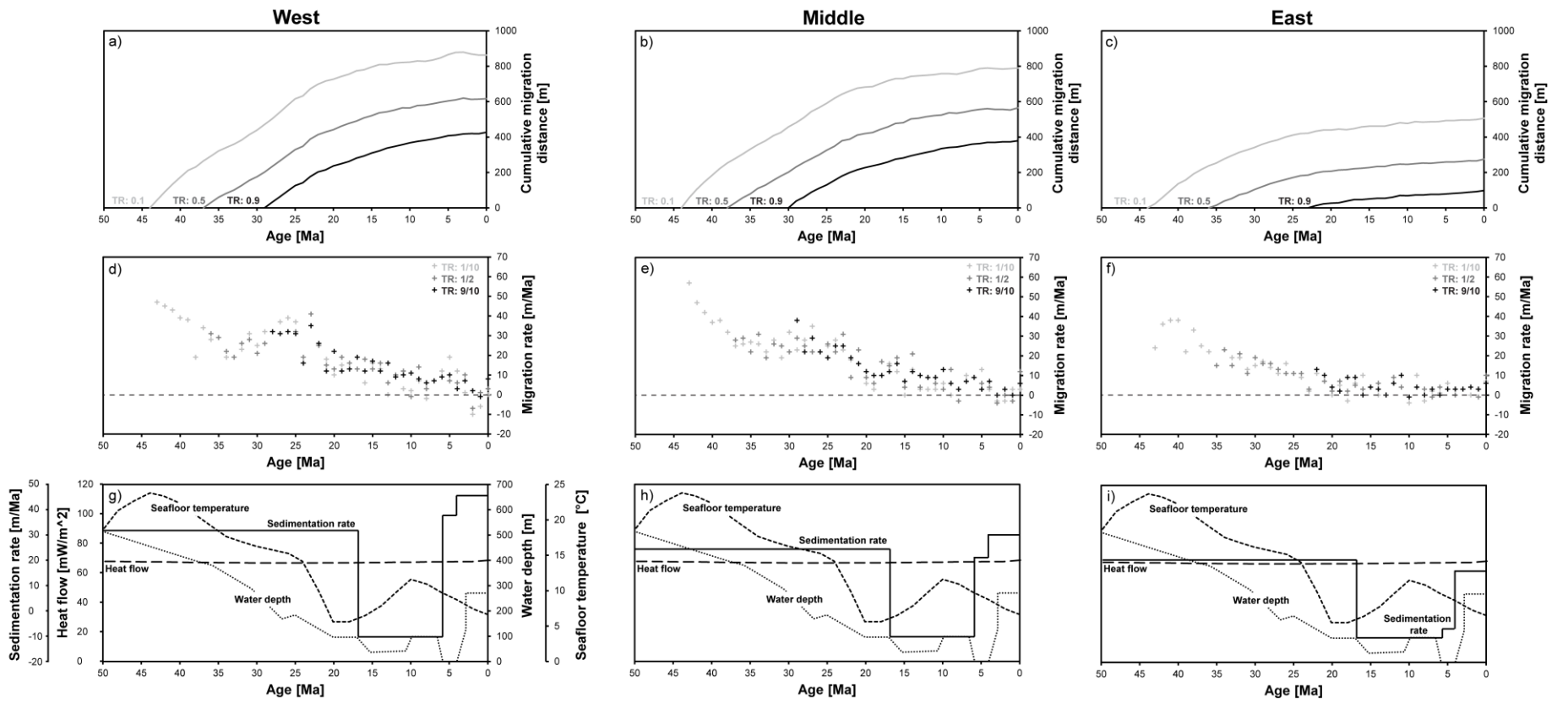


Figure 5.2: Key parameters extracted from basin modelling results. Cumulative migration distance (between various transformation ratios and the base of the Balder Formation) in the a) west (Fig. 6.7: distance: 0 km), b) middle (Fig. 6.7: distance: 17.5 km) and c) east (Fig. 6.7: distance: 35 km). Migration rate (derived from cumulative migration distance) in in the a) west (Fig. 6.7: distance: 0 km), b) middle (Fig. 6.7: distance: 17.5 km) and c) east (Fig. 6.7: distance: 35 km). g-i) Boundary conditions used for basin modelling including seafloor temperature (from Jensen & Buchardt, 1987; Anderson *et al.*, 1994), heat flow (after Lucazeau & Le Douaran, 1984) and water depth (from Kyrkjebø *et al.*, 2001).

5.5. POLYGONAL FAULTS

The polygonal faults in the North Viking Graben display no dominant orientation and show the characteristic polygonal pattern that includes numerous linked and abutted fault segments in plan-view (Fig. 4.30). The polygonal faults are generally confined to the Hordaland Group (Fig. 4.29) and have either more-or-less planar or listric geometries (Figs. 4.33, 4.34). The planar faults have average dips between *c.* 20-50°, while dips of the listric faults decreases from *c.* 50° to *c.* 20° with depth (Figs. 4.35, 4.36). The planar faults are mostly anti-thetic to listric faults (e.g. Fig. 4.29). It is furthermore worth noting that: 1) many polygonal faults are overlain by low-relief (<50 m) monoclines, 2) syn-sedimentary growth strata are not observed and 3) the opal-A/CT transformation is displaced by polygonal faults (e.g. Figs. 4.29, 4.33).

5.5.1.Displacement

The polygonal faults in the North Viking Graben have either a cone-shaped, c-type (e.g. Fig. 4.33a,b) (cf. Muraoka & Kamata, 1983) or an asymmetric-cone-shaped, b-type displacement-depth profile (e.g. Fig. 4.33c,d). Overall, 36% (49 of 137) of the mapped polygonal faults have cone-shaped, c-type displacement-depth profiles (Fig. 4.34a-c) and 64% (88 of 137) have asymmetric-cone-shaped b-type profiles (Fig. 4.34d-f). There is a correlation between displacement-depth profiles and fault geometries, as faults with c-type profiles are planar and faults with b-type profiles are listric (Figs. 4.34, 4.35). Faults with b-type displacement-depth profiles are also longer, higher and accommodate more displacement than faults with c-type profiles (Fig. 4.36c, d).

A key observation of this study is that the polygonal faults with b-type profiles show the highest displacement values (up to 200 m) in strata below the current opal-A/CT transformation (Fig. 4.34f). While observed fault heaves are particularly high (Fig. 4.34e), fault throws are only slightly increased in these strata (Fig. 4.34d). It is also worth noting that fault heave and displacement abruptly

increase from <50 m at the opal-A/CT transformation to sometimes >100 m about 300 m below the transformation.

The displacement contours also show the highest displacement values (up to 150 m) in strata below the opal-A/CT transformation (Fig. 4.37). In addition, these contours highlight that the polygonal faults often have multiple displacement maxima at similar depth levels along-strike. Finally, it is worth noting that displacement profiles and contours show that the b-type faults have relatively low gradients (<1) at their upper tips (Figs. 4.34f, 4.36).

5.5.2.Strain

The observed lateral strain profiles (Fig. 4.38) show the same shape as the b-type fault heave depth profiles, irrespective of their orientation (Fig. 4.34e). While lateral strains are <0.05 in the upper Hordaland Group, lateral strains are generally higher (<0.2) in the lower Hordaland Group. Strain maxima are therefore observed in the lower Hordaland Group (i.e. below the opal-A/CT transformation)

6. DISCUSSION & CONCLUSIONS

6.1. MINERALOGY

Because the Cenozoic rocks of the northern North Sea consist mainly of clay minerals (Figs. 4.5, 4.6), the clay mineralogy is reviewed before silica diagenesis is discussed.

6.1.1. Clay minerals

Clay minerals constitute between 30-95% of the Cenozoic rocks of the northern North Sea with (mixed-layered) illite-smectite being the largest fraction (Tabs. 8.1, 8.2) (Figs. 4.5, 4.6).

6.1.1.1. Illite-smectite

X-ray diffraction data reveal (mixed-layer) illite-smectite contents between 25-81% in the Cenozoic succession of the North Viking Graben (Figs. 4.5, 4.6). There is a consensus that Palaeocene-to-Eocene illite-smectite originates from alteration and weathering of volcanic ash deposited during rifting of the North Atlantic (Karlsson *et al.*, 1979; Pearson & Small, 1988; Rundberg, 1989; Pearson, 1990; Thyberg *et al.*, 2000). Subsequent erosion of these sediments in response to Oligocene uplift probably sourced smectite deposition in this time (see Pearson, 1990; Huggett, 1992; Thyberg *et al.*, 2000). The downward decrease in smectite and increase in illite content within the Cenozoic succession is explained by smectite-to-illite transformation in response to increasing pressures and temperatures during burial (Karlsson *et al.*, 1979; Pearson & Small, 1988; Rundberg, 1989; Pearson, 1990; Marcussen *et al.*, 2009).

6.1.1.2. Illite

X-ray diffraction data document illite (<28%) in the upper part of the Cenozoic succession of the North Viking Graben (Figs. 4.5, 4.6). Illite is either sourced by weathering of igneous or metamorphic rocks or by reworking of sedimentary rocks (Pearson, 1990).

6.1.1.3. Kaolinite

X-ray diffraction data are indicative of small amounts of kaolinite (<9%) in the upper part of the Cenozoic succession of the North Viking Graben (Figs. 4.5, 4.6). Kaolinite is produced by soil weathering in humid climate, by alteration of volcanic ash or by authigenesis in sedimentary rocks (Pearson, 1990).

6.1.2.Silica minerals

In this section, the origin of opal-A, opal-CT and quartz as well as the opal-A/CT and opal-CT/Q transformation in Cenozoic rocks of the northern North Sea are discussed.

6.1.2.1. Opal-A

Opal-A is defined as amorphous (i.e. non-crystalline), hydrous silica by Jones and Segnit (1971) and is either bio- or volcanogenic in origin (e.g. Hesse, 1988; Treguer *et al.*, 1995). In this case, opal-A is biogenic, as it consists of biosiliceous material of diatoms and minor fractions of sponge spicules, silicoflagellates and radiolarians (Figs. 5.2, 5.3) (Rundberg, 1989; Thyberg *et al.*, 1999).

X-ray diffraction data show that the opal-A content is highest at the top of the logged part of the Cenozoic succession and gradually decreases with depth (Figs. 5.4, 5.5); a trend that may have been influenced by silica deposition and/or diagenesis. Diagenetic reductions of opal-A content, for

example during opal-A/CT transformation, typically occur in distinct depth intervals (e.g. Isaacs, 1981; Compton, 1991; Ireland *et al.*, 2011). Minor opal-A content variation in the potential opal-A/CT transformation zone are therefore likely to be caused by diagenesis. The overall downward decline in opal-A content, in particular above the opal-A/CT transformation zone, is however uncharacteristic for diagenesis and therefore seems to be depositional (Figs. 5.4, 5.5).

If correct, the interpretation that vertical (i.e. temporal) variations in opal-A are controlled by deposition rather than diagenesis implies that the amount of opal-A deposited between the Eocene and Miocene must have increased relative to other minerals. There are at least three factors that may explain this increase. First, upwelling of nutrient-rich water could have increased silica production in surface waters. Thyberg *et al.* (1999) suggest that the palaeo-bathymetry together with water currents in north-south direction could have resulted in upwelling in the northern North Sea. This suggestion is supported by the observation of a persistent, palaeo-bathymetric high between 60 and 61°N in the northern North Sea between the Eocene and Miocene (Wien & Kjennerud, 2005). Second, terrigenous sediment input could have increased the nutrient content of and thereby the silica production in surface waters (DeMaster, 2002). In the context of the tectono-stratigraphic setting of the North Sea during the Oligocene, increased terrigenous sediment input from Norway (e.g. Jordt *et al.*, 1995; Faleide *et al.*, 2002; Anell *et al.*, 2012) may have driven increased near-surface nutrient content and thus silica deposition. Third, increasing silica deposition may reflect increasing preservation of biogenic silica. In terms of volume, silica preservation could be more important than production, considering that the observed biogenic silica is often partially dissolved (e.g. Fig. 5.3c) and that the present global silica preservation ratio is only 3% (Treguer & De La Rocha, 2013). Unfortunately, biogenic silica preservation is difficult to constrain, as the controlling factors are currently not well-understood. In the future, the study of the global silica cycle may allow the factors controlling silica preservation to be determined.

In summary, the overall decline in opal-A content with depth above the opal A/CT transformation zone, is most likely the result of increasing biogenic opal-A deposition from the Eocene to the Miocene. This increase in biogenic opal-A deposition may be explained by: 1)

upwelling, 2) terrigenous sediment input, and/or 3) silica preservation between the Eocene and Miocene. Based on our current knowledge and the availability of detailed palaeo-bathymetry data of the northern North Sea (e.g. Wien & Kjennerud, 2005), upwelling currently seems to provide the most likely explanation for increased biogenic opal-A deposition.

6.1.2.2. Opal-CT

Opal-CT consists of lepispheres, i.e. spheres of intertwined, microcrystalline cristobalite and tridymite blades that are precipitated from silica-rich solution (Jones & Segnit, 1972; Flörke *et al.*, 1976; von Rad *et al.*, 1978; Williams & Crerar, 1985). Scanning electron microscopy and X-ray diffraction confirms that opal-CT is present in the Cenozoic succession of the North Viking Graben (Rundberg, 1989; Thyberg *et al.*, 1999) (Figs. 5.3q-x, 5.4, 5.5). To precipitate opal-CT, the silica concentration of the pore fluids must exceed the solubility of opal-CT. These conditions were probably achieved by opal-A dissolution, as indicated by the negative correlation between opal-A and opal-CT content (Fig. 5.6a). An alternative interpretation is that the silica for the opal-CT precipitation was supplied by smectite dissolution. There is however no evidence for *in-situ* smectite dissolution leading to opal-CT precipitation (Fig. 5.6b). Even though it may be possible that opal-CT precipitation was partially sourced by the upward migration of silica-rich pore fluids released by smectite dissolution of the underlying rocks (Marcussen *et al.*, 2009; Thyberg *et al.*, 2010), opal-A dissolution seems to have been the primary source for opal-CT precipitation.

This implies that the opal-A dissolution and opal-CT precipitation were coupled and that the Cenozoic rocks of the North Viking Graben have indeed undergone opal-A/CT transformation. The opal-A/CT transformation has been demonstrated to be controlled by time, temperature and pH (see review by Williams & Crerar, 1985; Williams *et al.*, 1985), whereby the pH of the pore fluids can be affected by the host lithology or organic material (Kastner *et al.*, 1977; Hinman, 1990). Because the opal-A/CT transformation does not coincide with major lithology variations and organic material has not been documented (Figs. 5.4, 5.5), it seems that these two factors played a minor role. Instead, it

appears that the opal-A/CT transformation was primarily controlled by time and temperature; an interpretation that is supported by experimental studies by Mizutani (1967), Mizutani (1970), Kastner *et al.* (1977) and Kastner and Gieskes (1983).

A final observation is that opal-CT disappears below certain depths in the Hordaland Group (Fig. 4, 5). This may indicate that opal-CT precipitation did not occur below these depths or that it did occur, but was then followed by opal-CT dissolution. It seems unlikely that the opal-CT was not precipitated below these depths, considering that the same conditions (sufficient silica concentration in pore fluids, time and temperature) which led to opal-CT precipitation above these depths, were probably also reached below. It therefore seems more plausible that the meta-stable opal-CT was first precipitated and then fully dissolved below these depths (Figs. 5.4, 5.5).

In summary, quantitative mineralogical data (Figs. 5.4-5.6) can be used to show that opal-A dissolution most likely sourced opal-CT precipitation, i.e. that opal-A was indeed transformed into opal-CT as suggested by Rundberg (1989) and Thyberg *et al.* (1999).

6.1.2.3. Quartz

Sedimentary rocks may contain detrital and/or authigenic quartz. Detrital quartz is the result of weathering, transport and deposition of quartz bearing rocks, whereas authigenic quartz is formed in-situ by precipitation. The Cenozoic rocks of the northern North Sea contain detrital quartz (Figs. 5.2, 5.3) (Peltonen *et al.*, 2009; Kalani *et al.*, 2014) and even though authigenic quartz has been documented in the underlying Cretaceous and Palaeocene rocks (Marcussen *et al.*, 2009; Thyberg *et al.*, 2010; Thyberg & Jahren, 2011), scanning electron microscopy revealed no evidence for authigenic quartz in the samples of this study.

The formation of authigenic quartz requires a series of chemical and physical conditions to be reached, including the presence of silica-rich pore fluids and a thermodynamic driving force to reduce the free energy of the system (e.g. Worden & Morad, 2000). The absence of authigenic quartz

therefore indicates that at least one of these conditions was not reached in Cenozoic mudstones of the North Viking Graben. It is unlikely that the silica concentration of the pore fluids was too low, considering that opal-A and opal-CT were dissolved (see above). Interestingly, opal-CT dissolution appears to have not led to quartz precipitation, as there is no correlation between the opal-CT and quartz contents in the potential opal-CT/Q transformation zone (Fig. 5.6c). The absence of authigenic quartz, despite opal-CT dissolution, could be explained by the migration of silica-rich pore fluids or insufficient heating of the host rock during burial. If the silica-enriched pore fluids were moved out of the system, quartz precipitation could have been prevented. Alternatively, insufficient heating of the host rock during burial could have hampered quartz precipitation. Assuming they were heated from 10°C to 60°C between 50 Ma and the present day, which may be an overestimate, only 1% of the silica in solution would have formed authigenic quartz according to the kinetics of Rimstidt and Barnes (1980). The quartz found in the Cenozoic rocks of the North Viking Graben is most likely detrital, rather than authigenic in origin. This means that these rocks have not undergone opal-CT/Q transformation.

6.2. ROCK PROPERTIES

The Cenozoic rocks of the northern North Sea consist mainly of clay minerals (Figs. 4.5, 4.6), physical property changes as a result of the clay mineralogy are therefore reviewed before physical property changes as a result of silica diagenesis are discussed.

6.2.1. Clay minerals

In this section, physical property changes as a result of variations in the clay mineralogy are summarised based on previous studies. Marcussen *et al.* (2009), for instance, predict the smectite-to-illite transformation to start around 70°C and to increase the p-wave velocity and bulk density of the host rock. Considering surface temperatures of c.10°C, a geothermal gradient of c.30°C/km, the illite-smectite transformation would start about 2 km below the surface which is below the studied succession. Observed physical property changes therefore cannot be the result of the illite-smectite transformation.

Depositional clay mineral variations may however affect the physical properties of the studied rocks. In particular, smectite reduces the bulk density and p-wave velocity of the host rock (Mondol *et al.*, 2007). Marcussen *et al.* (2009) highlight a downward increase in smectite content that is associated with bulk density and p-wave velocity reductions of the Cenozoic rocks of the northern North Sea. Observed physical property changes must therefore be checked for effect of depositional clay mineral variations.

6.2.2. Silica minerals

To assess the effect of silica minerals on the host rock porosity, multiple linear regression analysis is applied to model the compositional and depth dependency of porosity for exploration well 35/10-1 and 35/11-5. Multiple linear regression is an approach to model the relationship between a

dependent variable and a set of independent variables. In this study, the independent variables may include the mineral contents and depth and the dependent variable is the host rock porosity To select the independent variables appropriately, all subset regression is applied. All subsets regression compares all possible regression models based on a subset of independent variables and then ranks them based on a pre-defined criterion. In this study, all subsets regression is used to select the ten 'best' models based on the Bayesian information criterion (Schwarz, 1978) which accounts for model fit, the number of observations, and the number of independent variables.

The ten best models selected by all subsets regression are listed in Table 4.12 and 4.13. Opal-A content is included, is statistically significant and its regression coefficient is positive in all models (Tabs. 4.12-4.15). These results highlight that, assuming that the relationship between host rock porosity, depth and composition can be modelled with multiple linear regression, opal-A content explains host rock porosity variation to a large extent. Moreover, seven of twenty models selected by all subset regression include opal-CT and pyrite content (Tabs. 4.12, 4.13). Opal-CT and pyrite content are statistically significant in two and three of the seven models, respectively (Tabs. 4.14, 4.15). In these models, the regression coefficient associated with opal-CT content is positive and the regression coefficient associated with pyrite is negative. These results highlight that, assuming that their relationship can be modelled with multiple linear regression, opal-CT and pyrite content are variables that explain host rock porosity variations to a lesser degree. Other mineral contents (e.g. Illite-smectite) and depth are included in less than seven of the twenty models and are not statistically significant in any of the models (Tabs. 4.12-4.15) highlighting that they do not explain host rock porosity variations using multiple linear regression analysis. In summary, opal-A content explains host rock porosity to a large extent and opal-CT and pyrite content explain host rock porosity to a lesser degree.

The validity of multiple linear regression analysis depends on five assumptions: (1) low degree of multicollinearity (2) linearity, (3) homoscedasticity, (4) independence of errors, and (5) normality of errors (e.g. Hair *et al.*, 2006). First, the degree of multicollinearity which describes correlation among independent variables is assessed using the variation inflation factor (Tabs. 4.14, 4.15). Since

variance inflation factors are <4, the degree of multicollinearity is low. Second, linearity between the independent and dependent variables is assessed using residual plots. While residuals of models using data of well 35/10-1 are equally distributed around zero highlighting a high degree of linearity (Fig. 4.16), residuals of models using data of well 35/11-5 slightly deviate from zero highlighting minor curvilinearity (Fig. 4.17). Third, homoscedasticity which is the constancy of errors is also assessed using residual plots. Again, residuals of models using data of well 35/10-1 are almost constant highlighting a high degree of homoscedasticity (Fig. 4.16), while residuals of models using data of well 35/11-5 slightly vary with porosity highlighting minor heteroscedasticity (Fig. 4.17). Fourth, independence of errors is assessed using partial residual plots. The partial residuals do not vary systematically with the independent variables highlighting a high degree of independence of errors in models of both wells (Figs. 4.18, 4.19). Fifth, normality of errors is assessed using normal probability plots. These plots show that the residuals of models of both wells are close to the linear functions representing normal distributions (Figs. 4.20, 4.21). In summary, the models satisfy the five assumptions of multiple linear regression analysis and are therefore valid.

6.3. EXTENT OF OPAL-A/CT TRANSFORMATION

This section describes the extent of silica diagenesis in the North Viking Graben. Because the opal-A/CT transformation reduces the host rock porosity, it increases its acoustic impedance (bulk density × p-wave velocity) and produces a mappable seismic reflection (Fig. 4.22). Using five volumes of 3-D seismic reflection data and sixteen exploration wells, the opal-A/CT transformation is mapped over >1500 km^2 (Fig. 4.23-4.26). Assuming that the opal-A/CT transformation zone is at least 50 m thick, the transformation zone affects >75 km^3 of sediments. As such, the opal-A/CT transformation is a key feature of the Cenozoic succession affecting a large volume of sediments

6.4. DIAGENETIC HISTORY

6.4.1. Opal-A preservation

In this section, the preservation of opal-A below the present opal-A/CT transformation zone is discussed. Considering that X-ray diffraction can overestimate opal-A contents by >10% (Conley, 1998), the observation of c.10% opal-A below the transformation could be interpreted as a measurement artefact. Previous studies however document that opal-A is preserved down to 1500 m depth in the northern North Sea (Thyberg et al., 1999) suggesting that the observation of opal-A below the transformation is a real phenomenon. This interpretation challenges our assumption that the transformation was primarily time-temperature dependant (see Section 4.8.1.) and thus other parameters need to be considered. The presence of opal-A below the transformation zone suggests that opal-A was not fully dissolved in these rocks, which may be explained by various factors. For example, Thyberg et al. (1999) suggest that the preservation of opal-A depends on the silica-producing biota; i.e. biosiliceous material of sponge spicules and radiolarians being more resistant to dissolution than that of diatoms; a hypothesis that could be tested by optical- and scanning electron microscopy in the future. Williams et al. (1985) argue that the preservation of opal-A depends on the surface area; i.e. the higher the surface area, the higher the solubility. Opal-A preservation can also be enhanced by the formation of detrital surface coatings (e.g. Rickert et al., 2002; Michalopoulos & Aller, 2004). Although these controls may have been active, they cannot be assessed with the available data. Furthermore, we suggest that the persistence of opal-A below the transformation zone is not at odds with the time-temperature dependency of opal-A dissolution. Assuming that the amount of opal-A that is dissolved depends on the time the host rocks were subject to certain temperatures (see Section 4.8.1.), the persistence of opal-A beneath the transformation zone may be a result of the host rock not being subject to sufficient temperatures for a sufficient period of time. The times and temperatures required to complete opal-A dissolution depend on the initial opal-A content; i.e. the more opal-A is present, the longer it takes to fully dissolve it. Opal-A could, for example, fully dissolve in rocks with low initial opal-A contents, whereas it may still be present in rocks that have

been subject to exactly the same temperatures and for the same time because they had higher initial contents. The persistence of opal-A may also be explained by supersaturation of the pore fluids. Supersaturation of the pore fluids with respect to opal-A and opal-CT might be achieved by opal-A dissolution. If fluid migration is limited and opal-CT precipitation slow, the pore fluids may remain supersaturated (with respect to opal-A) and further opal-A dissolution would be inhibited. In these ways, the preservation of opal-A below the transformation zone can thus be explained by the time-temperature dependency of opal-A dissolution.

To summarise, there are many possible explanations for the preservation of opal-A below the opal-A/CT transformation zone, five of which are presented above. Unfortunately, the validity of these explanations cannot be assessed with the available data. It therefore remains unclear what led to the persistence of opal-A below the transformation zone. Because of this uncertainty, the persistence of opal-A cannot be used to identify the controls on the opal-A/CT transformation in the North Viking Graben. In accordance with numerous experimental studies (e.g. Mizutani, 1967; Kastner et al., 1977; Kastner & Gieskes, 1983; Williams et al., 1985; Duffy, 1993; Dove & Rimstidt, 1994) we assume that the opal-A/CT transformation is, as a first-order approximation, time-temperature dependent. In future, it might be possible to determine the factor(s) controlling opal-A preservation and to describe their influence on the opal-A/CT transformation using different kinetics.

6.4.2. Evolution of opal-A/CT transformation

The evolution of the opal-A/CT transformation has been previously divided into three stages: 1) formation, 2) migration, 3) fossilisation (Davies & Cartwright, 2002). This division is adapted to discuss the timing, movement and controls on the opal-A/CT transformation modelled in this study. It is worth noting that this study is the first of its kind and the presented results will improve with the precision of the input parameters.

6.4.2.1. Formation

The formation of the opal-A/CT transformation zone has been previously described as the point when a minimum transformation temperature has been reached (Davies & Cartwright, 2002). This definition makes sense, if it is assumed that the transformation starts at a well-defined temperature. If the opal-A/CT transformation rate is calculated, 'the formation of the opal-A/CT transformation' must be refined. According to Arrhenius' (1889) equation, the transformation rate is low at low temperatures (Fig. 4.28). It therefore makes sense to define the formation as the first time a specific transformation ratio (of opal-A to opal-CT) is reached. Transformation ratios of 0.1 and 0.5 are suggested as upper and lower boundaries, respectively. If we define the 'start of transformation' as the first time a transformation ratio of 0.1 is reached, then basin modelling indicates that the opal-A/CT transformation started in the middle Eocene in the lower part of the Balder Fm(c.44 Ma) (Figs. 5.1, 5.2). A transformation ratio of 0.5 has been reached in the Late Eocene (c.35-38 Ma). For any other transformation ratio between 0.1 and 0.5, the 'start of transformation' can be estimated using Figure 10a-c.

Although this model predicts the opal-A/CT transformation zone to form in the lowest part of the Balder Formation which marks the onset of siliceous deposition in the North Viking Graben (Rundberg, 1989), it is possible that transformation zone formed at a shallower level. The opal-A/CT transformation zone could have even formed close to its current position. In either case, the opal-A/CT transformation zone formed due to increasing sediment temperatures as a result of burial of the host strata.

In this model, the formation of the opal-A/CT transformation occurred in a period of: 1) broadly constant sedimentation, 2) broadly constant heat flow, 3) an overall decrease in water depth and 4) relatively high seafloor temperatures (Fig. 5.2). Especially striking is the correlation between the middle Eocene seafloor temperature maximum, documented by oxygen isotope studies from the North Sea (Buchardt, 1978; Jensen & Buchardt, 1987; Anderson et al., 1994), and the formation of the opal-A/CT transformation zone (Fig. 10). This correlation may indicate that the temperature maximum controls the timing of opal-A/CT transformation zone formation.

6.4.2.2. Migration

The migration of the opal-A/CT transformation can be defined as formation (see above) in strata overlying the initial transformation zone. The migration is therefore an upward movement of the transformation relative to the host strata. The basin modelling results suggest that migration directly followed formation of the transformation zone (Figs. 5.1, 5.2). The opal-A/CT transformation zone migrated through most of the Balder Formation and the lower part of Hordaland Group. Migration distance and rate systematically increases from east to west, most likely as a result of more rapid burial due to a westward increase in sediment thickness and accumulation rate (Fig. 5.2). The migration rate was furthermore highest during formation and then systematically decreased until present day. According to our results, negligible migration of the opal-A/CT transformation zone occurred in the last 5 Myrs. Although high sedimentation rates increased burial depth and compaction of underlying sediments, the coeval lowering of surface temperatures during the Pliocene and Pleistocene resulted in no significant temperature increase at the A/CT transformation zone and thus no further upward migration. As such, the migration rate follows the general trend of seafloor temperature. This seems plausible, as seafloor temperature should intuitively be positively correlated to opal-A/CT transformation zone migration.

6.4.2.3. Fossilisation

The fossilisation of the opal-A/CT transformation zone has been previously described as the 'arrest of upward migration' (Davies & Cartwright, 2002). In here, fossilisation is defined as the point when the migration rate becomes zero despite the presence of opal-A in the overlying strata. According to this definition, the opal-A/CT transformation probably started to fossilise in early Miocene time in the North Viking Graben (Figs. 5.1, 5.2). The basin modelling results furthermore suggest that fossilisation occurred earlier in the east than in the west presumably due to a westward increase in sediment thickness (Fig. 5.2). In general, the opal-A/CT transformation zone appears to

have been fossilised close to its current position in the Hordaland Group and fossilisation of the opal-A/CT transformation zone seems to mark the end of a general decrease in migration rate (Fig. 5.2).

6.5. POLYGONAL FAULTING

To investigate the relationship between silica diagenesis and polygonal faulting, the evolution of the polygonal fault system in the Cenozoic succession of the North Viking is analysed in respect to the evolution of the opal-A/CT transformation.

6.5.1. Nucleation

Assuming that the points of maximum displacement on these faults correspond to nucleation sites (sensu Watterson, 1986; Barnett *et al.*, 1987), most faults (or fault segments) nucleated in the lower Hordaland Group (Fig. 4.34f). Polygonal fault nucleation is often identified with sediment failure (e.g. Cartwright & Lonergan, 1996; Goulty, 2001). Sediment failure can, for instance, be predicted from the friction angle (φ) of the host strata as well as the effective horizontal and vertical stress (e.g. Terzaghi, 1996). For the lower Hordaland Group, Wensaas *et al.* (1998) estimate a friction angle of 17° by triaxial testing. The effective vertical stress (σ'_v) can be estimated from the overburden:

$$\sigma'_v = g\,(\rho_s - \rho_w)\,z \qquad (6.1)$$

where g is the gravitational acceleration (9.81 m s^{-2}), p_s is the bulk density of the lower Hordaland Group (c.2000 kg m^{-3}), p_w is the water density (1000 kg m^{-3}) and z is the burial depth (0-1000 m). Assuming no lateral extension (cf. Cartwright & Lonergan, 1996), the effective horizontal stress (σ'_h) can be calculated by:

$$\sigma'_h = K_0\,\sigma'_v \qquad (6.2)$$

where K_0 is the coefficient of earth pressure at rest. The coefficient of earth pressure at rest for normally consolidated clays, such as the lower Hordaland Group (Wensaas *et al.*, 1998), can be calculated from the friction angle (φ) using Jaky's (1948) equation:

$$K_0 \approx 1 - \sin(\varphi) \tag{6.3}$$

where φ is the friction angle. The resulting stresses do not suffice to cause sediment failure in the lower Hordaland Group (Fig. 6.1). Sediment failure would require reduced horizontal stresses:

$$\sigma'_h = K_a \, \sigma'_v \tag{6.4}$$

where K_a is the active earth pressure defined by (Fig. 6.1) (Terzaghi, 1996):

$$K_a = \frac{1 - \sin(\varphi)}{1 + \sin(\varphi)} \tag{6.5}$$

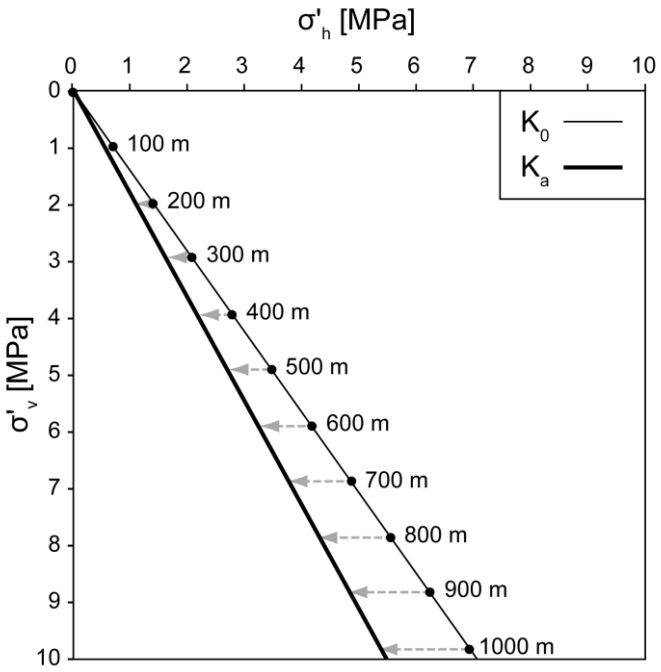


Figure 6.1: Effective horizontal and vertical stress for burial (up to 1000 m) without lateral strain (K_0) and for active earth pressure (K_a) based on Eqs. 7.2-7.4 and Tab. 7.1. Note that without lateral strain sediment failure is not reached during burial.

Cartwright and Lonergan (1996) argue that lateral contraction of the host strata causes the reduction of horizontal stresses to the point of failure. Lateral contraction has in turn been attributed to syneresis and diagenesis (Cartwright & Dewhurst, 1998; Dewhurst *et al.*, 1999; Shin *et al.*, 2008; Cartwright,

2011). Whether sediments of the lower Hordaland Group have undergone syneresis or not is unknown. However, these sediments have most likely undergone silica diagenesis (i.e. opal-A/CT transformation). Whether silica diagenesis can reduce the horizontal stress to the point of sediment failure is also unknown. Experimental studies quantifying the stress reductions during diagenesis in sedimentary rocks are required to decide whether diagenesis can cause sediment failure.

6.5.2. Growth

Polygonal fault growth is interpreted from observed strain and displacement data and related to the opal-A/CT transformation constrained by basin modelling. Cartwright and Lonergan (1996) demonstrate that polygonal faulting requires lateral contraction of the host strata. While distributed strain of the host strata cannot be measured, discrete lateral strain in the polygonal fault system is calculated from faults heaves and bed lengths (Fig. 4.38). Lateral strains <0.05 observed in the upper Hordaland Group provide a lower limit on the lateral strains required for polygonal faulting. Whether these strains can be produced by potential driving mechanisms of polygonal faulting (e.g. syneresis, diagenesis), is unknown. Moreover, lateral strains observed in the lower Hordaland Group are higher (<0.2) than in the upper Hordaland Group (<0.05) (Fig. 4.38). As the transition from upper to lower Hordaland Group coincides with the opal-A/CT transformation, additional lateral strains could have been induced by the transformation.

Polygonal fault growth can also be constrained by displacement data. Displacement-depth profiles show that most faults (64%) have b-type, as opposed to c-type (36%) profiles (Fig. 4.34). Moreover, faults with c-type profiles are often smaller than and antithetic to faults with b-type profiles. These observation probably indicate that faults with c-type profiles formed in response to faults with b-type profiles. To explain polygonal fault growth, it therefore suffices to explain the growth of the primary faults, the ones with b-type displacement-depth profiles. Displacement accumulation on normal faults can be explained by strain softening of the host strata (Fig. 6.2).

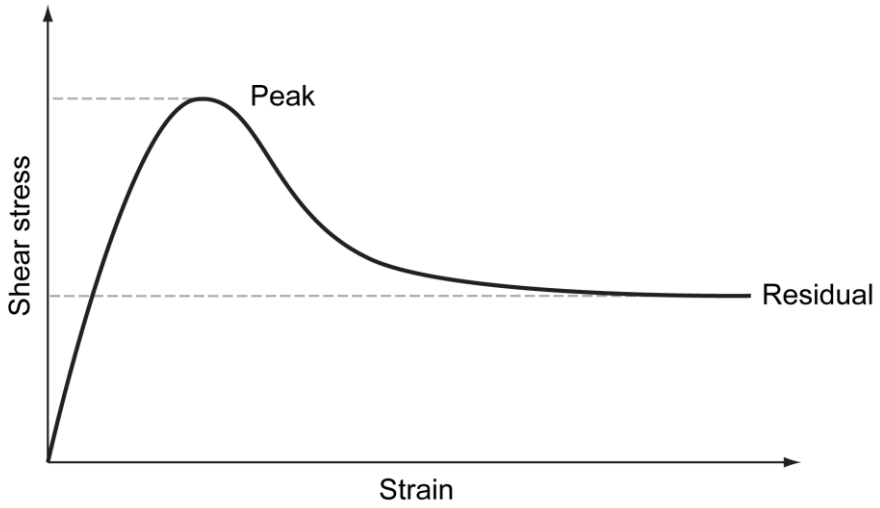


Figure 6.2: Stress-strain curve for sediments, illustrating peak and residual shear strength (after Terzaghi, 1996).

Strain softening describes the decline in shear strength after sediment failure. Strain softening leads to the recurring failure along existing faults, rather than fault nucleation in the surrounding strata. Because the Hordaland Group mudstones exhibit strain softening (Wensaas *et al.*, 1998), it can be used to explain displacement accumulation on the polygonal faults.

The preferential accumulation of displacement in the lower Hordaland Group is however more difficult to explain. As the polygonal faults with b-type profiles are listric (Fig. 4.35b), decreasing fault dip may result in increasing fault heave which results in increasing displacement given that the fault heave is higher than the throw (Fig. 4.34). Based on the observed fault throw and geometry, one would expect to see a continuous heave and displacement increase with depth. The observed displacement data however show an abrupt displacement increase from <50 m at 300 m to >100 at 600 m depth (Fig. 4.26). As this abrupt displacement increase coincides with the opal-A/CT transformation, additional strain could have been induced by silica diagenesis and may therefore explain preferential displacement accumulation in the lower Hordaland Group.

At last, it is worth discussing polygonal fault propagation into the upper Hordaland Group inferred from displacement-depth profiles and contours (Figs. 4.26, 4.27). While displacement maxima in the lower Hordaland Group indicate nucleation sites; low displacement gradients (<1) and fault-propagation folds are typical for unrestricted, upward fault propagation. Although silica

diagenesis did not reach the upper Hordaland Group, water release during opal-A/CT transformation may have driven upward fault propagation.

7. ADVANCES & IMPLICATIONS

7.1. SILICA DIAGENESIS

Although previous studies mention silica diagenesis in the northern North Sea (Rundberg, 1989; Thyberg *et al.*, 1999; Rundberg & Eidvin, 2005), this is the first study to document the opal-A/CT transformation as well as the absence of the opal-CT/Q transformation in the Cenozoic rocks of the North Viking Graben. As such, it forms part of an effort to map silica transformations along the Northeast Atlantic margin (Fig. 7.1).

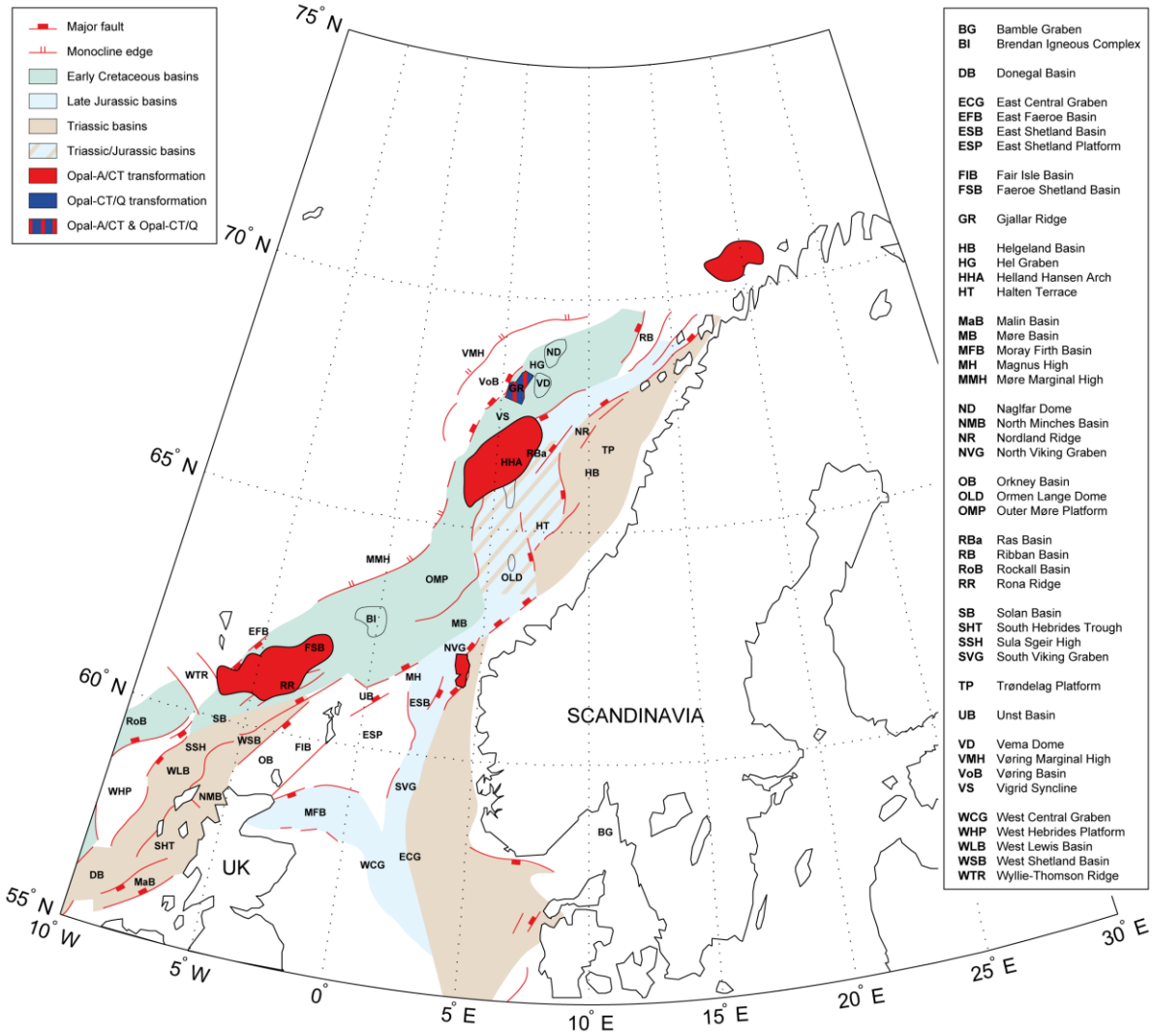


Figure 7.1: Structural map of the Northeast Atlantic margin after Graham *et al.* (2003) showing the extent of documented opal-A/CT transformations in the North Viking Graben (Rundberg, 1989; Thyberg *et al.*, 1999; Rundberg & Eidvin, 2005; this study), Faeroe-Shetland Basin (Davies & Cartwright, 2002; Davies, 2005), Møre Basin (Brekke *et al.*, 1999; Brekke, 2000; Davies & Cartwright, 2007; Neagu *et al.*, 2010), Vøring Basin (Brekke *et al.*, 1999; Brekke, 2000; Berndt *et al.*, 2004; Davies & Cartwright, 2007; Neagu *et al.*, 2010) and the Barents Sea (Riis & Fjeldskaar, 1992), Gjallar Ridge (Ireland *et al.*, 2011) and of opal-CT/Q transformation in the Gjallar Ridge (Ireland *et al.*, 2011).

7.2. BASIN MODELLING

Previous studies primarily use observations from seismic reflection data to constrain the evolution of silica transformations on a basin-scale (Davies & Cartwright, 2002; Neagu *et al.*, 2010). These studies often support their interpretation by comparing transformation temperatures to estimated subsurface temperature. This approach is problematic because silica diagenesis depends on time as well as temperature and subsurface temperatures are often estimated. This is the first study highlighting that the spatial and temporal evolution of silica diagenesis can be simulated in a basin model. Because this approach allows an accurate calculation of subsurface temperature, opal-A/CT transformation rates can be calculated based on time and temperature. This approach allows the effect of sedimentation, seafloor temperature, and heat flow on silica diagenesis to be studied on a basin-scale. As such, it represents a significant advance over previous studies and in future may help us understand the evolution of complex silica transformation zones (e.g. Davies, 2005; Meadows & Davies, 2007).

7.3. ROCK PHYSICS

Previous studies either compare rock properties of opal-A, opal-CT and quartz bearing rocks (Isaacs, 1981; Tada & Iijima, 1983; Guerin & Goldberg, 1996; Kim *et al.*, 2007) or analyse rock property changes with opal-A, opal-CT and quartz content (Compton, 1991; Chaika & Dvorkin, 2000) to infer the impact of silica diagenesis on the rock properties. These approaches are problematic because they do not account for depth-dependent rock property changes and rock property changes due to variations in the overall mineralogy, in particular in clay minerals. To address these problems, multiple linear regression analysis is, for the first time, applied to model the compositional and depth dependency of porosity for exploration well 35/10-1 and 35/11-5. The analysis shows that opal-A content explains host rock porosity to a large extent and opal-CT and pyrite content explain host rock porosity to a lesser degree. The analysis is validated by demonstrating that the assumptions underlying multiple regression are fulfilled. As such, this study does not only confirm that the impact of opal-A

on the host rock porosity is statistical significant, but also provides a recipe to analyse the impact of multiple parameters on host rock properties.

7.4. WATER RELEASE

Previous studies show that the transformation from opal-A to opal-CT can release up to 14wt% water (see Section 2.2.2.). Considering that the rocks hosting the transformation consist to less than 15vol% of opal-CT (Figs. 4.7, 4.8), the water released is less than 0.02% of the host rock volume. This volume is small compared to the amount of water released as a result of the porosity reduction. The opal-A/CT transformation reduces host rock porosity by *c.*20% which, assuming these rocks are water-saturated, results in an equivalent water release. This water release may cause overpressure, hydraulic fractures, or sediment remobilisations (Davies *et al.*, 2006). Its capacity to transport significant amounts of silica out of the system may however be limited. Bjorlykke and Jahren (2012), for example, argue that silica transport is limited by a number of factors, in particular silica solubility and host rock permeability. According to their interpretation, only a minute fraction (10^{-5}) of silica in the solid phase can be dissolved in the pore water, limiting silica transport out of the system.

7.5. POLYGONAL FAULTING

Previous studies suggest silica diagenesis to drive polygonal faulting, as some of these faults seem to nucleate close to diagenetic boundaries (Cartwright, 2011; Davies & Ireland, 2011). In this study, the evolution of silica diagenesis and the polygonal fault system are constrained separately by basin modelling and fault analysis, respectively. While basin modelling highlights the formation, migration and fossilisation of the opal-A/CT transformation zone, fault analysis is used to constrain polygonal fault nucleation and growth. Although the polygonal faults nucleated and preferentially

grew in rocks which have most likely undergone opal-A/CT transformation, basic rock mechanics show that diagenesis would need to induce lateral stresses and strains in the host rock to cause polygonal fault nucleation and growth, respectively. As such, this study highlights a need for experimental studies quantifying stresses/strains in sedimentary rocks induced by diagenesis and case studies reconstructing polygonal fault growth in sedimentary basins worldwide.

8. APPENDIX

8.1. ENERGY DISPERSIVE SPECTRA

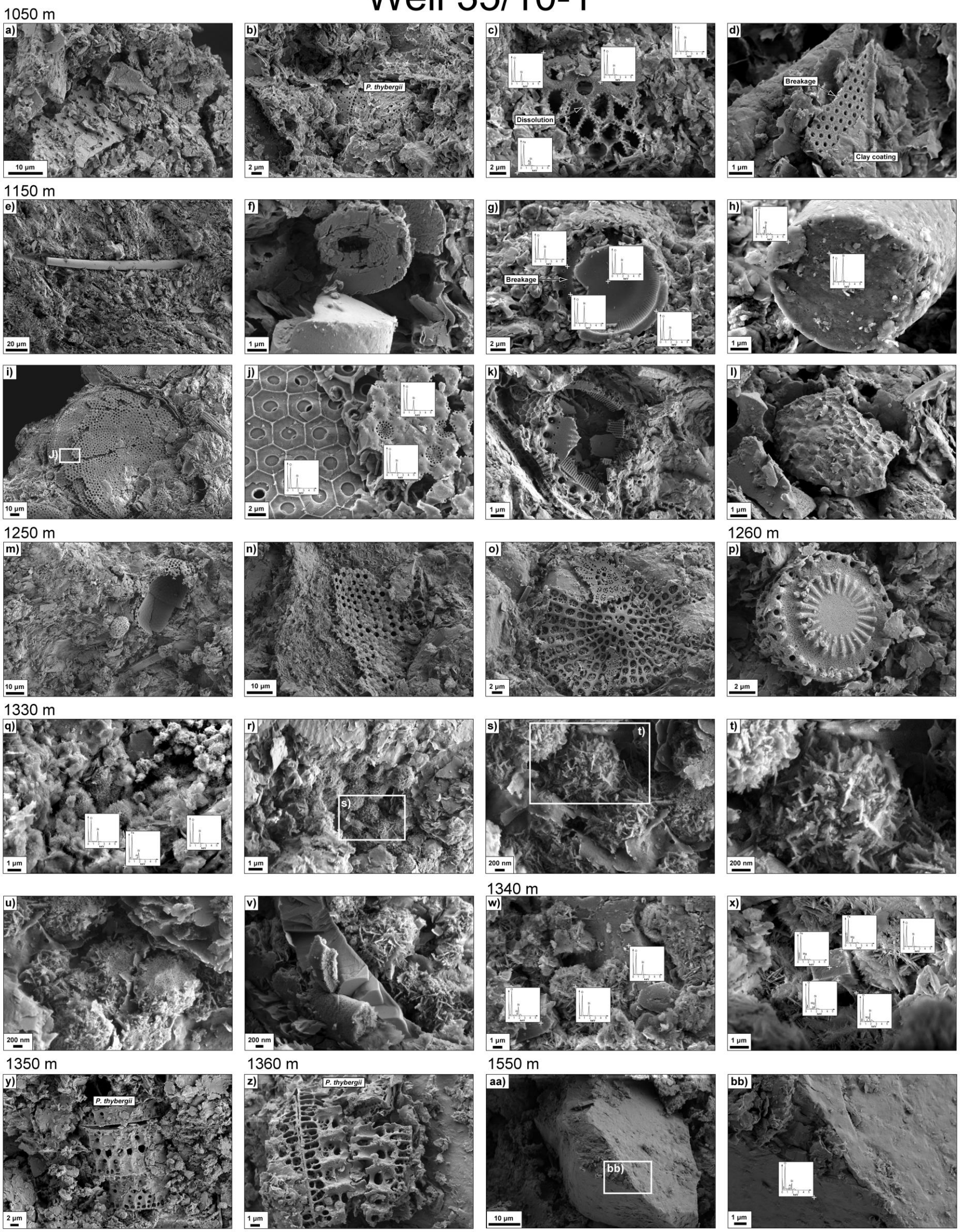


Figure 8.1: Scanning electron microscopy images of cutting samples from exploration well 35/10-1 with energy dispersive X-ray diffractograms.

8.2. MINERALOGICAL AND WIRELINE DATA

Depth	Opal-A	Opal-CT	Quartz	Illite-smectite	Illite	Kaolinite	Calcite	Pyrite	Barite	Sylvite	Halite	Porosity
m	vol.%	vol.%	vol.%	vol.%	vol.%	vol.%	vol.%	vol.%	vol.%	vol.%	vol.%	%
900	0.00	0.00	13.72	78.04	0.93	0.00	0.00	3.52	1.99	0.68	1.12	24.42
910	0.00	0.00	11.29	80.27	0.46	0.00	0.00	6.16	1.09	0.31	0.43	23.47
920	13.92	0.00	19.06	61.78	0.28	1.07	0.00	3.08	0.54	0.07	0.19	40.62
930	20.19	1.08	22.68	38.49	10.31	1.13	0.00	2.32	3.68	0.03	0.08	44.89
940	16.70	1.38	12.58	40.75	18.49	6.82	0.00	1.92	1.01	0.30	0.04	45.58
950	23.66	1.57	22.81	37.73	9.81	0.77	0.00	2.32	0.93	0.14	0.26	46.01
960	27.00	2.18	24.17	39.36	3.63	0.82	0.00	1.82	0.84	0.17	0.00	49.21
970	25.28	0.00	24.49	38.66	7.52	1.15	0.00	1.45	1.07	0.36	0.02	51.60
980	24.23	0.00	18.74	43.30	9.66	0.85	0.00	1.25	1.34	0.57	0.05	53.93
990	23.15	0.00	21.84	49.26	2.71	0.77	0.00	0.57	0.78	0.51	0.42	52.26
1000	20.55	0.00	17.10	58.17	0.83	0.05	0.00	0.41	0.88	0.75	1.26	55.10
1010	25.35	0.00	16.06	41.11	10.94	1.69	0.00	1.12	1.49	0.59	1.63	57.06
1020	21.90	0.00	18.77	41.37	12.02	0.86	0.00	1.88	1.58	0.55	1.06	53.91
1030	19.46	0.00	20.99	45.10	8.06	1.87	0.00	1.25	1.90	0.56	0.80	55.37
1040	31.26	0.00	6.56	42.26	15.99	1.19	0.01	1.48	0.33	0.74	0.18	58.44
1050	30.24	0.00	8.00	37.02	17.65	2.56	0.00	1.93	1.94	0.46	0.19	57.93
1060	26.82	0.00	11.54	54.02	3.02	1.82	0.18	0.13	1.52	0.79	0.14	58.65
1070	27.19	0.00	16.27	32.70	15.95	2.62	0.01	2.14	1.21	0.46	1.45	58.84
1080	31.76	0.00	9.03	44.26	10.75	0.75	0.01	0.27	0.79	0.62	1.77	55.13
1090	25.92	0.00	15.76	31.15	19.78	2.31	0.62	2.07	2.17	0.14	0.09	55.52
1100	23.64	0.00	14.12	43.49	11.35	0.95	1.59	0.47	1.43	0.85	2.10	56.71
1110	26.04	0.00	17.30	32.25	16.89	2.79	0.92	1.72	1.22	0.43	0.45	54.66
1120	24.37	0.00	11.00	44.59	13.39	1.92	0.81	0.37	1.68	0.78	1.08	52.12
1130	22.58	0.00	15.21	39.33	15.78	1.64	0.44	0.94	2.95	0.63	0.49	56.51
1140	19.18	0.00	14.45	55.39	4.64	1.44	0.85	0.37	2.32	0.72	0.63	56.28
1150	17.97	0.00	18.57	38.90	20.70	2.40	0.37	0.65	0.00	0.41	0.04	52.70
1160	18.25	0.00	14.11	33.75	28.04	2.51	1.26	1.50	0.05	0.49	0.04	53.53
1170	18.66	0.00	13.29	48.60	16.52	0.96	0.86	0.24	0.18	0.47	0.22	53.12
1180	18.71	0.00	11.74	43.26	19.23	0.59	1.13	0.81	2.19	0.59	1.74	50.26
1190	14.83	0.00	15.80	43.75	18.72	0.63	1.22	0.41	2.78	0.67	1.19	48.05
1200	17.05	0.00	16.03	36.95	25.63	0.59	0.40	1.05	1.87	0.33	0.09	39.40
1210	17.15	0.00	12.74	47.33	17.56	0.96	0.60	0.06	1.08	0.57	1.94	36.89
1220	13.27	0.00	19.75	40.09	22.29	0.27	0.94	0.65	2.26	0.34	0.13	35.59
1230	28.35	0.00	7.63	53.85	8.39	0.58	0.13	0.00	0.00	0.76	0.31	38.71
1240	11.08	1.06	21.20	51.86	11.03	0.43	0.74	0.41	1.47	0.58	0.12	38.48
1260	8.42	2.34	16.52	51.27	15.44	1.11	0.30	1.07	1.85	0.56	1.13	41.67
1270	9.51	8.17	20.84	44.34	13.20	0.34	0.00	0.48	1.62	0.66	0.85	43.75
1280	7.42	3.13	21.92	45.90	15.81	1.25	0.08	1.34	2.84	0.21	0.11	44.28
1290	10.33	4.62	14.95	53.61	10.11	1.65	0.17	0.28	2.17	0.76	1.36	48.08
1300	6.13	4.73	17.26	52.66	14.02	1.55	0.10	0.73	2.26	0.30	0.27	41.25
1310	10.36	3.87	15.46	55.94	8.44	1.42	0.95	0.03	1.79	0.89	0.86	45.48
1320	5.94	5.08	8.95	61.42	11.74	1.28	0.67	0.06	2.98	0.52	1.36	43.67
1330	9.00	7.02	11.93	55.74	12.69	0.50	1.30	0.06	1.01	0.54	0.23	47.06
1340	9.62	9.26	11.46	50.95	12.53	2.37	0.42	0.65	1.64	0.66	0.45	44.53
1350	5.82	14.97	11.08	43.19	18.87	2.81	0.14	0.95	0.67	0.42	1.06	47.13
1360	9.76	8.27	8.94	54.63	12.36	2.13	0.46	0.11	1.85	0.83	0.66	48.74
1370	7.73	7.57	11.50	51.46	14.85	2.40	0.33	0.88	2.58	0.53	0.16	39.13
1380	9.87	7.24	8.68	57.24	12.87	1.86	0.26	0.25	0.80	0.70	0.24	44.03
1390	7.60	5.23	13.92	52.40	10.51	2.46	1.03	1.33	4.14	0.50	0.87	41.01
1400	8.39	14.04	9.98	52.67	11.63	0.80	1.09	0.12	0.27	0.61	0.40	39.02
1410	5.25	1.88	8.53	58.49	18.39	2.79	0.02	1.09	2.80	0.47	0.27	33.59
1420	7.91	0.00	15.57	56.43	10.87	3.65	1.30	1.02	2.05	0.52	0.70	34.28
1430	6.97	0.00	12.00	62.05	14.99	2.58	0.00	0.02	0.59	0.51	0.28	36.61
1440	2.98	1.63	8.83	68.40	13.62	2.28	0.09	0.19	1.38	0.38	0.24	38.92
1450	10.17	0.66	8.70	57.07	18.09	2.23	0.06	0.31	0.36	0.55	1.80	43.09
1460	2.23	1.85	10.06	60.45	18.30	2.59	0.22	2.27	1.82	0.17	0.04	43.15
1470	5.19	0.00	10.50	65.91	13.55	2.45	0.00	0.87	0.96	0.45	0.13	37.79
1480	3.94	9.46	15.54	46.52	19.88	3.17	0.00	0.26	0.01	0.34	0.87	40.77
1490	5.58	1.68	18.86	55.95	14.23	2.55	0.00	0.31	0.01	0.40	0.43	42.67
1500	6.78	0.00	9.89	63.00	15.75	1.77	0.00	1.43	0.01	0.58	0.79	39.56
1510	0.00	0.19	17.64	64.81	7.16	1.92	0.00	6.46	0.01	0.00	1.82	41.94
1520	0.00	0.00	15.90	71.55	5.74	0.00	0.00	5.04	0.01	0.00	1.76	36.19
1530	0.00	0.39	18.06	68.22	6.99	0.00	0.00	5.77	0.09	0.00	0.47	35.81
1540	0.00	0.78	19.21	67.15	6.77	0.00	0.00	4.04	1.07	0.05	0.94	37.30
1550	0.00	1.38	19.05	63.06	6.87	0.00	0.00	5.93	3.20	0.01	0.51	35.73
1560	0.00	0.19	19.56	73.59	2.01	0.00	0.00	3.47	0.18	0.01	1.00	40.33

1570	0.00	1.26	17.31	66.62	5.11	0.00	0.10	7.58	1.99	0.00	0.03	38.47
1580	0.00	0.00	21.38	73.12	0.00	0.00	0.07	4.80	0.61	0.00	0.02	38.11
1590	0.00	0.06	21.20	66.59	1.21	0.00	0.01	8.71	2.16	0.01	0.05	37.68
1600	0.00	0.03	13.24	81.01	0.00	0.00	0.01	5.17	0.50	0.00	0.03	39.45
1610	0.00	0.04	15.49	79.01	0.00	0.00	0.00	5.46	0.00	0.00	0.00	38.75
1620	0.00	1.22	17.27	68.66	2.22	0.00	0.01	6.80	2.41	0.00	1.41	37.31
1630	0.00	1.62	18.22	68.97	1.65	0.00	0.01	7.44	1.85	0.00	0.24	35.41
1640	0.00	0.00	18.93	72.91	0.00	0.00	0.01	6.55	0.48	0.00	1.12	33.58
1650	0.00	0.53	24.75	63.07	0.00	0.00	0.01	9.11	2.53	0.00	0.00	36.01
1660	0.00	0.45	17.58	75.04	0.00	0.00	0.01	5.22	0.89	0.00	0.79	37.29
1670	0.00	0.48	18.08	73.68	0.00	0.00	0.01	7.00	0.74	0.00	0.00	36.81
1680	0.00	0.49	16.25	76.19	0.00	0.00	0.01	6.41	0.41	0.00	0.25	36.51
1690	0.00	0.08	15.50	72.74	0.00	0.00	0.01	9.78	1.23	0.00	0.65	36.00
1700	0.00	0.08	16.74	71.48	0.00	0.00	0.01	10.24	1.38	0.00	0.08	35.58
1710	0.00	0.07	16.80	73.01	0.00	0.00	0.01	8.77	1.26	0.00	0.07	35.01
1720	0.00	0.07	12.67	79.00	0.00	0.00	0.01	7.61	0.55	0.00	0.08	31.47
1730	0.00	0.08	21.04	66.28	0.00	0.00	0.01	11.52	1.07	0.00	0.00	27.58
1740	0.00	0.05	13.55	77.53	0.00	0.00	0.01	8.05	0.28	0.00	0.53	31.16
1750	0.00	0.06	16.92	71.05	0.00	0.00	0.01	11.22	0.35	0.00	0.39	28.01
1760	0.00	0.05	21.02	70.75	0.00	0.00	0.01	7.82	0.36	0.00	0.00	27.80
1790	0.00	0.05	27.90	56.32	0.00	0.00	0.01	14.03	0.57	0.00	1.12	27.28

Table 8.1: Mineral contents, porosity and p-wave velocity data of exploration well 35/10-1 used in multiple linear regression analysis.

Depth	Opal-A	Opal-CT	Quartz	Illite-smectite	Illite	Kaolinite	Calcite	Pyrite	Barite	Sylvite	Halite	Porosity
m	vol.%	vol.%	vol.%	vol.%	vol.%	vol.%	vol.%	vol.%	vol.%	vol.%	vol.%	vol.%
1030	28.00	0.45	10.57	48.03	1.66	1.80	1.47	1.34	3.34	2.84	0.50	53.68
1040	28.22	0.00	14.59	46.74	6.31	1.41	1.87	0.13	0.38	0.29	0.06	52.44
1050	19.44	0.00	20.25	47.72	8.99	1.16	0.43	0.08	0.87	0.79	0.28	55.31
1060	24.82	0.00	12.63	41.84	17.41	2.26	0.16	0.05	0.00	0.78	0.04	52.94
1070	18.72	0.00	24.57	30.86	19.17	3.16	0.21	1.53	0.10	1.57	0.12	52.36
1080	20.67	0.00	11.65	41.06	20.08	1.00	1.67	0.98	0.57	2.10	0.23	50.81
1090	20.70	0.79	12.24	38.65	19.96	2.61	1.23	1.57	0.30	1.83	0.13	47.00
1100	22.31	0.00	13.11	46.50	12.98	1.08	1.72	0.00	1.10	0.98	0.22	44.32
1110	12.27	0.00	19.21	41.81	16.43	2.10	2.47	0.41	3.60	1.46	0.23	45.92
1120	17.17	0.00	17.00	46.03	12.60	1.71	1.30	0.00	2.74	1.17	0.27	46.60
1130	15.06	0.00	26.69	36.58	11.26	2.84	0.37	1.49	3.43	2.09	0.18	48.71
1140	17.93	0.00	21.66	47.35	9.57	1.71	0.10	0.09	0.48	0.91	0.19	47.98
1150	16.28	0.00	17.65	46.06	10.77	3.61	0.22	1.02	1.40	2.84	0.16	47.87
1160	17.31	0.00	17.70	53.31	7.95	2.10	0.09	0.00	0.49	0.84	0.21	40.17
1170	11.88	0.00	29.82	43.49	9.28	2.28	0.13	0.41	1.69	0.74	0.26	36.90
1180	6.52	1.32	31.09	38.52	13.13	2.95	0.17	1.64	2.04	2.37	0.25	40.27
1190	9.96	1.88	16.64	53.02	12.19	3.98	0.27	0.00	1.01	0.88	0.17	40.84
1200	2.87	3.38	20.54	50.13	15.94	2.44	0.00	1.27	1.06	2.13	0.23	41.26
1210	5.31	2.30	20.62	52.64	12.01	2.26	0.00	1.08	2.40	1.04	0.33	36.87
1220	5.40	6.08	12.39	53.19	14.84	1.97	0.00	0.86	3.20	1.78	0.27	38.43
1230	7.10	13.00	13.92	42.87	18.19	2.27	0.00	1.74	0.37	0.45	0.09	37.89
1240	4.07	13.84	12.31	51.73	10.49	1.42	0.01	2.28	1.53	2.28	0.04	38.20
1250	9.77	6.58	11.80	53.58	14.48	1.51	0.01	0.01	1.05	0.99	0.23	41.31
1260	0.00	7.83	31.38	47.32	8.35	1.45	0.01	0.01	2.34	1.17	0.13	46.71
1270	0.00	8.87	13.64	63.62	8.79	2.56	0.10	1.94	0.22	0.10	0.15	45.80
1280	0.00	9.05	12.66	60.28	16.21	1.44	0.13	0.00	0.00	0.16	0.09	46.30
1290	0.00	1.03	17.20	61.49	14.80	2.53	0.23	0.60	0.82	0.88	0.43	44.76
1300	2.71	1.16	13.18	56.15	18.19	2.43	0.02	1.42	2.52	0.97	1.24	52.35
1310	9.96	0.43	13.25	57.52	9.34	1.68	0.02	2.15	4.48	1.06	0.11	48.84
1320	5.32	0.42	12.98	63.26	12.45	2.63	0.02	0.19	1.66	0.95	0.12	45.15
1330	2.17	0.93	6.41	55.73	23.34	9.06	0.01	1.56	0.27	0.52	0.00	42.48
1340	3.13	0.29	14.06	58.50	17.72	2.61	0.01	0.90	1.57	1.06	0.15	40.99
1350	0.00	0.51	18.48	50.24	16.32	3.75	0.02	3.77	3.44	3.43	0.04	48.47
1360	2.89	0.65	10.68	67.41	12.13	1.68	0.00	1.15	1.81	1.06	0.55	45.56
1370	0.01	0.95	13.90	77.30	0.00	0.00	0.00	5.31	0.95	0.00	1.57	45.56
1380	0.04	1.23	12.18	64.85	13.27	2.42	0.19	1.08	2.91	1.67	0.19	43.73
1390	3.28	0.50	11.74	68.93	11.39	1.23	0.15	0.31	0.92	0.93	0.62	43.64
1400	1.73	0.00	12.19	70.64	10.16	2.14	0.03	2.26	0.06	0.36	0.42	41.28
1410	4.65	0.00	9.14	72.32	13.05	0.08	0.00	0.19	0.00	0.31	0.26	41.64
1420	1.67	0.00	12.85	66.79	15.73	0.11	0.00	0.85	0.61	1.19	0.19	38.92
1430	2.49	0.63	11.41	61.23	18.78	2.22	0.00	2.37	0.22	0.59	0.05	39.56
1440	1.71	0.00	9.70	70.87	12.50	0.18	0.00	1.41	1.08	1.17	1.37	45.93
1450	5.29	0.00	7.18	75.17	8.41	0.00	0.19	0.62	1.33	1.36	0.46	45.02
1460	0.00	1.84	12.16	58.03	21.56	0.41	0.00	5.62	0.14	0.00	0.25	46.73
1470	0.16	0.05	9.44	70.68	17.17	0.00	0.72	0.00	0.66	0.97	0.15	44.94
1480	0.00	0.88	9.09	71.12	15.92	0.00	0.00	0.00	1.24	1.22	0.53	42.60

1490	3.07	0.00	6.81	80.84	6.04	0.00	0.00	0.01	1.86	0.86	0.52	47.04
1500	0.00	0.00	5.21	78.81	15.79	0.00	0.00	0.00	0.00	0.18	0.00	43.42

Table 8.2: Mineral contents, porosity and p-wave velocity data of exploration well 35/11-5 used in multiple linear regression analysis.

8.3. R CODES

```
library(xlsx)

mydata <- read.xlsx("35-10-1.xlsx", 1)


library(leaps)

attach(mydata)

leaps<-
regsubsets(POR~Depth+Illite.Smectite+Illite+Kaolinite+Opal.A+Opal
.CT+Quartz+Calcite+Pyrite+Barite+Sylvite+Halite,data=mydata,nbest
=10,method='exhaustive')


summary(leaps)
```

Code 8.1: Example code used for all subsets model selection

```
library(xlsx)

mydata <- read.xlsx("35-10-1.xlsx", 1)

attach(mydata)


library(car)

fit1 <- lm(POR ~ Opal.A + Opal.CT)

summary(fit1)

vif(fit1)

fit1.scale <- lm(scale(POR) ~ scale(Opal.A) + scale(Opal.CT))

summary(fit1.scale)


plot(fit1)

plot(fit1$residuals ~ Opal.A)

qqPlot(fit1)
```

Code 8.2: Example code used for multiple regression

9. REFERENCES

ADDIS, M.A. & JONES, M.E. (1985) Volume Changes During Diagenesis. *Marine and petroleum geology*, **2,** 241-246.

ALLEN, P.A. & ALLEN, J.R. (2013) *Basin Analysis: Principles and Application to Petroleum Play Assessment*. John Wiley & Sons.

ANDERSON, E. (1951) The Dynamics of Faulting and Dyke Formation with Application to Britain (2nd Edn) Oliver and Boyd, Edinburgh.

ANDERSON, T.F., POPP, B.N., WILLIAMS, A.C., HO, L.-Z. & HUDSON, J.D. (1994) The Stable Isotopic Records of Fossils from the Peterborough Member, Oxford Clay Formation (Jurassic), Uk: Palaeoenvironmental Implications. *Journal of the Geological Society*, **151,** 125-138.

ANELL, I., THYBO, H. & RASMUSSEN, E. (2012) A Synthesis of Cenozoic Sedimentation in the North Sea. *Basin Research*, **24,** 154-179.

ARRHENIUS, S. (1889) Über Die Reaktionsgeschwindigkeit Bei Der Inversion Von Rohrzucker Durch Säuren. *Zeitschrift für physikalische Chemie*, **4,** 226-248.

BADLEY, M.E., PRICE, J.D., RAMBECH DAHL, C. & AGDESTEIN, T. (1988) The Structural Evolution of the Northern Viking Graben and Its Bearing Upon Extensional Modes of Basin Formation. *Journal of the Geological Society*, **145,** 455-472.

BAHORICH, M. & FARMER, S. (1995) 3-D Seismic Discontinuity for Faults and Stratigraphic Features: The Coherence Cube. *The leading edge*, **14,** 1053-1058.

BARNETT, J.A.M., MORTIMER, J., RIPPON, J.H., WALSH, J.J. & WATTERSON, J. (1987) Displacement Geometry in the Volume Containing a Single Normal-Fault. *Aapg Bulletin-American Association of Petroleum Geologists*, **71,** 925-937.

BATCHELDER, M. & CRESSEY, G. (1998) Rapid, Accurate Phase Quantification of Clay-Bearing Samples Using a Position-Sensitive X-Ray Detector. *Clays and Clay Minerals*, **46,** 183-194.

BEHL, R.J. (2011) Chert Spheroids of the Monterey Formation, California (USA): Early-Diagenetic Structures of Bedded Siliceous Deposits. *Sedimentology*, **58,** 325-351.

BERNDT, C., BUNZ, S., CLAYTON, T., MIENERT, J. & SAUNDERS, M. (2004) Seismic Character of Bottom Simulating Reflectors: Examples from the Mid-Norwegian Margin. *Marine and Petroleum Geology*, **21,** 723-733.

BJORLYKKE, K. & JAHREN, J. (2012) Open or Closed Geochemical Systems During Diagenesis in Sedimentary Basins: Constraints on Mass Transfer During Diagenesis and the Prediction of Porosity in Sandstone and Carbonate Reservoirs. *AAPG bulletin*, **96,** 2193-2214.

BJØRLYKKE, K. (1999) Principal Aspects of Compaction and Fluid Flow in Mudstones. *Geological Society, London, Special Publications*, **158,** 73-78.

BJØRLYKKE, K. (2014) Relationships between Depositional Environments, Burial History and Rock Properties. Some Principal Aspects of Diagenetic Process in Sedimentary Basins. *Sedimentary Geology*, **301,** 1-14.

BOHRMANN, G., SPIEß, V., HINZE, H. & KUHN, G. (1992) Reflector "Pc" a Prominent Feature in the Maud Rise Sediment Sequence (Eastern Weddell Sea): Occurrence, Regional Distribution and Implications to Silica Diagenesis. *Marine geology*, **106,** 69-87.

BREKKE, H., DAHLGREN, S., NYLAND, B. & MAGNUS, C. (1999) The Prospectivity of the Vøring and Møre Basins on the Norwegian Sea Continental Margin. *Geological Society, London, Petroleum Geology Conference series*, **5,** 261-274.

BREKKE, H. (2000) The Tectonic Evolution of the Norwegian Sea Continental Margin with Emphasis on the Vøring and Møre Basins. *Geological Society, London, Special Publications*, **167,** 327-378.

BROWN, G., BRINDLEY, G. & BROWN, G. (1980) Crystal Structures of Clay Minerals and Their X-Ray Identification. *Mineralogical Society, London***,** 361-410.

BUCHARDT, B. (1978) Oxygen Isotope Palaeotemperatures from the Tertiary Period in the North Sea Area.

CARTWRIGHT, J. (2011) Diagenetically Induced Shear Failure of Fine-Grained Sediments and the Development of Polygonal Fault Systems. *Marine and Petroleum Geology*, **28,** 1593-1610.

CARTWRIGHT, J.A. & LONERGAN, L. (1996) Volumetric Contraction During the Compaction of Mudrocks: A Mechanism for the Development of Regional-Scale Polygonal Fault Systems. *Basin Research*, **8,** 183-193.
CARTWRIGHT, J.A. & DEWHURST, D.N. (1998) Layer-Bound Compaction Faults in Fine-Grained Sediments. *Geological Society of America Bulletin*, **110,** 1242-1257.
CHAIKA, C. & DVORKIN, J. (2000) Porosity Reduction During Diagenesis of Diatomaceous Rocks. *Aapg Bulletin-American Association of Petroleum Geologists*, **84,** 1173-1184.
CLAUSEN, J., GABRIELSEN, R., REKSNES, P. & NYSAETHER, E. (1999) Development of Intraformational (Oligocene–Miocene) Faults in the Northern North Sea: Influence of Remote Stresses and Doming of Fennoscandia. *Journal of Structural Geology*, **21,** 1457-1475.
COMPTON, J.S. (1991) Porosity Reduction and Burial History of Siliceous Rocks from the Monterey and Sisquoc Formations, Point-Pedernales Area, California. *Geological Society of America Bulletin*, **103,** 625-636.
CONLEY, D.J. (1998) An Interlaboratory Comparison for the Measurement of Biogenic Silica in Sediments. *Marine chemistry*, **63,** 39-48.
CRESSEY, G. & SCHOFIELD, P. (1996) Rapid Whole-Pattern Profile-Stripping Method for the Quantification of Multiphase Samples. *Powder Diffraction*, **11,** 35-39.
DAVIES, R., IRELAND, M. & CARTWRIGHT, J. (2009) Differential Compaction Due to the Irregular Topology of a Diagenetic Reaction Boundary: A New Mechanism for the Formation of Polygonal Faults. *Basin Research*, **21,** 354-359.
DAVIES, R.J. & CARTWRIGHT, J. (2002) A Fossilized Opal a to Opal C/T Transformation on the Northeast Atlantic Margin: Support for a Significantly Elevated Palaeogeothermal Gradient During the Neogene? *Basin Research*, **14,** 467-486.
DAVIES, R.J. (2005) Differential Compaction and Subsidence in Sedimentary Basins Due to Silica Diagenesis: A Case Study. *Geological Society of America Bulletin*, **117,** 1146-1155.
DAVIES, R.J. & CLARK, I.R. (2006) Submarine Slope Failure Primed and Triggered by Silica and Its Diagenesis. *Basin Research*, **18,** 339-350.
DAVIES, R.J., HUUSE, M., HIRST, P., CARTWRIGHT, J. & YANG, Y.S. (2006) Giant Clastic Intrusions Primed by Silica Diagenesis. *Geology*, **34,** 917-920.
DAVIES, R.J. & CARTWRIGHT, J.A. (2007) Kilometer-Scale Chemical Reaction Boundary Patterns and Deformation in Sedimentary Rocks. *Earth and Planetary Science Letters*, **262,** 125-137.
DAVIES, R.J., GOULTY, N.R. & MEADOWS, D. (2008) Fluid Flow Due to the Advance of Basin-Scale Silica Reaction Zones. *Geological Society of America Bulletin*, **120,** 195-206.
DAVIES, R.J. & IRELAND, M.T. (2011) Initiation and Propagation of Polygonal Fault Arrays by Thermally Triggered Volume Reduction Reactions in Siliceous Sediment. *Marine Geology*, **289,** 150-158.
DEER, W.A., HOWIE, R.A., WISE, W.S. & ZUSSMAN, J. (2004) *Rock-Forming Minerals. Volume 4b: Framework Silicates: Silica Minerals, Feldspathoids and the Zeolites*. Geological Society, Geological Society Publishing House.
DEMASTER, D. (2003) The Diagenesis of Biogenic Silica: Chemical Transformations Occurring in the Water Column, Seabed, and Crust. *Treatise on Geochemistry*, **7,** 87-98.
DEMASTER, D.J. (2002) The Accumulation and Cycling of Biogenic Silica in the Southern Ocean: Revisiting the Marine Silica Budget. *Deep Sea Research Part II: Topical Studies in Oceanography*, **49,** 3155-3167.
DEWHURST, D.N., CARTWRIGHT, J.A. & LONERGAN, L. (1999) The Development of Polygonal Fault Systems by Syneresis of Colloidal Sediments. *Marine and Petroleum Geology*, **16,** 793-810.
DOVE, P.M. & RIMSTIDT, J.D. (1994) Silica-Water Interactions. *Silica: Physical Behavior, Geochemistry and Materials Applications*, **29,** 259-&.
DRALUS, D., PETERS, K.E., LEWAN, M.D., SCHENK, O., HERRON, M. & TSUCHIDA, K. (2011) Kinetics of the Opal-Ct to Quartz Phase Transition Control Diagenetic Traps in Siliceous Shale Source Rock from the San Joaquin Basin and Hokkaido. *Oral presentation at AAPG Annual Convention and Exhibition, Houston, Texas, USA, April 10-13, 2011*, **Search and Discovery Article #40771**.
DUFFY, C.J. (1993) Kinetics of Silica-Phase Transitions, Los Alamos National Lab., NM (United States).

EIDVIN, T. & RUNDBERG, Y. (2001) Late Cainozoic Stratigraphy of the Tampen Area (Snorre and Visund Fields) in the Northern North Sea, with Emphasis on the Chronology of Early Neogene Sands. *Norwegian Journal of Geology/Norsk Geologisk Forening*, **81**.

EIDVIN, T., RIIS, F. & RASMUSSEN, E.S. (2014) Oligocene to Lower Pliocene Deposits of the Norwegian Continental Shelf, Norwegian Sea, Svalbard, Denmark and Their Relation to the Uplift of Fennoscandia: A Synthesis. *Marine and Petroleum Geology*, **56,** 184-221.

EISMA, D. & VAN DER GAAST, S. (1971) Determination of Opal in Marine Sediments by X-Ray Diffraction. *Netherlands Journal of Sea Research*, **5,** 382-389.

ERNST, W. & CALVERT, S. (1969) An Experimental Study of the Recrystallization of Porcelanite and Its Bearing on the Origin of Some Bedded Cherts. *Am. J. Sci*, **267,** 114-133.

EVERITT, B.S. & SKRONDAL, A. (2002) The Cambridge Dictionary of Statistics. *Cambridge: Cambridge*.

FAERSETH, R.B., KNUDSEN, B.E., LILJEDAHL, T., MIDBOE, P.S. & SODERSTROM, B. (1997) Oblique Rifting and Sequential Faulting in the Jurassic Development of the Northern North Sea. *Journal of Structural Geology*, **19,** 1285-1302.

FALEIDE, J.I., KYRKJEBO, R., KJENNERUD, T., GABRIELSEN, R.H., JORDT, H., FANAVOLL, S. & BJERKE, M.D. (2002) Tectonic Impact on Sedimentary Processes During Cenozoic Evolution of the Northern North Sea and Surrounding Areas. *Geological Society, London, Special Publications*, **196,** 235-269.

FLÖRKE, O., JONES, J. & SEGNIT, E. (1975) Opal-Ct Crystals. *Neues Jahrbuch Mineralogie Monatsheft*, **8,** 69-377.

FLÖRKE, O., KÖHLER-HERBERTZ, B., LANGER, K. & TÖNGES, I. (1982) Water in Microcrystalline Quartz of Volcanic Origin: Agates. *Contributions to Mineralogy and Petrology*, **80,** 324-333.

FLÖRKE, O.W., HOLLMANN, R., RAD, U. & RÖSCH, H. (1976) Intergrowth and Twinning in Opal-Ct Lepispheres. *Contributions to Mineralogy and Petrology*, **58,** 235-242.

FLÖRKE, O.W., GRAETSCH, H., MARTIN, B., RÖLLER, K. & WIRTH, R. (1991) Nomenclature of Microcrystalline and Non-Crystalline Silica Minerals, Based on Structure and Microstructure. *Neues Jahrbuch Für Mineralogie-Abhandlungen*, **163,** 19-42.

FOSSEN, H. (2010) *Structural Geology*. Cambridge University Press.

GILES, M.R. (1997) Diagenesis: A Quantitative Perspective. *Implications for Basin Modelling and Rock Property Prediction*.

GOULTY, N. (2001) Mechanics of Layer-Bound Polygonal Faulting in Fine-Grained Sediments. *Journal of the Geological Society*, **159,** 239-246.

GRAETSCH, H., FLORKE, O.W. & MIEHE, G. (1985) The Nature of Water in Chalcedony and Opal-C from Brazilian Agate Geodes. *Physics and Chemistry of Minerals*, **12,** 300-306.

GRAETSCH, H., GIES, H. & TOPALOVIC, I. (1994) Nmr, Xrd and Ir Study on Microcrystalline Opals. *Physics and Chemistry of Minerals*, **21,** 166-175.

GRAETSCH, H. & IBEL, K. (1997) Small Angle Neutron Scattering by Opals. *Physics and Chemistry of Minerals*, **24,** 102-108.

GRAHAM, C., ARMOUR, A., BATHURST, P., EVANS, D. & PETROLEUMSFORENING, N. (2003). *The Millennium Atlas: Petroleum Geology of the Central and Northern North Sea*, Geological Society of London.

GUDMUNDSSON, A. (2011) *Rock Fractures in Geological Processes*. Cambridge University Press Cambridge.

GUERIN, G. & GOLDBERG, D. (1996) Acoustic and Elastic Properties of Calcareous Sediments across a Siliceous Diagenetic Front on the Eastern U.S. Continental Slope. *Geophysical Research Letters*, **23,** 2697-2700.

GUTHRIE, G.D., BISH, D.L. & REYNOLDS, R.C. (1995) Modeling the X-Ray Diffraction Pattern of Opal-Ct. *American Mineralogist*, **80,** 869.

HAIR, J.F., BLACK, W.C., BABIN, B.J., ANDERSON, R.E. & TATHAM, R.L. (2006) *Multivariate Data Analysis*. Pearson Prentice Hall Upper Saddle River, NJ.

HAMMOND, R.D. & GAITHER, J.R. (1983) Anomalous Seismic Character - Bering Sea Shelf. *Geophysics*, **48,** 590-605.

HANTSCHEL, T. & KAUERAUF, A.I. (2009) *Fundamentals of Basin and Petroleum Systems Modeling*. Springer.

HEANEY, P. (1994) Silica: Physical Behavior, Geochemistry & Materials Applications (Reviews in Mineralogy; Vol 29) Author: Pj Heaney.
HEIN, J.R., SCHOLL, D.W., BARRON, J.A., JONES, M.G. & MILLER, J. (1978) Diagenesis of Late Cenozoic Diatomaceous Deposits and Formation of the Bottom Simulating Reflector in the Southern Bering Sea*. *Sedimentology*, **25,** 155-181.
HEMPEL, P., MAYER, L., TAYLOR, E., BOHRMANN, G. & PITTENGER, A. (1989) 44. The Influence of Biogenic Silica on Seismic Lithostratigraphy at Odp Sites 642 and 643, Eastern Norwegian Sea1.
HERDIANITA, N.R., BROWNE, P.R.L., RODGERS, K.A. & CAMPBELL, K.A. (2000) Mineralogical and Textural Changes Accompanying Ageing of Silica Sinter. *Mineralium Deposita*, **35,** 48-62.
HESSE, R. (1988) *Diagenesis #13. Origin of Chert: Diagenesis of Biogenic Siliceous Sediments*.
HESSE, R. & SCHACHT, U. (2011) Chapter 9 - Early Diagenesis of Deep-Sea Sediments. In: *Developments in Sedimentology* (Ed. by H. Heiko & M. Thierry), **Volume 63**, 557-713. Elsevier.
HILLIER, S. (2002) Quantitative Analysis of Clay and Other Minerals in Sandstones by X-Ray Powder Diffraction (Xrpd). *Clay Mineral Cements in Sandstones: Special Publication*, **34,** 213-251.
HINMAN, N.W. (1990) Chemical Factors Influencing the Rates and Sequences of Silica Phase-Transitions - Effects of Organic-Constituents. *Geochimica Et Cosmochimica Acta*, **54,** 1563-1574.
HINMAN, N.W. (1998) Sequences of Silica Phase Transitions: Effects of Na, Mg, K, Al, and Fe Ions. *Marine Geology*, **147,** 13-24.
HOLGATE, N.E., JACKSON, C.A.-L., HAMPSON, G.J. & DREYER, T. (2013) Sedimentology and Sequence Stratigraphy of the Middle–Upper Jurassic Krossfjord and Fensfjord Formations, Troll Field, Northern North Sea. *Petroleum Geoscience*.
HUGGETT, J. (1992) Petrography, Mineralogy and Diagenesis of Overpressured Tertiary and Late Cretaceous Mudrocks from the East Shetland Basin. *Clay Minerals*, **27,** 487-487.
HURD, D.C. & THEYER, F. (1975) Changes in the Physical and Chemical Properties of Biogenic Silica from the Central Equatorial Pacific. *Adv. Chem. Ser*, **147,** 211-230.
ICENHOWER, J.P. & DOVE, P.M. (2000) The Dissolution Kinetics of Amorphous Silica into Sodium Chloride Solutions: Effects of Temperature and Ionic Strength. *Geochimica et Cosmochimica Acta*, **64,** 4193-4203.
ILER, R.K. (1979) The Chemistry of Silica, Wiley, New York.
IRELAND, M.T. (2011) 3-D Seismic Investigation of the Diagenesis and Deformation of Cenozoic Siliceous Sediments on the Eastern Atlantic Margin, Durham University.
IRELAND, M.T., DAVIES, R.J., GOULTY, N.R. & CARRUTHERS, D. (2011) Structure of a Silica Diagenetic Transformation Zone: The Gjallar Ridge, Offshore Norway. *Sedimentology*, **58,** 424-441.
ISAACS, C.M. (1981) Porosity Reduction During Diagenesis of the Monterey Formation, Santa Barbara Coastal Area, California.
ISAACSON, E. & NEFF, D. (1999). *A, B Avo Cross Plotting and Its Application in Greenland and the Barents Sea*. Geological Society, London, Petroleum Geology Conference series, Geological Society of London.
JAEGER, J.C., COOK, N.G. & ZIMMERMAN, R. (2009) *Fundamentals of Rock Mechanics*. John Wiley & Sons.
JAKY, J. (1948). *Pressure in Silos*. Proceedings of the 2nd international conference on soil mechanics and foundation engineering.
JENSEN, T.F. & BUCHARDT, B. (1987) *Sedimentology and Geochemistry of the Organic Carbon-Rich Lower Cretaceous Sola Formation (Barremian-Albian), Danish North Sea*. DGU.
JONES, J. & SEGNIT, E. (1972) Genesis of Cristobalite and Tridymite at Low Temperatures. *Journal of the Geological Society of Australia*, **18,** 419-422.
JONES, J.B. & SEGNIT, E.R. (1971) The Nature of Opal I. Nomenclature and Constituent Phases. *Journal of the Geological Society of Australia*, **18,** 57-68.
JORDT, H., FALEIDE, J.I., BJØRLYKKE, K. & IBRAHIM, M.T. (1995) Cenozoic Sequence Stratigraphy of the Central and Northern North Sea Basin: Tectonic Development, Sediment Distribution and Provenance Areas. *Marine and Petroleum Geology*, **12,** 845-879.

JORDT, H. (1996) The Cenozoic Geological Evolution of the Central and Northern North Sea Based on Seismic Sequence Stratigraphy. *PhD thesis, Institute of Geology, University of Oslo.*
JORDT, H., THYBERG, B.I. & NOTTVEDT, A. (2000) Cenozoic Evolution of the Central and Northern North Sea with Focus on Differential Vertical Movements of the Basin Floor and Surrounding Clastic Source Areas. *Geological Society, London, Special Publications*, **167,** 219-243.
JOY, A.M. (1993) Comments on the Pattern of Post-Rift Subsidence in the Central and Northern North Sea Basin. *Geological Society, London, Special Publications*, **71,** 123-140.
KALANI, M., JAHREN, J., MONDOL, N.H. & FALEIDE, J.I. (2014) Compaction Processes and Rock Properties in Uplifted Clay Dominated Units,-the Egersund Basin, Norwegian North Sea. *Marine and Petroleum Geology*.
KARLSSON, W., VOLLSET, J. & JØRGENSEN, P. (1979) Changes in Mineralogical Composition of Tertiary Sediments from North Sea Wells. *Developments in Sedimentology*, **27,** 281-289.
KASTNER, M., KEENE, J.B. & GIESKES, J.M. (1977) Diagenesis of Siliceous Oozes—I. Chemical Controls on the Rate of Opal-a to Opal-Ct Transformation—an Experimental Study. *Geochimica et Cosmochimica Acta*, **41,** 1041-1059.
KASTNER, M. & GIESKES, J. (1983) Opal-a to Opal-Ct Transformation: A Kinetic Study. *Developments in Sedimentology*, **36,** 211-227.
KELLER, M.A. & ISAACS, C.M. (1985) An Evaluation of Temperature Scales for Silica Diagenesis in Diatomaceous Sequences Including a New Approach Based on the Miocene Monterey Formation, California. *Geo-Marine Letters*, **5,** 31-35.
KIM, G.Y., YOO, D.G., LEE, H.Y., LEE, Y.J. & KIM, D.C. (2007) The Relationship between Silica Diagenesis and Physical Properties in the East/Japan Sea: Odp Legs 127/128. *Journal of Asian Earth Sciences*, **30,** 448-456.
KRÖGER, N., LORENZ, S., BRUNNER, E. & SUMPER, M. (2002) Self-Assembly of Highly Phosphorylated Silaffins and Their Function in Biosilica Morphogenesis. *Science*, **298,** 584-586.
KRÖGER, N. & POULSEN, N. (2008) Diatoms-from Cell Wall Biogenesis to Nanotechnology. *Annual review of genetics*, **42,** 83-107.
KURAMOTO, S., TAMAKI, K., LANGSETH, M., NOBES, D., TOKUYAMA, H., PISCIOTTO, K. & TAIRA, A. (1992) 73. Can Opal-a/Opal-Ct Bsr Be an Indicator of the Thermal Structure of the Yamato Basin, Japan Sea? *Age*, **794,** 36.35.
KYRKJEBØ, R., KJENNERUD, T., GILLMORE, G., FALEIDE, J. & GABRIELSEN, R. (2001) Cretaceous-Tertiary Palaeo-Bathymetry in the Northern North Sea; Integration of Palaeo-Water Depth Estimates Obtained by Structural Restoration and Micropalaeontological Analysis. *Norwegian Petroleum Society Special Publications*, **10,** 321-345.
LANGER, K. & FLÖRKE, O. (1974) Near Infrared Absorption Spectra (4000–9000 Cm–1) of Opals and the Role of "Water" in These Sio2–Nh2o Minerals. *Fortschritte der Mineralogie*, **52,** 17-51.
LASDON, L.S., WAREN, A.D., JAIN, A. & RATNER, M. (1978) Design and Testing of a Generalized Reduced Gradient Code for Nonlinear Programming. *ACM Transactions on Mathematical Software (TOMS)*, **4,** 34-50.
LØSETH, H., RAULLINE, B. & NYGÅRD, A. (2013) Late Cenozoic Geological Evolution of the Northern North Sea: Development of a Miocene Unconformity Reshaped by Large-Scale Pleistocene Sand Intrusion. *Journal of the Geological Society*, **170,** 133-145.
LUCAZEAU, F. & LE DOUARAN, S. (1984) Numerical Model of Sediment Thermal History Comparison between the Gulf of Lion and the Viking Graben. *Thermal Phenomena in Sedimentary Basins: Editions Technip, Paris***,** 211-218.
MARCUSSEN, O., THYBERG, B.I., PELTONEN, C., JAHREN, J., BJORLYKKE, K. & FALEIDE, J.I. (2009) Physical Properties of Cenozoic Mudstones from the Northern North Sea: Impact of Clay Mineralogy on Compaction Trends. *AAPG Bulletin*, **93,** 127-150.
MAYERSON, D. & CROUCH, J. (1994) The Opal-Ct/Quartz Diagenetic Boundary within the Monterey Formation of the California Offshore Santa Maria Basin; an Untapped Exploration Target (Abs.). *AAPG Bulletin*, **78,** 669-670.
MEADOWS, D. & DAVIES, R.J. (2007) Morphological Development of Basin-Scale Silica Diagenetic Fronts Revealed with 2d Seismic Reflection Data: Offshore Sakhalin, Russian Far East. *Journal of the Geological Society*, **164,** 1193-1206.

MEADOWS, D. & DAVIES, R.J. (2009) Predicting Porosity Reduction Due to Silica Diagenesis Using Seismic Reflection Data. *Marine and Petroleum Geology*, **26,** 1543-1553.
MICHALOPOULOS, P. & ALLER, R.C. (2004) Early Diagenesis of Biogenic Silica in the Amazon Delta: Alteration, Authigenic Clay Formation, and Storage. *Geochimica et Cosmochimica Acta*, **68,** 1061-1085.
MIZUTANI, S. (1966) Transformation of Silica under Hydrothermal Conditions. *The Journal of earth sciences, Nagoya University*, **14,** 56-88, Pl. I-IV.
MIZUTANI, S. (1967) Kinetic Aspects of Diagenesis of Silica. *The Journal of earth sciences, Nagoya University*, **15,** 99-111.
MIZUTANI, S. (1970) Silica Minerals in Early Stage of Diagenesis. *Sedimentology*, **15,** 419-&.
MONDOL, N.H., BJØRLYKKE, K., JAHREN, J. & HØEG, K. (2007) Experimental Mechanical Compaction of Clay Mineral Aggregates—Changes in Physical Properties of Mudstones During Burial. *Marine and Petroleum Geology*, **24,** 289-311.
MOORE, D.M. & REYNOLDS, R.C. (1997) *X-Ray Diffraction and the Identification and Analysis of Clay Minerals*, 2nd edn. Oxford university press Oxford.
MURAOKA, H. & KAMATA, H. (1983) Displacement Distribution Along Minor Fault Traces. *Journal of Structural Geology*, **5,** 483-495.
NADIN, P. & KUSZNIR, N. (1995) Palaeocene Uplift and Eocene Subsidence in the Northern North Sea Basin from 2d Forward and Reverse Stratigraphic Modelling. *Journal of the Geological Society*, **152,** 833-848.
NEAGU, R.C., CARTWRIGHT, J., DAVIES, R. & JENSEN, L. (2010) Fossilisation of a Silica Diagenesis Reaction Front on the Mid-Norwegian Margin. *Marine and Petroleum Geology*, **27,** 2141-2155.
NPD (2014) Norwegian Petroleum Directorate: Http://Factpages.Npd.No/Factpages/.
OTTESEN, D., DOWDESWELL, J.A., RISE, L. & BUGGE, T. (2012) Large-Scale Development of the Mid-Norwegian Shelf over the Last Three Million Years and Potential for Hydrocarbon Reservoirs in Glacial Sediments. *Geological Society, London, Special Publications*, **368,** 53-73.
PEARSON, K. (1895) Note on Regression and Inheritance in the Case of Two Parents. *Proceedings of the Royal Society of London*, **58,** 240-242.
PEARSON, M. & SMALL, J. (1988) Illite-Smectite Diagenesis and Palaeotemperatures in Northern North Sea Quaternary to Mesozoic Shale Sequences. *Clay Minerals*, **23,** 109-132.
PEARSON, M. (1990) Clay Mineral Distribution and Provenance in Mesozoic and Tertiary Mudrocks of the Moray Firth and Northern North Sea. *Clay Minerals*, **25,** 519-541.
PEDERSEN, P., THRONDSEN, T., LYSELL, F., DROTTING, Å. & RAUTAKORPI, T. (2005). *Characterization and Occurrence of Opal-Reflectors*. 67th EAGE Conference & Exhibition.
PEGRUM, R.M., ØDEGÅRD, T., BONDE, K. & HAMANN, N.E. (2001). *Exploration in the Fylla Area, Sw Greenland*. Proceedings of AAPG Regional Conference.
PELTONEN, C., MARCUSSEN, Ø., BJØRLYKKE, K. & JAHREN, J. (2009) Clay Mineral Diagenesis and Quartz Cementation in Mudstones: The Effects of Smectite to Illite Reaction on Rock Properties. *Marine and Petroleum Geology*, **26,** 887-898.
PERRY, C.C. (2003) Silicification: The Processes by Which Organisms Capture and Mineralize Silica. *Reviews in mineralogy and geochemistry*, **54,** 291-327.
PISCIOTTO, K.A. (1981) Distribution, Thermal Histories, Isotopic Compositions, and Reflection Characteristics of Siliceous Rocks Recovered by the Deep Sea Drilling Project.
PRICE, N.J. & COSGROVE, J.W. (1990) *Analysis of Geological Structures*. Cambridge University Press.
RICKERT, D., SCHLÜTER, M. & WALLMANN, K. (2002) Dissolution Kinetics of Biogenic Silica from the Water Column to the Sediments. *Geochimica et Cosmochimica Acta*, **66,** 439-455.
RIDER, M.H. & KENNEDY, M. (2011) The Geological Interpretation of Well Logs.
RIIS, F. & FJELDSKAAR, W. (1992) On the Magnitude of the Late Tertiary and Quaternary Erosion and Its Significance for the Uplift of Scandinavia and the Barents Sea. *Structural and tectonic modelling and its application to petroleum geology*, **1,** 163-185.
RIMSTIDT, J.D. & BARNES, H.L. (1980) The Kinetics of Silica-Water Reactions. *Geochimica Et Cosmochimica Acta*, **44,** 1683-1699.

RUNDBERG, Y. (1989) *Tertiary Sedimentary History and Basin Evolution of the Norwegian North Sea between 60°-62°N: An Integrated Approach*. Universititet i Trondheim, Norges tekniske høgskole.
RUNDBERG, Y. & EIDVIN, T. (2005) Controls on Depositional History and Architecture of the Oligocene-Miocene Succession, Northern North Sea Basin. In: *Norwegian Petroleum Society Special Publications* (Ed. by J. P. N. E. E. Bjørn T.G Wandås & G. Felix), **Volume 12**, 207-239. Elsevier.
SCHWARZ, G. (1978) Estimating the Dimension of a Model. *The annals of statistics*, **6,** 461-464.
SELNES, A., STROMMEN, J., LUBBE, R., WATERS, K. & DVORKIN, J. (2013). *Flat Spots-True Dhis or False Positives?* 75th EAGE Conference & Exhibition incorporating SPE EUROPEC 2013.
SHIN, H., SANTARNARINA, J.C. & CARTWRIGHT, J.A. (2008) Contraction-Driven Shear Failure in Compacting Uncemented Sediments. *Geology*, **36,** 931-934.
SPINELLI, G.A., MOZLEY, P.S., TOBIN, H.J., UNDERWOOD, M.B., HOFFMAN, N.W. & BELLEW, G.M. (2007) Diagenesis, Sediment Strength, and Pore Collapse in Sediment Approaching the Nankai Trough Subduction Zone. *Geological Society of America Bulletin*, **119,** 377-390.
SWANSON, H.E., TATGE, E. & FUYAT, R.K. (1953) Standard X-Ray Diffraction Powder Patterns.
TADA, R. & IIJIMA, A. (1983) Petrology and Diagenetic Changes of Neogene Siliceous Rocks in Northern Japan. *Journal of Sedimentary Petrology*, **53,** 911-930.
TEAM, R.C. (2014) R: A Language and Environment for Statistical Computing. R Foundation for Statistical Computing, Vienna, Austria, 2012, ISBN 3-900051-07-0.
TERZAGHI, K. (1996) *Soil Mechanics in Engineering Practice*. John Wiley & Sons.
THYBERG, B., JORDT, H., BJORLYKKE, K. & FALEIDE, J. (2000) Relationships between Sequence Stratigraphy, Mineralogy and Geochemistry in Cenozoic Sediments of the Northern North Sea. *SPECIAL PUBLICATION-GEOLOGICAL SOCIETY OF LONDON*, **167,** 245-272.
THYBERG, B., JAHREN, J., WINJE, T., BJORLYKKE, K., FALEIDE, J.I. & MARCUSSEN, O. (2010) Quartz Cementation in Late Cretaceous Mudstones, Northern North Sea: Changes in Rock Properties Due to Dissolution of Smectite and Precipitation of Micro-Quartz Crystals. *Marine and Petroleum Geology*, **27,** 1752-1764.
THYBERG, B. & JAHREN, J. (2011) Quartz Cementation in Mudstones: Sheet-Like Quartz Cement from Clay Mineral Reactions During Burial. *Petroleum Geoscience*, **17,** 53-63.
THYBERG, B.I., STABELL, B., FALEIDE, J.I. & BJORLYKKE, K. (1999) Upper Oligocene Diatomaceous Deposits in the Northern North Sea - Silica Diagenesis and Paleogeographic Implications. *Norsk Geologisk Tidsskrift*, **79,** 3-18.
TREGUER, P., NELSON, D.M., VAN BENNEKOM, A.J., DEMASTER, D.J., LEYNAERT, A. & QUEGUINER, B. (1995) The Silica Balance in the World Ocean: A Reestimate. *Science*, **268,** 375-379.
TREGUER, P.J. & DE LA ROCHA, C.L. (2013) The World Ocean Silica Cycle. *Ann Rev Mar Sci*, **5,** 477-501.
VOLPI, V., CAMERLENGHI, A., HILLENBRAND, C.D., REBESCO, M. & IVALDI, R. (2003) Effects of Biogenic Silica on Sediment Compaction and Slope Stability on the Pacific Margin of the Antarctic Peninsula. *Basin Research*, **15,** 339-363.
VON RAD, U., RIECH, V. & ROESCH, H. (1978) 31. Silica Diagenesis in Continental Margin Sediments Off Northwest Africa. *Deep Sea Drilling*.
WALDEN, A.T. & WHITE, R.E. (1998) Seismic Wavelet Estimation: A Frequency Domain Solution to a Geophysical Noisy Input-Output Problem. *Ieee Transactions on Geoscience and Remote Sensing*, **36,** 287-297.
WATTERSON, J. (1986) Fault Dimensions, Displacements and Growth. *Pure and Applied Geophysics*, **124,** 365-373.
WEIBEL, R., FRIIS, H., KAZEROUNI, A.M., SVENDSEN, J.B., STOKKENDAL, J. & POULSEN, M.L.K. (2010) Development of Early Diagenetic Silica and Quartz Morphologies—Examples from the Siri Canyon, Danish North Sea. *Sedimentary Geology*, **228,** 151-170.
WELTON, J.E. (1984) *Sem Petrology Atlas*. American Association of Petroleum Geologists Tulsa^ eOklahoma Oklahoma.
WENSAAS, L., AAGAARD, P., BERRE, T. & ROALDSET, E. (1998) Mechanical Properties of North Sea Tertiary Mudrocks: Investigations by Triaxial Testing of Side-Wall Cores. *Clay Minerals*, **33,** 171-183.

WIEN, S.T. & KJENNERUD, T. (2005) 3d Cretaceous to Cenozoic Palaeobathymetry of the Northern North Sea. *Norwegian Petroleum Society Special Publications*, **12,** 241-253.
WILLIAMS, L.A. & CRERAR, D.A. (1985) Silica Diagenesis, Ii. General Mechanisms. *SEPM Journal of Sedimentary Research*, **Vol. 55,** 312-321.
WILLIAMS, L.A., PARKS, G.A. & CRERAR, D.A. (1985) Silica Diagenesis; I, Solubility Controls. *Journal of Sedimentary Research*, **55,** 301-311.
WORDEN, R. & MORAD, S. (2000) Quartz Cementation in Oil Field Sandstones: A Review of the Key Controversies. *Quartz cementation in sandstones*, **29,** 1-20.
YIELDING, G. (1990) Footwall Uplift Associated with Late Jurassic Normal Faulting in the Northern North-Sea. *Journal of the Geological Society*, **147,** 219-222.